VYSOKÉ UČENÍ TECHNICKÉ V BRNĚ

BRNO UNIVERSITY OF TECHNOLOGY

FAKULTA STROJNÍHO INŽENÝRSTVÍ

FACULTY OF MECHANICAL ENGINEERING

ÚSTAV MECHANIKY TĚLES, MECHATRONIKY A BIOMECHANIKY

INSTITUTE OF SOLID MECHANICS, MECHATRONICS AND BIOMECHANICS

VÝPOČTOVÉ MODELOVÁNÍ VLIVU PORUCH ŠÍŘENÍ VZRUCHU NA KONTRAKCI LEVÉ SRDEČNÍ KOMORY

COMPUTATIONAL STUDY OF THE IMPACT OF DISORDERS IN EXCITATION PROPAGATION ON LEFT VENTRICULAR CONTRACTION

DIZERTAČNÍ PRÁCE

DOCTORAL THESIS

AUTOR PRÁCE — Ing. Jiří Vaverka

AUTHOR

ŠKOLITEL — prof. Ing. Jiří Burša, Ph.D.

SUPERVISOR

BRNO 2022

Abstract

This doctoral thesis deals with computational modeling of contraction of human left ventricle using finite element method. The primary goal is to determine the impact of the left bundle branch block on ventricular ejection fraction. Additionally, changes in ventricular motions, strains and stress distribution, resulting from the block, are also investigated. Electrical activation of left ventricle under healthy conditions and during the branch block is modeled by the monodomain equation coupled with an artificial ionic model designed to reduce the computational demands of the monodomain equation. Conduction velocity in myocardium is considered orthotropic. Calculated activation maps show that the left bundle branch block prolongs electrical activation by 50 % which agrees with clinically observed prolongation of the QRS complex on ECG. The activation maps are subsequently used in the simulations of ventricular mechanics to distribute the beginning of contraction throughout the finite-element mesh. Passive mechanical behavior of myocardium is described by an orthotropic hyperelastic model. Active stresses, induced by muscle contraction, are incorporated by means of the time-dependent active strain tensor. Contraction starts from a prestressed reference configuration representing the end-diastolic state of the ventricle. Pressure development during ejection phase is controlled by two-parametric Windkessel model. Results indicate that the left bundle branch block does not substantially reduce the pumping efficiency of the ventricle; ejection fraction in the diseased state decreased by only 2.3 % relative to the healthy conditions which agrees with some of the previously published clinical studies. Changes in displacements and strains, predicted by the model, correspond with clinical and experimental observations. Stress analyses revealed unexpectedly high stresses in the interventricular septum; further analyses with modified boundary conditions have been suggested in order to better assess these result.

Keywords

heart, left ventricle, finite element method, conduction system, left bundle branch, monodomain equation, hyperelasticity

Abstrakt

Tato disertační práce se zabývá výpočtovým modelováním kontrakce levé srdeční komory pomocí metody konečných prvků. Primárním cílem práce je vyhodnotit vliv blokády levého Tawarova raménka na ejekční frakci komory. Dále je vyšetřován dopad blokády na pohyby komory během srdečního cyklu, na lokální hodnoty přetvoření a na rozložení napětí ve stěně. Průběh elektrické aktivace jak zdravé komory, tak i komory s blokádou je modelován pomocí monodoménové rovnice svázané s pseudo-modelem buněčné membrány, který byl navržen za účelem snížení výpočetní náročnosti monodoménové rovnice. Rychlost šíření vzruchu v myokardu je uvažována ortotropní. Vypočítané časové průběhy elektrické aktivace ukazují, že blokáda levého Tawarova raménka prodlužuje dobu depolarizace komory o 50 %, což je v souladu s udávanými délkami trvání QRS komplexu na EKG u zdravých jedinců a u pacientů s blokádou. Průběhy elektrické aktivace jsou následně využity v simulacích kontrakce komory pro předepsání počátku kontrakce jednotlivých prvků sítě. Pasivní mechanická odezva myokardu je v těchto simulacích popsána pomocí ortotropního hyperelastického modelu. Aktivní napětí vyvolané svalovou kontrakcí je do modelu zahrnuto prostřednictvím časově závislého tenzoru aktivního přetvoření. Do počáteční konfigurace modelu, reprezentující stav komory na konci diastoly, je před zahájením kontrakce zahrnuto předpětí odpovídající end-diastolickému tlaku v komoře. Časový průběh komorového tlaku během ejekční fáze je modelován pomocí dvouparametrického modelu Windkessel. Výsledky simulací ukazují, že blokáda levého Tawarova raménka nesnižuje významně čerpací schopnost komory. Predikovaný pokles ejekční frakce v důsledku blokády činí pouze 2.3 %, což je v souladu s některými publikovanými klinickými výsledky. Vypočítané časové průběhy posuvů a přetvoření ve vybraných místech modelu taktéž vykazují některé charakteristiky popisované klinickými nebo experimentálními studiemi. V oblasti mezikomorového septa byly pozorovány výrazně vyšší hodnoty napětí než v ostatních částech komory; tyto výsledky však bude nutné ověřit dalšími výpočty, neboť v současném modelu není septum zatíženo silovými účinky vyvolanými kontrakcí pravé komory.

Klíčová slova

srdce, levá komora, metoda konečných prvků, převodní systém, levé Tawarovo raménko, monodoménová rovnice, hyperelasticita

Statement of originality

I declare that the material contained in this thesis is an original work composed by myself under the guidance and advice of my supervisor prof. Ing. Jiří Burša, Ph.D.

Brno 27th September 2022

Jiří Vaverka

Acknowledgments

I would like to thank my supervisor prof. Jiří Burša for all his help, continuous support, and patience during my doctoral studies. I have been very lucky to have the opportunity to study under his friendly and inspiring guidance.

Contents

1 Scope and plan of thesis

Computational modeling is nowadays a powerful tool complementing traditional clinical observations and experimental studies in our effort to better understand physiological processes in human body. It enables to evaluate the severity of functional disorders as well as predict the outcomes of medical treatments. This thesis deals with computational modeling of electrophysiology and mechanics of the left ventricle (LV) of the heart. These two fields of study are closely related in the context of cardiac physiology because contraction is induced by electrical activation. It follows that electrical disturbances in LV affect also its mechanical function, more precisely its ability to generate blood pressure inside the ventricle and, consequently, to eject sufficient amount of blood into aorta. This work will be focused on one of the most common pathological conditions affecting the electrical activation of LV – the left bundle branch block (LBBB). Modern computational methods and various mathematical models, describing different aspects of LV function, will be integrated together in order to investigate the overall impact of isolated LBBB on LV function.

The thesis is divided into six chapters. Chapter 2 starts with a basic description of the structure and function of the heart. Afterwards, more in-depth information is provided about the structure of ventricular wall and arrangement of muscle fibres in myocardium. At the end of the chapter, a fairly detailed description of the time course of electrical activation of ventricular myocardium is given. In Chapter 3, the problem addressed by the thesis is discussed and individual goals are specified. The chapter also gives references to the author's previous work on related topics. The most important part of thesis is represented by Chapters 4 and 5 which contain complete step-by-step description of the process of creation of computational models of LV electrophysiology (Chapter 4) and mechanics (Chapter 5). At the end of both chapters, the results are presented and discussed. The last chapter summarizes the results as well as limitations of this work and suggests some potential directions for future work.

2 Selected parts from anatomy and physiology of heart

This chapter presents selected information regarding the structure and function of the heart. Its content was selected with respect to the subject of this thesis and the amount of information included should scarcely exceed the level necessary for understanding of the problem addressed by the thesis.

2.1 Basic cardiac anatomy and function, blood circulation

The heart consists of four chambers (Fig. 1): the *left* and the *right atrium*, and the *left* and the *right ventricle*. The ventricles are separated from each other by the *interventricular septum* and the atria are separated by the *interatrial septum*. The left and the right side of the heart form two separate pumps that work in series. The flow of blood is maintained by coordinated contractions of chambers. Both atria contract approximately simultaneously and the same applies to the ventricles. Contraction of atria precedes contraction of ventricles. The right ventricle pumps deoxygenated blood through the *pulmonary valve* into the *pulmonary trunk*, which is the first part of the *pulmonary circuit* leading to the lungs. Oxygenated blood returning from the lungs passes through the *pulmonary veins* into the left atrium. Contraction of the left atrium pushes blood through the *mitral valve* into the left ventricle, which in turn propels blood through the *aortic valve* into the aorta. Here the blood starts its route through the *systemic circuit*, which delivers oxygen and nutrients to all parts of the body (except to the parts of the lungs supplied by the pulmonary arteries). Deoxygenated blood returning from the systemic circuit enters the right atrium through the *superior vena cava* and the *inferior vena cava*. Pressure gradient and the contraction of the right atrium propel blood through the *tricuspid valve* into the right ventricle which completes one circuit of blood throughout the body (during which blood passes through the heart twice).

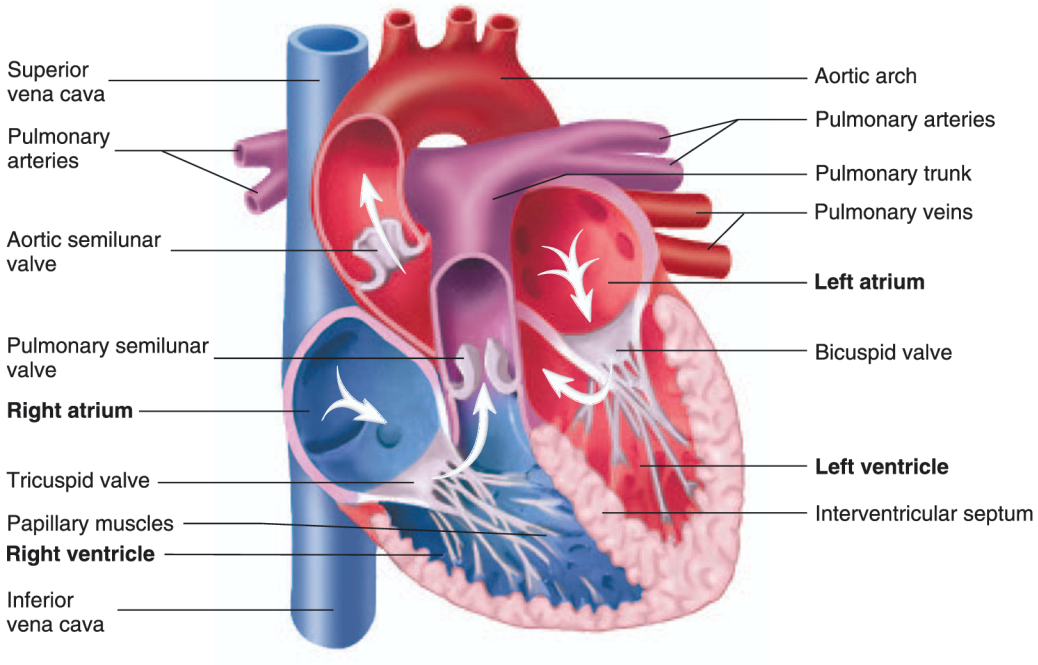

Fig. 1: Internal anatomy of the heart with arrows indicating the flow of blood through the heart. (Adopted from [1].)

2.2 Cardiac cycle

The totality of actions and events in heart that occur during one contraction and one relaxation of ventricles is called a *cardiac cycle*. Sometimes the term is also used to refer to the corresponding period of time [1]. Each cardiac cycle begins with the onset of ventricular contraction and consists of *systole*, during which the ventricles contract, and *diastole*, during which they relax.[1] Systole is further divided into the period of isovolumic contraction and the period of ejection, while diastole consists of the period of isovolumic relaxation, passive ventricular filling and active ventricular filling [1]. With regard to the topic of this thesis, description of these phases will be provided here in terms of the events occurring in the left side of the heart. The corresponding pressure and volume changes are displayed in Fig. 2.

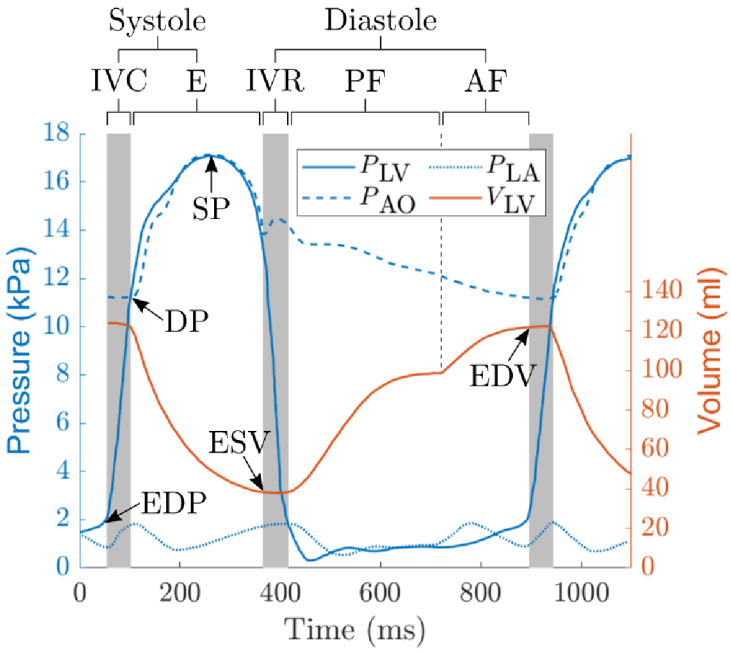

Fig. 2: Temporal evolution of left ventricular pressure (P_{LV}), aortic pressure (P_{AO}), left atrial pressure (P_{LA}) and left ventricular volume (V_{LV}) in normal healthy human heart (based on Fig. 1 from [2]). IVC: isovolumic contraction, E: ejection, IVR: isovolumic relaxation, PF: passive filling, AF: active filling, SP: systolic pressure, DP: diastolic pressure, EDP: end-diastolic pressure, EDV: end-diastolic volume, ESV: end-systolic volume.

Before systole begins, the LV is filled with blood, the aortic valve is closed and the mitral valve is open. As the ventricle begins to contract, the ventricular pressure increases, causing immediately the mitral valve to close. This initiates the short phase of *isovolumic contraction* (IVC) during which both valves are closed and so the volume of blood in the ventricle is kept constant. The ongoing contraction rapidly increases the ventricular pressure, which at some point becomes higher than the current pressure in aorta (the *diastolic pressure* – the lowest value of the aortic pressure). As a result, the aortic valve is pushed open, which starts the *ejection phase* during which blood flows from the ventricle into the aorta. During this phase the aortic pressure reaches its maximum value, called the *systolic pressure*. The flow of blood out of the ventricle finally ceases and the ventricular

[1]The terms "systole" and "diastole" are also used more generally to denote contraction and relaxation of *any* chamber, including atria.

pressure falls below that in aorta. As a result, blood will tend to flow back toward the ventricle, which causes the aortic valve to close. The closure is followed by a slight increase in aortic pressure producing the *dicrotic notch*, or *incisura*, on the pressure curve (see Fig. 2); this is a consequence of an elastic recoil of the stretched aorta [1]. The volume of blood left in the ventricle after the closure of the aortic valve is called the LV *end-systolic volume*. Since the mitral valve remains closed as well, the ventricular volume does not change during the subsequent *isovolumic relaxation* phase, only the pressure decreases rapidly. Meanwhile, the left atrium has been filled by the inflow of blood from the pulmonary veins. As the ventricle continues to relax, its pressure becomes lower than that in the atrium, which leads to the opening of the mitral valve and *passive filling* of LV. The adjective "passive" means that the inflow is only a result of the pressure gradient between the ventricle and veins, which propels blood into the ventricle. This passive inflow accounts for ∼80 % of the total diastolic filling (under resting conditions) [2]. The remaining 20 % is a result of the subsequent contraction of the atrium (the *active filling*). The amount of blood in the ventricle at the end of diastole (beginning of systole) is called the *end-diastolic volume* and the corresponding ventricular pressure is the *end-diastolic pressure*.

Normal values of systolic pressure and diastolic pressure are approximately 16 kPa and 10.7 kPa, respectively [1].[1] Some other important pressures and volumes can be read from Fig. 2 which is exemplary (although interindividual variations in volumes can be significant, especially between men and women [3]). If we consider a normal resting heart rate of about 70 beats per minute, the corresponding duration of one cardiac cycle is approximately 850 ms. Normal resting values of isovolumic contraction time, ejection time and isovolumic relaxation time are approximately 40–70 ms, 280 ms and 80–90 ms, respectively [4, 5].

2.3 Structure of heart wall, fibre arrangement

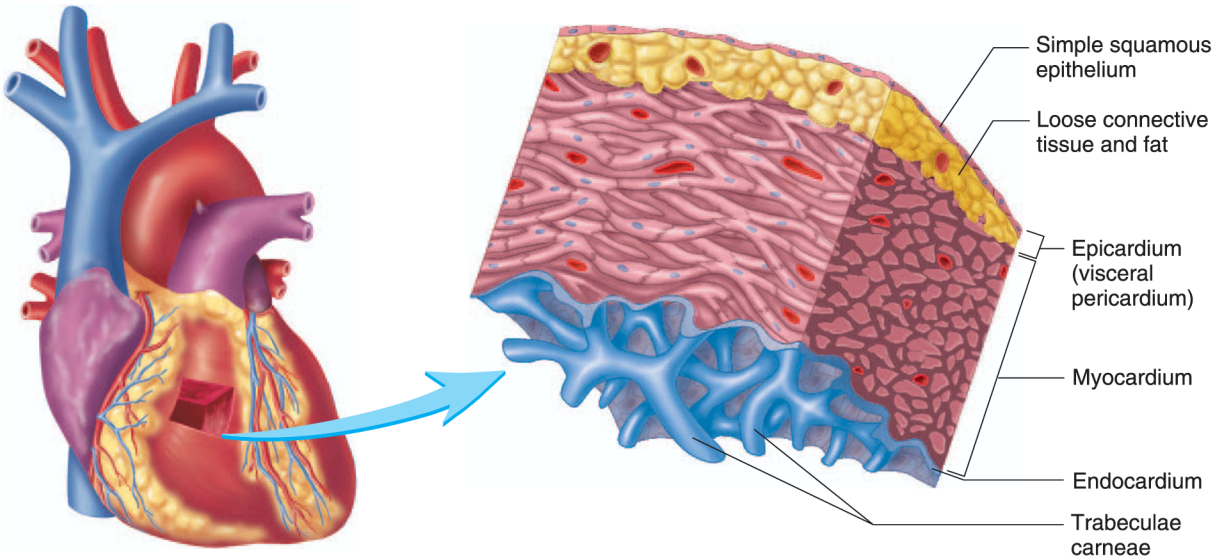

Fig. 3: Structure of the heart wall [1].

[1]In medicine, it is more common to express pressures is millimetres of mercury (mmHg). An approximate conversion relation is 1 mmHg ≈ 133.322 Pa. In this work, all pressures will be expressed in pascals (Pa) or decimal multiples of pascal (kPa, MPa, etc.) because these units are more common in physics.

The wall of the heart consists of three layers of tissue (Fig. 3): the *epicardium*, the *myocardium* and the *endocardium*. Epicardium is a smooth thin membrane that covers the outer surface of the heart. It is in contact with pericardial fluid, which reduces friction between moving heart and the pericardial sac that surrounds it [1]. Myocardium is the thickest part of the wall which consists mainly of cardiac muscle cells (*cardiomyocytes*) and, accordingly, is responsible for contraction. Endocardium is a thin layer that covers the inner surfaces of the heart and facilitates movement of blood on its interface with the walls [1]. In ventricles the endocardium is laid over irregular muscle bundles called *trabeculae carneae*, while in atria the interior surfaces are mainly flat [1].

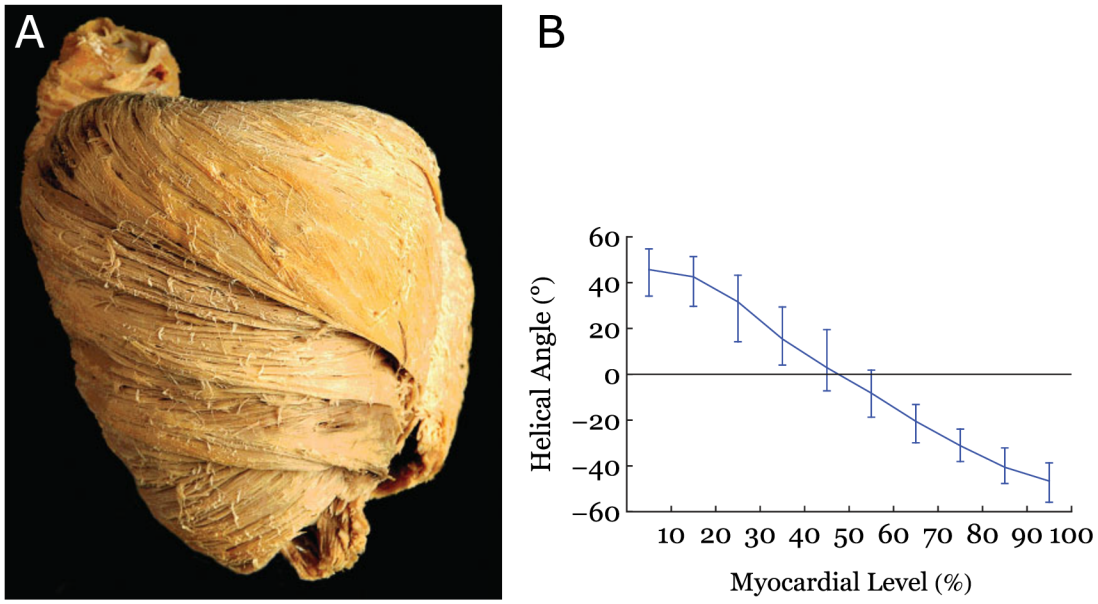

Fig. 4: (A) Porcine heart with successively removed layers of the left ventricular myocardium. The depth of dissection increases from the base (the top part of the heart) to the apex (the lower tip of the heart) and reveals the left-hand helix orientation of the subepicardial fibres, the right-hand helix orientation of the subendocardial fibres, and the circumferential alignment in the central part of the wall [6]. (B) Helical angle as a function of myocardial depth in percent (0 %: subendocardium, 100 %: subepicardium). Results are shown as medians with interquartile range. Data were obtained from porcine hearts using diffusion tensor magnetic resonance imaging [7]. Twelve different zones of left ventricle were scanned (including the septum where 100 % is the right ventricular subendocardium). Separate data for the individual zones can be found in the original paper [7].

The working units of myocardium are cardiomyocytes, which provide force for the ejection of blood. They are elongated cells connected mostly end-to-end but also by side branches into a complex three-dimensional mesh with locally distinguishable preferred direction [8]. The longitudinal chains of myocytes in this mesh are generally called "fibres" even though they are continuous and interconnected with no distinct origin nor insertion (unlike skeletal muscles) [8]. Fibres are predominantly tangent to the walls, although there are also populations of myocytes that are inclined more radially [6]. The orientation of fibres with respect to the circumferential direction is markedly changing across the wall, as clearly shown in Fig. 4A. The sharp angle between the longitudinal axis of a fibre and the local circumferential direction is called the *helical angle*; it is positive when fibres form the right-hand helix and negative when they form the left-hand helix [7]. In the

end-diastolic state the values of the helical angle in LV vary approximately from $+60°$ in the subendocardial layer to $-60°$ in the subepicardial layer [7]. Moreover, this variation is almost linear across the wall (Fig. 4B) and fairly uniform throughout the LV myocardium [7].

Fibres in ventricular myocardium are further aggregated (by means of connective tissue) into larger structures with layered appearance (Fig. 5A) [9]. It is however important to note that these layers (which are usually called "sheets" or "sheetlets" [9, 10]) are not separated from each other; as Fig. 5A clearly shows, they are interconnected by branches running through the interstitial spaces. Thus there are no discrete bundles of myocytes in ventricular myocardium and its structure can perhaps best be characterized as a continuous three-dimensional myocardial mesh in which we can locally determine the predominant fibre direction and the sheet orientation [10, 6]. This specific microstructure determines the electrical and mechanical properties of myocardium, which are naturally orthotropic [11, 12] (as will be discussed later). In order to mathematically describe these properties, it is common to introduce a local orthonormal basis defined by the *fibre vector* $\mathbf{f}$ (aligned with the predominant fibre direction), the *sheet vector* $\mathbf{s}$ (in the plane of the sheet, perpendicular to $\mathbf{f}$) and the *sheet-normal vector* $\mathbf{n}$ (perpendicular to the sheet); see Fig. 5B. The distribution of these vectors in some region within the wall can be determined by a non-invasive technique known as the *diffusion tensor magnetic resonance imaging* (e.g. [7, 13]). In vivo measurements using this technique [13] revealed that the sheet orientation (represented either by $\mathbf{s}$ or $\mathbf{n}$) in LV considerably changes during systole (much more than the helical angle calculated from $\mathbf{f}$ does). At the beginning of systole the sheets are almost tangent to the wall [7, 13], while at its end they are oriented much more radially [13]. This reorientation represents a predominant mechanism of the thickening of LV wall during systole (>35 %) [13].

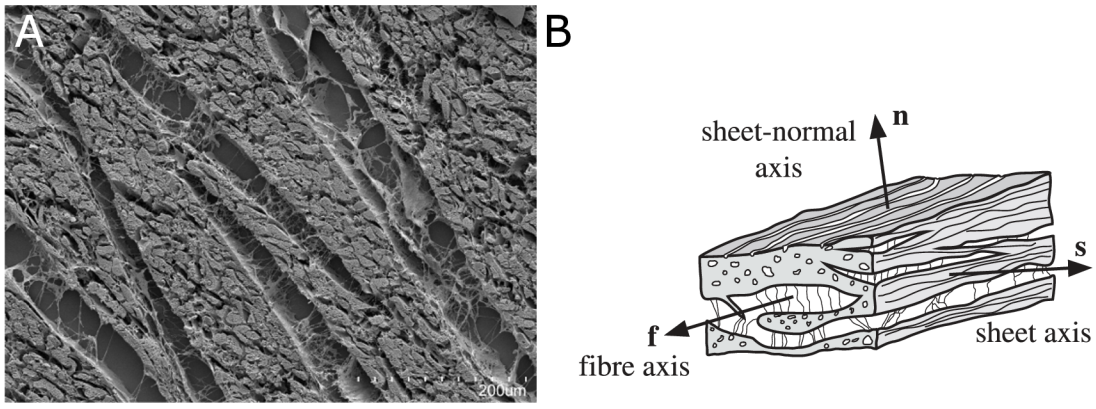

Fig. 5: (A) An electron microscopic image of a section through the left ventricular wall (perpendicular to the fibres) showing how individual fibres are aggregated together in a layered fashion [9]. (B) A scheme of the 3-dimensional layered structure of ventricular myocardium with the corresponding structural vectors (modified from [14]).

2.4 Electrical activation of heart

Contraction of cardiomyocytes is initiated by their electrical activation. A myocyte is activated when its membrane potential[1] increases from its resting value (approximately -83 mV [16]) to the threshold potential (approximately -60 mV [16]). In tissue, this occurs as a result of a flow of ions between adjacent interconnected cells [1]. Activation of a cell then gives rise to a sequence of changes in the permeability of ionic channels in cell membrane. The resulting exchange of ions between intra- and extracellular spaces is reflected by a specific time course of membrane potential, which is called the *action potential*. As can be seen from Fig. 6, the shapes of the action potentials in LV vary across the thickness of the wall. The initial rapid increase of potential is called a *depolarization* of the membrane; it lasts only about 1 ms [17] and, as will be discussed later, critically increases computational demands of computer simulations of action potential propagation [17, 18]. Once a cell is depolarized, it becomes a source of activation for its neighboring cells because the depolarization initiates exchange of ions leading to the increase of the neighboring cells' membrane potential [1].

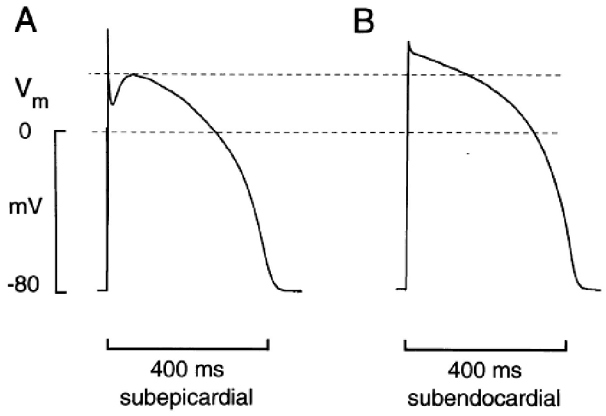

Fig. 6: Action potentials recorded from human myocytes isolated from the subepicardial (A) and the subendocardial (B) layer of the left ventricular anterior wall [19].

The heart is equipped with a network of modified cardiomyocytes that are responsible for spontaneous generation and coordinated propagation of electrical signal through the heart. They constitute the *conduction system* of the heart, whose main components are shown in Fig. 7. Electrical impulses originate in the *sinoatrial node* (which is therefore also called the *pacemaker* of the heart [1]) from which they spread through the atria causing them to contract. Ventricles are electrically insulated from atria by the *cardiac skeleton*, which is a plate of fibrous connective tissue around the valves [1]. The only electrical connection between atria and ventricles is represented by the *atrioventricular bundle* [1] (also known as the *bundle of His* or *His bundle* [15]), arising from the *atrioventricular node*. This node delays the passage of signal to the ventricles in order to let the atria complete their contraction before ventricular contraction begins [1]. The atrioventricular bundle leads into the interventricular septum where it splits into the *right bundle branch* and the *left bundle branch*. Each branch descends the endocardial surface on the corresponding side of the interventricular septum and splits into a fine network of *Purkinje fibres* which

[1] *Membrane potential* (or *transmembrane potential*) is defined as a potential difference between intracellular and extracellular spaces. The sign is given by the convention that the extracellular electrode is used as a reference [15]. Thus, if ψ_i and ψ_e are intra- and extracellular potentials, then the membrane potential $V = \psi_\mathrm{i} - \psi_\mathrm{e}$.

at discrete sites, called the *Purkinje-ventricular muscle junctions*, are in contact with ventricular myocardium [15]. These junctions are situated in the subendocardial layer of myocardium [15] and only through them the electrical signal can pass to the myocardium because, apart from the junctions, Purkinje fibres are isolated from myocardium by thin fibrous sheaths [20, 15]. In ventricular myocardium the activation spreads from cell to cell (by means of the exchange of ions mentioned earlier) until the whole muscular tissue is depolarized.

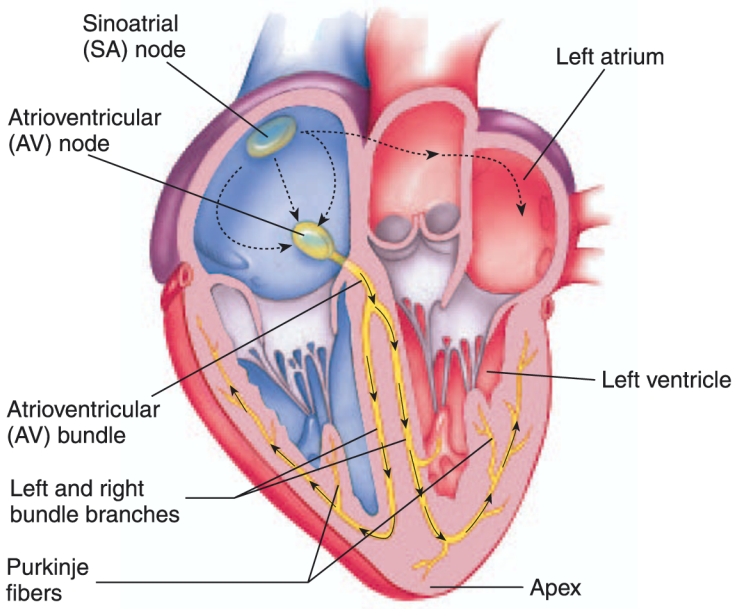

Fig. 7: Schematic representation of the conduction system of the heart [1].

Transition of the bundle branches into the Purkinje network as well as anatomy and location of these structures was thoroughly studied by Stephenson et al. (2017) [21] who, by means of contrast enhanced micro-computed tomography with "spatial resolutions approaching the single cell" [21], obtained accurate three-dimensional representation of the cardiac conduction system in human heart. They observed the right bundle branch "to project anteriorly onto the interventricular septum as a superficial narrow ribbon, which then descended the septum..." The bundle then "became continuous with the Purkinje network," which, as the reconstructions presented in their paper clearly show, was concentrated in the lower parts of the right ventricular cavity.

The structure of the left ventricular conduction branch is somewhat more elaborate, as already described Tawara in 1906 [22] (see Fig. 8). Stephenson et al. (2017) [21] described the left bundle branch proximally as "a broad sheet-like structure draped over and down the left basal surface of the muscular ventricular septum." More distally, then, the bundle "took on a tri-fascicular appearance, permitting identification of the anterior, septal and posterior fascicles." The fascicles appeared as "wide ribbon-like structures running on the endocardial surface," which then "gave rise distally to the Purkinje fibres." They described the Purkinje network in LV as having a "cone-like appearance" and from their graphical reconstructions (see [21]) it is obvious that, except the septum, the fibres are concentrated in the lower parts of the LV, specifically in the subendocardial layer. It was observed by others that septal fascicle in some cases is not separate, but rather formed from smaller branches of the two other fascicles [23].

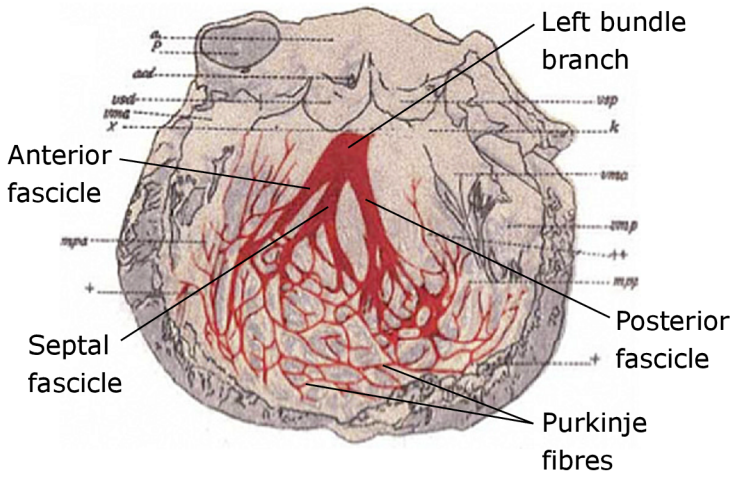

Fig. 8: Drawing from the pioneering work of Tawara (1906) [22] in which he first described the structure of the ventricular conduction system. The left bundle branch divides into the anterior, septal (or middle) and posterior fascicles.

Since the purpose of the Purkinje fibres is to rapidly distribute excitation through the ventricles in order to achieve synchronous contraction, they conduct with much higher velocity than myocardial cells. Kléber et al. (2011) [24] collected 8 different values of conduction velocity from 8 published experimental studies; they range from 1.76 mm $\cdot$ ms^{-1} to 3.50 mm $\cdot$ ms^{-1} and the average is 2.28 mm $\cdot$ ms^{-1}. Conduction velocity in LV myocardium is not only lower, but also highly influenced by the laminar arrangement of myocytes described above in Sec. 2.3. This is evident from the results of Caldwell et al. (2009) [11] who analyzed microstructure and electrical activity in the same volumes of LV tissue. They concluded that conduction velocity is orthotropic with principal directions of propagation coinciding with those determined by the local microstructure (in Fig. 5). The measured conduction velocities were (mean $\pm$ SD): 0.67 ± 0.019 mm $\cdot$ ms^{-1} in $\mathbf{f}$ direction, 0.30 ± 0.010 mm $\cdot$ ms^{-1} in $\mathbf{s}$ direction and 0.17 ± 0.004 mm $\cdot$ ms^{-1} in $\mathbf{n}$ direction. These values agree well with results of many other authors (see a summary in [24]) who, however, generally assumed transversely isotropic conduction in myocardium.

Depolarization of ventricles starts from the locations of Purkinje-muscle junctions. Experimental study by Durrer et al. (1970) [25], which presented contour maps of electrical activation times measured in isolated human hearts, identified three early-activated areas in LV endocardium (see Fig. 9, top row): "(1) an area high on the anterior paraseptal wall just below the attachment of the mitral valve, extending at least 2 cm toward the apex into the region of the anterior papillary muscle; (2) a central area on the left surface of the interventricular septum; (3) the posterior paraseptal area at about one third of the distance from apex to base." According to the authors, this initial activation pattern was consistent among different hearts, but as activation continued, some individual variations occurred (see the bottom row of Fig. 9). The presence of three early-activated areas in LV is in agreement with the above described division of the left bundle branch into three fascicles (Fig. 8). Endocardial activation of the right ventricle was observed to start "about 5 to 10 msec after the onset of the left ventricular cavity potential, or slightly later" [25]. It begins near the insertion of the anterior papillary muscle and in the low anterior part of the right septal surface [25, 15]. This corresponds with the anatomical findings of Stephenson et al. [21] who described that Purkinje fibres supply mainly the apical region of the right ventricle.

A total time necessary for a complete depolarization of both ventricles can be clinically

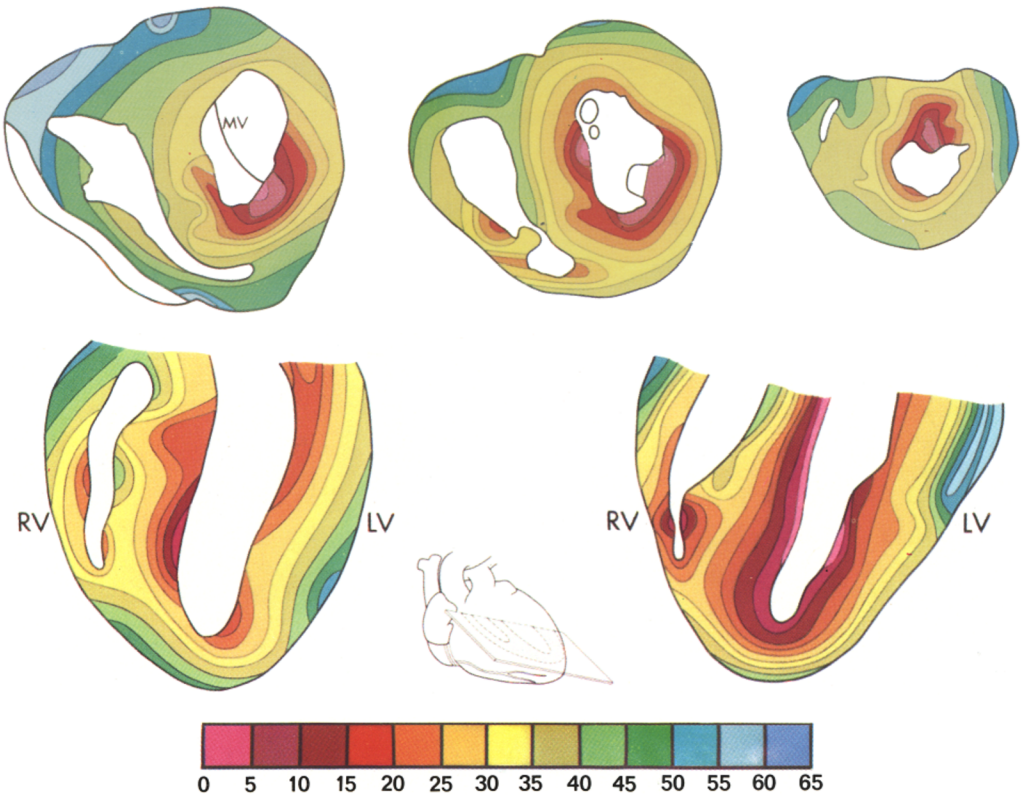

Fig. 9: Isochrone maps of electrical activation times measured in isolated human hearts by Durrer et al. (1970) [25]. Top row: Horizontal sections taken at (from left to right) basal, central, and apical regions of one heart. Locations of the first activated areas (in pink) were consistent between different hearts. Bottom row: Nearly identical sections of two different hearts showing some variation in the activation pattern. Activation times are expressed in milliseconds following the onset of electrical activity in left ventricle. MV: mitral valve, LV: left ventricle, RV: right ventricle.

measured as a duration of the QRS complex on the electrocardiogram [15]. This duration was observed to slightly decrease with increasing age and to be generally longer in men compared to women because men have larger hearts that take longer to depolarize [15]. Specifically, for a group of healthy persons aged 18–29 years Macfarlane et al. [15] report QRS durations (mean ± SD) 96.4 ± 8.6 ms ($n = 265$) and 87.7 ± 7.8 ms ($n = 317$) respectively for men and women, and for persons over 50 years they report 92.7 ± 9.3 ms ($n = 123$) and 87.1 ± 8.7 ms ($n = 79$) respectively for men and women. These values should provide a good estimate of normal ventricular activation times across the population. They are, however, apparently inconsistent with the experiments of Durrer et al. [25] in which total excitation of isolated hearts took only about 65–80 ms (see their Fig. 4). The source of this discrepancy was identified by the latter authors themselves. Their control measurements on dogs' hearts, performed first *in situ* and then after the removal of each heart from the body, revealed that although the isolation does not change the overall pattern of electrical activation, it substantially increases ventricular conduction velocity. Thus the reported activation times (Fig. 9) will be about 20 % higher in a beating heart [25] which means that total excitation will take about the same time as the normal QRS complex, as it should.

The last activated region in ventricles is generally located in the posterobasal portion of the LV free wall or more laterally [25].

3 Motivation and objectives

The normal electrical activation process described in Sec. 2.4 can be disrupted by a wide variety of *conduction defects*. If a conduction defect is characterized by a delay or complete interruption of conduction of electrical stimulus in some part of the heart, it is called a *block* [15]. Thus, we distinguish the *left bundle branch block*, the *right bundle branch block*, the *left anterior fascicular block*, the *left posterior fascicular block* and other blocks, including combined ones which affect more than one conduction branches (see [15] for a list). If conduction through a given part is totally interrupted, the block is called *complete*; if it is only delayed, the block is *incomplete* [15]. The above examples of conduction blocks all belong to the class of the *intraventricular* conduction defects since they all occur at the ventricular level [15]. Analogously, the defects occuring in the atria are called the *intraatrial* defects.

Intraventricular blocks can arise as a consequence of various anatomical or functional lesions in ventricles, including myocardial fibrosis, infarction, cardiomyopathies, coronary artery disease, ischaemia, or hyperkalemia [15]. Even when they are not directly caused by an underlying cardiovascular disease, they are most often accompanied by one or more of them [15, 26]. The degree of reduction of systolic function is then determined by the cumulative impact of all coexisting abnormalities and it might be difficult to correctly assess the contribution of the block alone. Thus there is a danger that the impact of the block will be either underestimated or overestimated. This is especially the case of the complete LBBB, which is the most common conduction defect in patients with heart failure [27].

The LBBB frequently occurs in conjunction with coronary artery disease, hypertension, cardiomyopathy, LV hypertrophy, mitral regurgitation and other abnormalities [26, 27]. The *Comprehensive cardiology* (2010) [15] by Mcfarlane et al. describes the pattern of electrical activation in complete LBBB as follows: "When the conduction of the electrical impulse through the main left bundle branch (or through its two or three subdivisions) is interrupted or severely delayed by any type of disease process, the ventricular excitation wave is conducted through the right bundle branch. Activation will then begin low on the right septal surface, in the region corresponding, on the left side, to the base of the anterior papillary muscle. From there, the wave of excitation spreads to the right ventricle and transeptally to the left ventricle, which is reached from right to left, at a much lower speed, by conduction from one muscular fiber to another." The disrupted activation pattern necessarily leads to asynchronous contraction which reduces an efficiency of LV mechanical function. Smiseth & Aalen (2019) [26] described the mechanism of deterioration of LV contraction as follows: "In LBBB, the early activated septum contracts when the LV lateral wall is fully relaxed, and rather than contributing to LV ejection, septal contraction displaces blood towards the lateral wall that is stretched to abnormally high preload. When the lateral wall is activated, it contracts vigorously according to the Starling mechanism, and displaces blood back towards the septum that is stretched and displaced towards the right ventricle. When the septum is stretched and displaced, it absorbs energy from work performed by the LV lateral wall, which can be assessed as wasted work in the septum." This mechanical dyssynchrony is manifested by enlarged displacements of the LV apex in directions perpendicular to the long axis of the ventricle [28, 29]. This phenomenon is called "apical rocking" and it can be observed on echocardiographic images. It is also hypothesized [26] that the asynchronous contraction due to the LBBB overloads some regions of the ventricular muscle. Increased stresses in

the wall can cause further damage to the ventricle because they alter regional coronary blood flow, increase oxygen consumption and induce tissue remodeling [30].

In order to evaluate the separate impact of LBBB on LV function, several clinical studies have compared LV ejection fraction[1] in patients with *isolated* LBBB (i.e. without evidence of any other heart disease) against healthy individuals; e.g. [32, 33, 34, 35, 36]. Their results are summarized in Table 1 and illustrated in Fig. 10. It can be seen that the reported decrease in mean ejection fraction ranges from 4 % in [33, 36] to as much as 14.2 % in [34]. In the last mentioned study, the mean ejection fraction in the LBBB group even fell below 50 % which is generally considered a sign of LV systolic dysfunction [4]. This slightly contradicts the general belief that normal ejection fraction is usually preserved in isolated LBBB [26] and confirms that the impact of the block on LV performance is currently not entirely clear.

Table 1: Ejection fractions in healthy individuals (Control) and patients with isolated left bundle branch block (LBBB) from 5 clinical studies. Values are means ± SD, n is the number of subjects.

	Control	LBBB
Grines et al. (1989) [32]	62 ± 5 % ($n = 10$)	54 ± 7 % ($n = 18$)
Özdemir et al. (2001) [33]	68 ± 6 % ($n = 65$)	64 ± 6 % ($n = 45$)
Valenti et al. (2012) [34]	63.1 ± 5.3 % ($n = 10$)	48.9 ± 6.6 % ($n = 39$)
Akhtari et al. (2018) [35]	68 ± 6 % ($n = 18$)	56 ± 7 % ($n = 18$)
Aalen et al. (2019) [36]	60 ± 4 % ($n = 11$)	56 ± 6 % ($n = 11$)

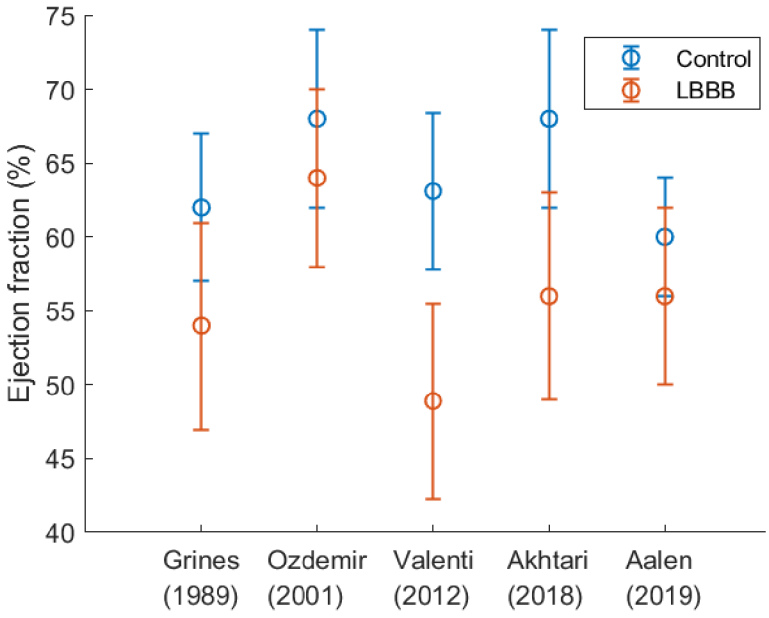

Fig. 10: Mean ejection fractions ± SD in healthy individuals (Control) and patients with isolated left bundle branch block (LBBB) reported by Grines et al. [32], Özdemir et al. [33], Valenti et al. [34], Akhtari et al. [35] and Aalen et al. [36].

[1]Ejection fraction is the volume fraction of blood ejected from the LV per one beat, expressed in percents. It is the most widely used measure of the pumping efficiency of the ventricle and an indicator of the severity of heart failure [31].

The lack of conclusive clinical results encourages the usage of computer models in the study of pathological consequences of LBBB. However, although there are many models in literature investigating the impact of LBBB on ventricular electrophysiology (see a review [37]), simulations of LV mechanics and hemodynamics are scarce. In fact the study by Dou et al. (2009) [38] seems to be the only one that presents the values of ejection fraction for both healthy and LBBB conditions. But their simulated decrease from 55.0 % (healthy) to 21.7 % (LBBB) seems unrealistic compared to the values in Table 1. This discrepancy can probably be attributed to the (over)simplified model which the authors used. For instance, the mechanical behavior of myocardium was modeled as transversely isotropic and linearly elastic which is far from reality [39, 12]. Quarteroni et al. [40] simulated LBBB with much more elaborated model, but their paper was devoted mainly to the numerical techniques used in cardiac computational models and the simulation of LBBB was intended only as a demonstration of the capabilities of their model [40]. It is probably for this reason that they did not present any hemodynamic results of their simulations. Unfortunately, no other computational studies investigating the impact of LBBB on LV mechanics and hemodynamics have been found in literature.

With regard to the above facts, **this thesis aims (i) to develop an electromechanical finite-element (FE) model of human left ventricle capable of simulating ventricular contraction under different conditions and (ii) to employ the model to investigate the impact of isolated LBBB on ventricular hemodynamics, kinematics and wall stress.** The primary goal is the assessment of ejection fractions. Kinematics of the model will be analyzed in order to verify its ability to reproduce the reported changes in LV motions. Stress analysis can yield valuable results because stresses in myocardium cannot be directly measured *in vivo* [30].

It should be added that this thesis extends the previous research [41, 42] on some closely related topics which was conducted by me, my supervisor Jiří Burša and our colleagues from Masaryk University. Within this research, we investigated the importance of experimentally observed transmural[1] differences in electromechanical delay and myocyte shortening velocity for LV function [41] and then we studied the impact of decreased conduction velocity on LV pressure rise during isovolumic contraction [42]. The main results of the latter study were that 50% decrease in transmural conduction velocity prolongs the isovolumic contraction by 18 % and decreases slightly the maximum rate of left ventricular pressure rise. Since the scope of my dissertation topic was originally limited to the investigation of the impact of slowed myocardial conduction on isovolumic contraction phase, the above results already fulfilled the main goals of my research. However, it soon became clear that the simulations of isovolumic contraction are insufficient for evaluation of the consequences of slowed conduction. Moreover, the FE model used in the above studies was too simplistic and its potential applicability for other conduction defects was hardly possible. For these reasons, it was finally decided to start building a new, much more elaborate model of LV which is presented in this thesis and which overcomes many of the limitations of the older model. Since the new model has much broader applicability, we eventually turned our attention to investigating the LBBB which is nowadays more extensively discussed in literature than the reduced conductivity of myocardium. I believe that this topic has greater potential to be further explored by future students and to extend the research activities of our department.

[1]The adjective "transmural", which will occasionally be used throughout this work, means "through the wall of an organ; extending through or affecting the entire thickness of the wall of an organ or cavity" (www.thefreedictionary.com).

4 Calculation of electrical activation maps

From the computational viewpoint, the quantities of interest in this thesis, as specified in the goals formulated in the previous chapter, can be regarded as outcomes from the simulations of LV mechanics. Changes in LV volume, which determine the ejection fraction, as well as wall stresses arise primarily as a result of the muscle contraction which therefore, in some way, must be incorporated in the simulations. Regardless of the chosen approach, it is always necessary to directly prescribe the spatial distribution of the beginning of contraction in the computational domain (possibly uniform in some simplified models). In a heart this onset of contraction is determined mainly by the time of electrical activation which, as already discussed in Sec. 2.4, is not uniform throughout the LV myocardium. Thus, if the timing of contraction cannot be prescribed from some other data, the simulation of mechanics must be preceded by a simulation of electrical activity from which the distribution of electrical activation times (activation maps) can be obtained.

In this chapter, first the computational domain will first be specified, which will then be used throughout the rest of this thesis. Afterwards, the mathematical model of electrical activity in cardiac tissue will be introduced and the way of obtaining the activation maps from its solution will be explained. The rest of the chapter will be dedicated mostly to the description of individual steps of FE solution of the model. In the course of this description a FE mesh will be presented which will later be used also for the simulations of LV mechanics. In the end of the chapter, two calculated activation maps are presented, one representing a normal healthy activation and the other representing a ventricle with LBBB.

4.1 Computational domain

An essential requirement for mathematical solution of any physical problem described in space is a specification of the spatial computational domain Ω. Combining requirements given by Truesdell [43] and Quarteroni [40] (and assuming that we describe problems in 3 dimensions), we can characterize domain as a regularly open, bounded and connected subset of a 3-dimensional Euclidean space. In order to make applicable the divergence theorem (and other integral theorems), it is also commonly assumed that the boundary $\partial\Omega$ of a domain is piecewise smooth.

In this work, Ω will be specified on the basis of the publicly available[1] "mean shape model" of LV which was created by Bai et al. [44] and is shown in Fig. 11A. The model represents an average normal human LV at end-diastole and was calculated from high-resolution magnetic resonance images of over 1000 healthy subjects (see [44] for details). It is provided as a set of points in a 3-dimensional Cartesian space $\mathbb{R}^3$ along with a set of triangular elements which connect the points and together form the closed surface depicted in Fig. 11A. In order to improve quality of future FE meshes and also to facilitate prescription of kinematic boundary conditions at the base (which is highly irregular in the original model), the surface was first smoothed and then its basal portion was cut out by a plane perpendicular to the long axis of LV.[2] The first of these operations was realized in software GOM Inspect 2018, while the second in Ansys ICEM CFD 2021 R2.

[1] http://wp.doc.ic.ac.uk/wbai/data

[2] The long axis is the line that passes through the center of the mitral valve orifice and the left ventricular apex [45]. In Fig. 11A it is represented by the blue z axis.

The resulting surface, which is shown in Fig. 11B, is the union of endocardial (Γ_{endo}), epicardial (Γ_{epi}) and basal (Γ_{base}) surfaces. Points inside this union (not lying on the surfaces) constitute the reference configuration Ω and the union itself forms the boundary, i.e. $\partial\Omega = \Gamma_{\text{endo}} \cup \Gamma_{\text{epi}} \cup \Gamma_{\text{base}}$. The volume of the LV cavity (enclosed by Γ_{endo} and the basal plane) in the final model is approximately 137 ml which is well within the range of normal values of end-diastolic volume [3].

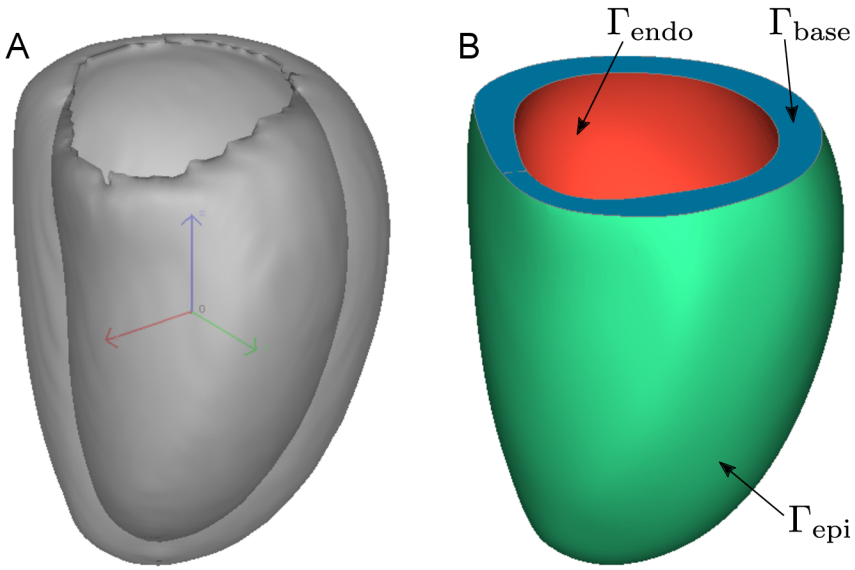

Fig. 11: (A) The original model representing an average normal human LV at end-diastole. Transparent view shows the contour of the endocardial surface as well as the global Cartesian coordinate system. The global z axis (blue) coincides with the long axis of the ventricle, x axis (red) points toward the septum, and y axis (green) points toward the anterior wall. Position of the origin on the long axis is arbitrary and has no particular meaning. (B) The resulting surface is the union of endocardial (Γ_{endo}), epicardial (Γ_{epi}) and basal (Γ_{base}) surfaces.

Since we are aiming toward FE solutions, we can already expect that boundaries of the eventual FE meshes will not perfectly coincide with $\partial\Omega$, which means that numerical solutions will actually be realized on a domain different from Ω. We will denote such discretized domain as Ω_h [40] where h is a parameter characterizing the spacing of the mesh (see below). The set Ω_h is an approximation of Ω induced by some mesh $\mathcal{T}_h$. A mesh is a collection of *finite elements* which, in the present case, are closed subsets of $\mathbb{R}^3$ with sufficiently simple shape and specific topology.[1] A generic element in $\mathcal{T}_h$ will be denoted by K. For each $K \in \mathcal{T}_h$ we can define its diameter $h_K := \max\{\|x - y\| \mid x, y \in K\}$, which is the maximum of distances of all possible pairs of points from K. We can then specify $h := \max\{h_K \mid K \in \mathcal{T}_h\}$, which is the maximum diameter of all elements in the mesh. Given $\mathcal{T}_h$, the discretized domain Ω_h is defined as the interior of the union of all members of $\mathcal{T}_h$ [40], i.e.:

$$\Omega_h := \operatorname{int}\left(\bigcup_{K\in\mathcal{T}_h} K\right). \tag{4.1}$$

The closure $\overline{\Omega}_h$ of Ω_h is the set inside the parentheses in (4.1). It safisfies: $\overline{\Omega}_h = \Omega_h \cup \partial\Omega_h$.

[1] Complete list of conditions on meshes and a formal definition of a finite element provides, e.g., Ciarlet [46].

4.2 The monodomain model, activation maps

Propagation of electrical activation in myocardial tissue is mathematically described by the so-called *monodomain model*, or *monodomain equation*, which can be written as[1] [18]

$$\frac{\partial V}{\partial t} = \operatorname{div}\left(\mathbf{D}\nabla V\right) - J_{\text{ion}}\left(V, \mathbf{u}\right) + J_{\text{stim}}\,, \tag{4.2}$$

where V is the membrane potential, t is time, $\mathbf{D}$ is the diffusion tensor, J_{ion} represents the ionic current through membrane channels, J_{stim} represents the stimulus current and $\mathbf{u}$ is a vector of cell-level variables, such as ionic concentrations and membrane gating variables.[2] A solution of the monodomain equation is a transmembrane-potential mapping

$$V\colon\ \langle 0, T\rangle \times \Omega \to \mathbb{R}\,, \tag{4.3}$$

which assigns to each point $\mathbf{x}$ in the spatial domain Ω and each time t from some interval $\langle 0, T\rangle$, with $T > 0$, the value of the membrane potential $V(t, \mathbf{x})$. When such V is calculated for a time interval of one cardiac cycle, we can also interpret it as a mapping which assigns to each point $\mathbf{x} \in \Omega$ one complete action potential. This calculated action potential is a function, which assigns to each $t \in \langle 0, T\rangle$ the value $V(t, \mathbf{x})$. Following [48], we will denote such function $V(\,\cdot\,, \mathbf{x})$. Thus, the action potential at $\mathbf{x}$ is a function

$$V(\,\cdot\,, \mathbf{x}) \coloneqq (t \mapsto V(t, \mathbf{x}))\colon\ \langle 0, T\rangle \to \mathbb{R}\,. \tag{4.4}$$

Alternatively, (4.3) can be interpreted as a mapping which assigns to each time $t \in \langle 0, T\rangle$ a scalar field describing a distribution of membrane potential in Ω. Following [48], we will denote such field $V(t, \,\cdot\,)$. It is defined as

$$V(t, \,\cdot\,) \coloneqq (\mathbf{x} \mapsto V(t, \mathbf{x}))\colon \Omega \to \mathbb{R}\,. \tag{4.5}$$

We will later need also a mapping which assigns the scalar field (4.5) to each time t. Following [48], we will identify this mapping with (4.3) which means that the same symbol, V, will be used for both. Thus, V can be interpreted also as:

$$V \coloneqq (t \mapsto V(t, \,\cdot\,))\colon\ \langle 0, T\rangle \to \operatorname{Map}(\Omega, \mathbb{R})\,, \tag{4.6}$$

where $\operatorname{Map}(\Omega, \mathbb{R})$ is the set of all mappings from Ω to $\mathbb{R}$ [48].

When V is calculated, the action potentials are known at all points $\mathbf{x} \in \Omega$. Activation time at $\mathbf{x}$ can then be defined as the time when the calculated action potential $V(\,\cdot\,, \mathbf{x})$ reaches the threshold value during the early rapid depolarization. Electrical activation in the whole domain Ω can then be described by an electrical activation map

$$\operatorname{eac}\colon \Omega \to \mathbb{R}\,, \tag{4.7}$$

[1] Equation given here assumes that activation takes place in a fixed region Ω, which is only an approximation of the real conditions. More general form of the equation (e.g. [47]) takes into account also motions of the tissue, but then it is not possible to fully uncouple the simulation of electrophysiology from the simulation of mechanics.

[2] J_{ion} and J_{stim} are not actual currents, because their unit is $\mathrm{V}\cdot\mathrm{s}^{-1}$. Rather, they are scaled currents [18], obtained from the ionic current per unit membrane area, j_{ion} ($\mathrm{A}\cdot\mathrm{m}^{-2}$), and the stimulus current per unit volume, i_{stim} ($\mathrm{A}\cdot\mathrm{m}^{-3}$), as: $J_{\text{ion}} = j_{\text{ion}}/C_{\text{m}}$ and $J_{\text{stim}} = i_{\text{stim}}/(\beta\, C_{\text{m}})$, where C_{m} is the membrane capacitance per unit area ($\mathrm{F}\cdot\mathrm{m}^{-2}$) and β is the membrane surface-to-volume ratio (m^{-1}).

whose value $\mathrm{eac}(\mathbf{x})$ is the calculated electrical activation time at $\mathbf{x}$, for all $\mathbf{x} \in \Omega$. Function (4.7) can then be used to prescribe the distribution of the onset of contraction in the subsequent simulation of mechanics.

Returning to the quantities appearing in the monodomain equation (4.2), the diffusion tensor (or diffusivity tensor) $\mathbf{D}$ governs the velocity of propagation of depolarization in individual directions. It is given by [49]

$$\mathbf{D} \coloneqq D_{\mathbf{f}}\, \mathbf{f} \otimes \mathbf{f} + D_{\mathbf{s}}\, \mathbf{s} \otimes \mathbf{s} + D_{\mathbf{n}}\, \mathbf{n} \otimes \mathbf{n}\,, \tag{4.8}$$

where $D_{\mathbf{f}}$, $D_{\mathbf{s}}$, $D_{\mathbf{n}}$ are diffusion coefficients (or diffusivities) in the three material directions depicted in Fig. 5. Generally, the coefficients are functions of coordinates. In a purely diffusive system, velocity in a particular direction should theoretically be proportional to the square root of the corresponding diffusion coefficient, but in the monodomain equation it is influenced also by the ionic term $J_{\mathrm{ion}}\,(V, \mathbf{u})$ [49]. In FE simulations, velocity depends also on the mesh density, time step and on the method of interpolation of J_{ion} over an element [50, 47]. Thus a common approach to determine suitable values of diffusion coefficients for a computational model is to tune the coefficients to give velocities that are close to the real values [49]. But even then there are differences between locally measured velocities because velocity on the front of the propagating depolarization wave depends also on the curvature of the front [49], which is of course variable. This dependence can be observed not only in simulations, but also in real cardiac tissue [49].

The exact form of the ionic term $J_{\mathrm{ion}}\,(V, \mathbf{u})$ is determined by a particular ionic model of cardiac cell, which is expected to be used in conjunction with the monodomain model. All cell models are systems of ordinary differential equations expressed in terms of time-dependent cell-level variables arranged in vector $\mathbf{u}$. Many different models have been proposed in literature and they vary considerably in the number of parameters they use.[1] The number of parameters generally reflects the amount of quantities a particular model is designed to reproduce, but it also determines the accuracy of their reproduction. Specifically, all cell models provide description of the cardiac action potential whose key characteristic is the early rapid depolarization phase. The fact that this particular characteristic must be replicated by all models (in more or less the same way) has huge consequences because it makes large-scale simulations (involving whole ventricle(s)) extremely computationally demanding [17]. The reason behind this fact is that the depolarization phase is very fast and it occurs on very small lengths. It lasts only about 1 ms [17] and if we consider that conduction velocity in myocardium is usually between 0.17 $\mathrm{m \cdot s^{-1}}$ and 0.67 $\mathrm{m \cdot s^{-1}}$(cf. Sec. 2.4), it follows that the depolarization wavefront propagating through the tissue is only about 0.17–0.67 mm thick in the direction of propagation (conduction velocity $\times$ 1 ms). This means that in order to reproduce the evolution of V with sufficient accuracy, FE analyses should use element sizes of the order of 0.1 mm [17, 18]. Similar restrictions are imposed also on the time step size, which should be of the order of 0.01 mm [17, 18] (and probably even smaller if fully explicit time discretization is used [51]). These restrictions eventually result in enormous requirements on computer memory and computational times and represent reasons why many published computational studies actually involve only small blocks of tissue with dimensions not exceeding a few centimeters [17].

The last term in (4.2), J_{stim}, represents the stimulus current which serves to initiate the growth of V in selected portions of the model (first activated regions). It is usu-

[1] For example, Colli Franzone et al. [17] list in their Table 2.2 on p. 44 in total 24 frequently used models with numbers of parameters ranging between 3 and 50.

ally prescribed only during the first few milliseconds of simulation. Once V exceeds the threshold potential in the stimulated regions (and possibly in their close neighborhoods), the stimulus can be removed (set to zero) because depolarization will propagate without the need of any external source.

4.3 Artificial ionic model

The fact that the sole purpose of the simulations of electrophysiology in this work is to obtain the electrical activation maps for the subsequent mechanical analyses implies that it is actually not necessary to simulate the whole action potentials. The initial depolarization phase is sufficient which means that the simulated period should be only about 100 ms long (the duration of the QRS complex). In spite of that, a solution of the traditional monodomain system, composed of the monodomain equation and a model of cardiac cell, eventually turned out to be beyond the capabilities of hardware available to the author of this thesis. The first attempts of the author involved a simple three-parameter cell model proposed by Bueno-Orovio et al. [16]. But although the FE computer code using this model was successfully implemented, it was impossible to simulate the whole depolarization phase in the whole of Ω. The simplicity of the Bueno-Orovio model did not change the fact that the FE mesh with suitable diameter $h = 0.2$ mm contained more than 120 million linear tetrahedrons. The requirements on the computational time with such a dense mesh became excessive and so the solution could not be obtained. Attempts have also been made to simulate the depolarization with larger elements in order to reduce the computational cost. This idea was motivated by the realization that the accuracy of the simulated waveforms is not really important in the present case because the only results that will be further utilized are the instants when the potentials reach the threshold. But these attempts also failed because FE solutions of the monodomain equation generally overestimate the conduction velocities when the mesh size is not sufficiently fine [47]. The necessity to achieve velocities as low as $0.17\ \mathrm{m \cdot s^{-1}}$ precluded the use of any coarser mesh. In fact, the velocity of $0.17\ \mathrm{m \cdot s^{-1}}$ could not be achieved even with the original mesh with the size of 0.2 mm; even in that case the lowest achievable value was only slightly below $0.30\ \mathrm{m \cdot s^{-1}}$ which means that the electrical propagation in the model would effectively be transversely isotropic rather than orthotropic.

All the above problems finally led to the idea of replacing a true ionic model by an artificial one that would be specifically designed to generate a gradual rather than the steep increase of potential. This approach can be justified by the fact that virtually any sort of simulated (pseudo-)activation wave that would travel throughout the computational domain with prescribed conduction velocities would serve the purpose of this thesis just as well as the complete monodomain system with an appropriate model of human cardiac cell. The artificial model was finally formulated as a real-valued function of the (similarly unrealistic) normalized dimensionless potential v (used e.g. in [18]), which is supposed to rise from 0 to 1 during the depolarization phase. The function is defined by:

$$J_{\mathrm{ion}}(v) \coloneqq \begin{cases} \alpha(v^2 - v) & \text{for} \quad v \in (0,1) \\ 0 & \text{for} \quad v \in \mathbb{R} \setminus (0,1)\,, \end{cases} \tag{4.9}$$

where $\alpha > 0$ (s^{-1}) is a parameter controlling the rate of growth of v. As can be seen from Fig. 12, by choosing a suitable value for α it is possible to obtain a response with sufficiently slow growth, which means that the extreme discretization requirements imposed by standard ionic models will no longer apply. Thus, it will be possible to use

computationally acceptable FE meshes as well as time steps. The procedure leading to the curves in Fig. 12 is explained below. Since V was replaced by v and J_{ion} was defined

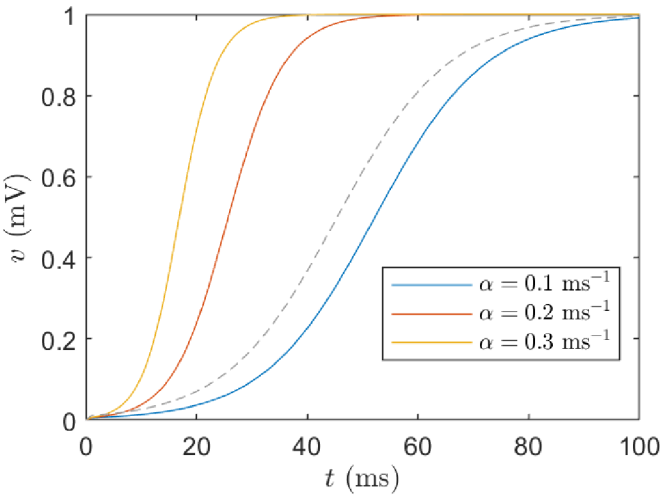

Fig. 12: A graph of dimensionless pseudo-potentials v against time t for different choices of the rate parameter α in (4.9). The response was initiated by the stimulus $J_{\text{stim}} = 0.005$ ms^{-1} which was applied during the time period 0–1 ms. The time step was $\Delta t = 0.5$ ms. Dashed gray curve shows the response for $\alpha = 0.1$ ms^{-1} after J_{stim} was doubled (for illustrative purposes only).

only in terms of v (without any other "cell-level" variables $\mathbf{u}$), the monodomain equation (4.2) should be updated accordingly as follows:[1]

$$\frac{\partial v}{\partial t} = \operatorname{div}(\mathbf{D}\nabla v) - J_{\text{ion}} \circ v + J_{\text{stim}}\,. \tag{4.10}$$

This equation describes the propagation of potential in tissue; when the goal is to describe only the action potential of a single cell, the corresponding equation can be obtained, formally, by omitting the diffusion term from (4.10). The equation then reads:[2]

$$\frac{\mathrm{d}v}{\mathrm{d}t} = -\,J_{\text{ion}} \circ v + J_{\text{stim}}\,, \tag{4.11}$$

where v and J_{stim} are understood to be independent of the spatial variable (unlike in (4.10)) and J_{ion} is defined by (4.9). Equation (4.11) together with the initial condition $v(0) = 0$ and a suitably chosen stimulus function J_{stim} represents an initial value problem which can be solved using, e.g., the backward Euler method [40]. To do so, we choose a time step $\Delta t > 0$ and define a sequence of times $(t_0, t_1, \ldots, t_n)$ by the rule $t_k := k\,\Delta t$. Then, the approximate solutions v_k and v_{k+1} at times t_k and t_{k+1}, respectively, are related by:

$$\frac{v_{k+1} - v_k}{\Delta t} = -\,J_{\text{ion}}(v_{k+1}) + J^2_{\text{stim},k+1}\,, \tag{4.12}$$

[1]The mapping $J_{\text{ion}} \circ v$ in (4.10) is the composite of J_{ion}, given by (4.9), and the unknown solution $v\colon \langle 0, T\rangle \times \Omega \to \mathbb{R}$. Precisely, it is defined by $(J_{\text{ion}} \circ v)(t, \mathbf{x}) := J_{\text{ion}}(v(t, \mathbf{x}))$ for all $t \in \langle 0, T\rangle$ and $\mathbf{x} \in \Omega$.

[2]Eq. (4.11) is basically a version of the Hodgkin-Huxley electrical circuit model of the cellular membrane (see e.g. [17], Sec. 2.7) which models the membrane as an electric circuit with capacitor and resistor connected in parallel. The model expresses the current conservation law which states that the applied current is given by the sum of the capacitive and ionic currents.

where $J_{\text{stim},k+1}$ is the stimulus applied at t_{k+1}. Provided that v_k is known, v_{k+1} can be readily expressed from (4.12) using the definition (4.9). This procedure was used to obtain the curves in Fig. 12; concrete data which were used in calculations are specified in the figure and its caption.

When the artificial ionic model proposed here is used in the monodomain model, a particular point in the domain can be considered activated when v reaches some arbitrary value. For the subsequent simulations, this "pseudo-threshold potential" was chosen to be 0.5.

The stimulus current J_{stim} that appears in the monodomain equation (4.10) plays exactly the same role as the stimulus current used in the single-cell simulations described above. The only difference is that, in the monodomain equation, J_{stim} is dependent on the spatial variable, just like v.

4.4 Initial-boundary value problem

Equation (4.10) is defined in space and time, which means that its solution requires specification of boundary and initial conditions. Here, we will assume that the pseudo-potential v is initially zero (the resting value) and, following [47, 18], that no current flows across the boundary during the whole time interval (i.e. the tissue is electrically insulated). If we additionally assume that J_{ion} is given by (4.9) and that J_{stim} is sufficiently regular, we can formulate the following initial-boundary value problem [52]: Find $v\colon \langle 0,T\rangle \times \Omega \to \mathbb{R}$ such that

$$\begin{cases} \dfrac{\partial v}{\partial t} = \operatorname{div}(\mathbf{D}\nabla v) - J_{\text{ion}} \circ v + J_{\text{stim}} & \text{in } (0,T)\times\Omega \\ (\mathbf{D}\nabla v)\cdot\mathbf{n} = 0 & \text{in } (0,T)\times\partial\Omega \\ v(0) = 0 & \text{in } \Omega\,, \end{cases} \tag{4.13}$$

where $\mathbf{n}$ is the outward unit normal to the boundary $\partial\Omega$. The second line of (4.13) represents the homogeneous Neumann boundary condition, while the third represents the initial condition. In the initial condition, v is used in the sense of (4.6).

4.5 Weak formulation

Since it is impossible to obtain a solution of (4.13) in closed (explicit) form, an approximate solution will be sought using the FE method. However, solutions obtained by the FE method are generally not differentiable on the boundaries of elements (only continuity is guaranteed) and it is clear that such solutions cannot be obtained from eq. $(4.13)_1$ because it requires the existence of spatial derivatives of v at all points in Ω. In order to extend the class of potential solutions, we must develop the *weak formulation* of the problem (4.13) [40]. To this end, we express the governing equation $(4.13)_1$ at a particular time t, multiply the result by a test function[1] u and integrate over Ω [40]. We obtain:[2]

$$\int_\Omega \dot{v}(t)\,u = \int_\Omega \operatorname{div}(\mathbf{D}\nabla v(t))\,u - \int_\Omega (J_{\text{ion}}\circ v(t))\,u + \int_\Omega J_{\text{stim}}(t)\,u\,, \tag{4.14}$$

[1] A *test function*, in the present meaning, is an infinitely differentiable function $f\colon \Omega\to\mathbb{R}$ with compact support in Ω. The support of f, denoted $\operatorname{Supp} f$, is the closure of the set where the function takes values different from zero, i.e. $\operatorname{Supp} f \coloneqq \overline{\{\mathbf{x}\in\Omega \mid f(\mathbf{x})\neq 0\}}$. A function f is said to have a compact support in Ω if there exists a compact set $C\subset\Omega$ such that $\operatorname{Supp} f \subset C$. A compact set $C\subset\mathbb{R}^3$ is a a set which is closed and bounded. The space of all test functions is usually denoted by $\mathcal{D}(\Omega)$. See [40] for details.

[2] $v(t)$ in (4.14) is a member of $\operatorname{Map}(\Omega,\mathbb{R})$; see (4.6).

where $\dot{v}(t)$ denotes the time derivative. Using the product rule for divergence, the divergence theorem[1] and the boundary condition $(4.13)_2$, the first integral on the right-hand side of (4.14) can be rewritten as

$$\begin{aligned}\int_\Omega \operatorname{div}(\mathbf{D}\nabla v(t))\, u &= \int_\Omega \operatorname{div}(u\,\mathbf{D}\nabla v(t)) - \int_\Omega \nabla u \cdot (\mathbf{D}\nabla v(t)) \\ &= \int_{\partial\Omega} u\,(\mathbf{D}\nabla v(t)) \cdot \mathbf{n} - \int_\Omega \nabla u \cdot (\mathbf{D}\nabla v(t)) \\ &= -\int_\Omega \nabla u \cdot (\mathbf{D}\nabla v(t))\,.\end{aligned} \tag{4.15}$$

Using this identity in (4.14), we get

$$\int_\Omega \dot{v}(t)\, u + \int_\Omega \nabla u \cdot (\mathbf{D}\nabla v(t)) = -\int_\Omega (J_{\text{ion}} \circ v(t))\, u + \int_\Omega J_{\text{stim}}(t)\, u\,. \tag{4.16}$$

This equation admits more solutions than the original equation $(4.13)_1$ which required the existence of second-order derivatives of $v(t)$, while the above equation contains only first derivatives. However, a more significant extension can be achieved if we replace all classical derivatives in (4.16) by those *in the sense of distributions*[2] and then reinterpret $v(t)$ and u as members of the first-order Sobolev space $H^1(\Omega)$.[3] After doing so, all integrals in (4.16) will still be meaningful but we will search for solution in much larger space $H^1(\Omega)$, which contains also all kinds of functions typically encountered in the FE analyses [40]. The resulting problem is called the *weak formulation* of the original problem (4.13) and reads [52]: Find $v : \langle 0, T\rangle \to H^1(\Omega)$ such that $v(0) = 0$ and for each $t \in (0, T)$ it holds that

$$\int_\Omega \dot{v}(t)\, u + \int_\Omega \nabla u \cdot (\mathbf{D}\nabla v(t)) = -\int_\Omega (J_{\text{ion}} \circ v(t))\, u + \int_\Omega J_{\text{stim}}(t)\, u \quad \forall u \in H^1(\Omega)\,. \tag{4.17}$$

4.6 Galerkin approximation

The weak problem (4.17) can be approximated if we replace $H^1(\Omega)$ by its suitably chosen finite-dimensional subspace $\mathcal{V}_h$ with dimension N_h. If such approximation is made, we can choose a basis $(\psi_1, \ldots, \psi_{N_h})$ of $\mathcal{V}_h$ and expand $v(t)$ with respect to the basis:

$$v(t) = \sum_{j=1}^{N_h} v_j(t)\, \psi_j\,. \tag{4.18}$$

It can be seen from this expansion, that the unknown solution is now uniquely determined by a finite family of real-valued functions $v_1, \ldots, v_{N_h}$. Thus the weak problem which

[1] Both the product rule for divergence and the divergence theorem can be found, e.g., in the book by Truesdell [43]. The former is on p. 329 and the latter on p. 181.

[2] Differentiation *in the sense of distributions* is an abstract algebraic operation which extends the classical differentiation of functions. Unlike the classical differentiation, it can be applied on any square-integrable function $f\colon \Omega \to \mathbb{R}$. To each such f we can naturally assign a *distribution* T_f, which is a linear and continuous functional on the space $\mathcal{D}(\Omega)$ formed by all infinitely differentiable functions with compact support. Generalized differentiation is then defined as an operator on the space of all distributions $\mathcal{D}'(\Omega)$, which is the topological dual space of $\mathcal{D}(\Omega)$. For the definition and details, see [40].

[3] Sobolev space $H^1(\Omega)$ is the space of all square-integrable functions from Ω to $\mathbb{R}$ whose first partial derivatives (in the sense of distributions) are also square-integrable. Square-integrable function is a measurable function f for which $\int_\Omega f^2 < \infty$. The space of all square-integrable functions on Ω is denoted as $L^2(\Omega)$. See [40] for details.

required to find a mapping $v : \langle 0, T\rangle \to H^1(\Omega)$ is now replaced by a problem of finding a finite family of functions $v_1, \ldots, v_{N_h}$ from $\langle 0, T\rangle$ to $\mathbb{R}$. Moreover, any test function $u \in \mathcal{V}_h$ can be expressed with respect to the basis in the same way as $v(t)$ in (4.18). If we substitute such expansion into (4.17), it can be readily seen that the equation is satisfied for all members of $\mathcal{V}_h$ if and only if it is satisfied by the basis functions. Thus it is sufficient to require that the equation (4.17) holds for the basis functions because then it holds for any other function in $\mathcal{V}_h$. The resulting problem is called the *Galerkin approximation* of (4.17). Provided that the space $\mathcal{V}_h$ and its basis $(\psi_1, \ldots, \psi_{N_h})$ are given, the problem can be expressed as follows [52]: Find a family of functions $v_1, \ldots, v_{N_h}$ from $\langle 0, T\rangle$ to $\mathbb{R}$ satisfying $v_j(0) = 0$, such that the mapping $v : \langle 0, T\rangle \to H^1(\Omega)$ defined by $v(t) \coloneqq \sum_{j=1}^{N_h} v_j(t)\, \psi_j$ satisfies, for all $t \in (0, T)$, the following condition:

$$\int_\Omega \dot{v}(t)\, \psi_i + \int_\Omega \nabla\psi_i \cdot (\mathbf{D}\nabla v(t)) = -\int_\Omega (J_{\text{ion}} \circ v(t))\, \psi_i + \int_\Omega J_{\text{stim}}(t)\, \psi_i \qquad \forall i \in \{1, \ldots, N_h\}\,. \quad (4.19)$$

The Galerkin problem (4.19) represents a spatial discretization, or semi-discretization (because time variable has not yet been discretized). Formally, (4.19) is a system of N_h ordinary differential equations for determination of the unknown functions $v_1, \ldots, v_{N_h}$. The system is nonlinear because of the nonlinear definition of J_{ion} by (4.9).

4.7 Finite element approximation

The finite element method is a specific way of constructing the subspaces $\mathcal{V}_h$ in the Galerkin approximation (4.19) [52]. Such spaces are then called *finite element spaces* and the subscript h refers to the maximum of diameters of all elements in the mesh (cf. Sec. 4.1). A particular form of $\mathcal{V}_h$ is determined by the mesh $\mathcal{T}_h$ chosen for the solution of a given problem. Since there are many types of meshes, different approaches for the construction of $\mathcal{V}_h$ exist (see [46]). Thus, it seems appropriate at this point to introduce the mesh which was finally used for the solution of the problem described in this chapter. That mesh is shown in Fig. 13. It is composed of quadratic tetrahedral elements with diameters ≤ 2 mm. Tetrahedral shape was chosen because, as already mentioned in Sec. 4.2, conduction velocity is dependent on mesh density which implies that the density should not vary considerably between different regions or in different directions. Tetrahedral mesh is more appropriate in this respect than hexahedral, owing to the complicated shape of the domain Ω. Besides, the same type of element is suitable also for the subsequent simulation of contraction and, as a matter of fact, the mesh in Fig. 13 was eventually used for both kinds of simulations. It was selected, after many trials, as an appropriate mesh which gave converged results in the simulations of mechanics but at the same time was not overly computationally expensive. Afterwards, it was verified that the same mesh is capable of reproducing the whole required range of conduction velocities if the rate parameter α in the artificial current (4.9) is chosen sufficiently low and the diffusion coefficients are properly adjusted. Thus the simplifications introduced to the monodomain model by adoption of the artificial current made it possible to employ the same mesh for both kinds of simulations.

The mesh in Fig. 13 is based on the *isoparametric* formulation of elements which is a general and efficient approach for construction of FE meshes [46]. In this formulation, all elements in the mesh are generated from a single *reference element* by a suitable geometric transformation. Specifically, for the tetrahedral mesh $\mathcal{T}_h$ used here, every element

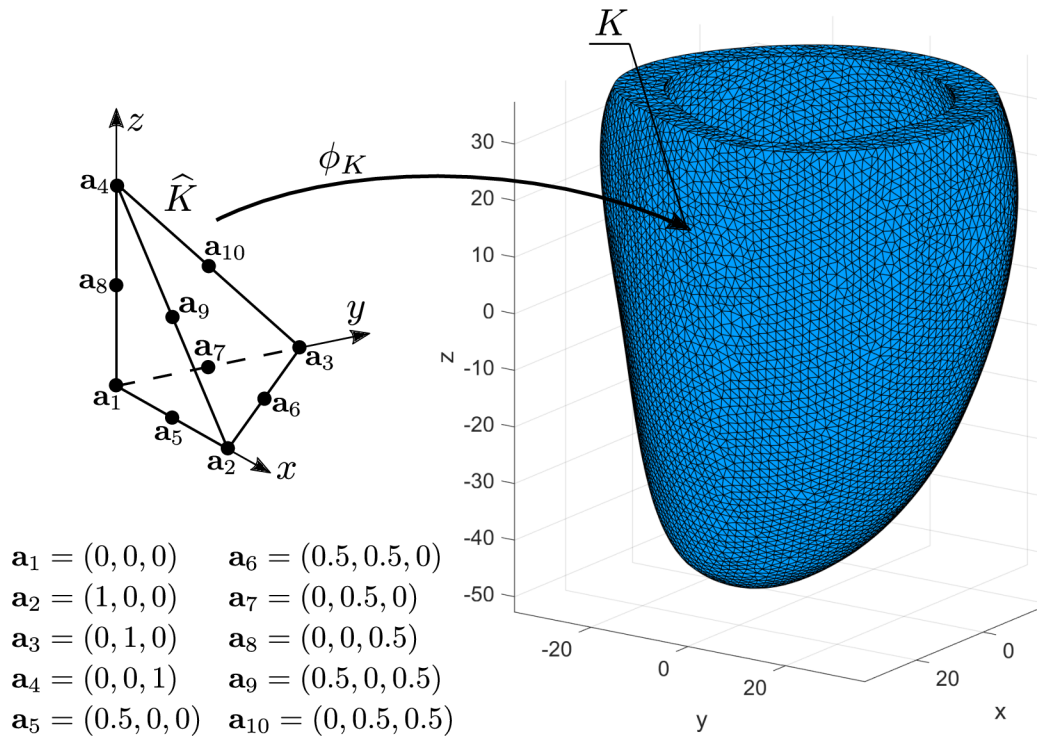

$\mathbf{a}_1 = (0,0,0)$ $\quad \mathbf{a}_6 = (0.5,0.5,0)$
$\mathbf{a}_2 = (1,0,0)$ $\quad \mathbf{a}_7 = (0,0.5,0)$
$\mathbf{a}_3 = (0,1,0)$ $\quad \mathbf{a}_8 = (0,0,0.5)$
$\mathbf{a}_4 = (0,0,1)$ $\quad \mathbf{a}_9 = (0.5,0,0.5)$
$\mathbf{a}_5 = (0.5,0,0)$ $\quad \mathbf{a}_{10} = (0,0.5,0.5)$

Fig. 13: A quadratic tetrahedral mesh with maximum element diameter $h = 2$ mm. The mesh was generated in software Ansys ICEM CFD 2021 R2 and subsequently transferred into Matlab R2021b in which the graphical representation shown above was produced. Each element K in the mesh originates as an image $\phi_K(\widehat{K})$ of the reference element $\widehat{K}$ by means of the transformation map ϕ_K. The reference element is a unit tetrahedron in $\mathbb{R}^3$ with nodes $\mathbf{a}_1, \ldots, \mathbf{a}_{10}$.

$K \in \mathcal{T}_h$ can be obtained from the reference unit tetrahedron $\widehat{K}$ (Fig. 13) by means of a transformation $\phi_K \colon \widehat{K} \to \mathbb{R}^3$ which satisfies $\phi_K(\widehat{K}) = K$. (This transformation will be specified later in this section.) Formally, the reference element is a closed subset of $\mathbb{R}^3$ given by:

$$\widehat{K} := \{(x,y,z) \in \mathbb{R}^3 \mid x,y,z \geq 0\,;\; x+y+z \leq 1\}\,. \tag{4.20}$$

If the transformation ϕ_K is known for a particular $K \in \mathcal{T}_h$, the integral of any function $f \colon K \to \mathbb{R}$ can be replaced by an integral on $\widehat{K}$ using the familiar transformation formula

$$\int_K f = \int_{\widehat{K}} |\det(\nabla \phi_K)| (f \circ \phi_K)\,. \tag{4.21}$$

The transformed integral is easier to evaluate because the shape of $\widehat{K}$ is simple in contrast to the elements in the mesh which are irregular and can have curved faces.

Transformation maps also enable a particularly simple construction of the FE space $\mathcal{V}_h$, using polynomials defined on $\widehat{K}$ [46]. The construction starts with the space $\mathbb{P}_2$ of all quadratic polynomials defined on $\mathbb{R}^3$, i.e.:

$$\begin{aligned}\mathbb{P}_2 := \{p \colon \mathbb{R}^3 \to \mathbb{R} \mid p(x,y,z) &= a_1 + a_2 x + a_3 y + a_4 z + a_5 xy + a_6 yz + a_7 xz \\ &+ a_8 x^2 + a_9 y^2 + a_{10} z^2 \quad \forall x,y,z \in \mathbb{R}; \text{with } a_1, \ldots, a_{10} \in \mathbb{R}\}\,.\end{aligned} \tag{4.22}$$

Any $p \in \mathbb{P}_2$ can be restricted to the set $\widehat{K}$; the resulting function is denoted by $p|_{\widehat{K}}$ and the space of all such restrictions is

$$\mathbb{P}_2(\widehat{K}) := \{p|_{\widehat{K}} \mid p \in \mathbb{P}_2\}\,. \tag{4.23}$$

The space $\mathbb{P}_2(\widehat{K})$ is 10-dimensional, as indicated by the 10 coefficients in the expansion in (4.22). Thus, its bases are composed of 10 linearly independent functions. A natural basis is provided by the Lagrange polynomials which are defined, for all $\mathbf{x} \coloneqq (x, y, z) \in \widehat{K}$, by the following rules [53]:

$$\begin{cases} \widehat{\psi}_1(\mathbf{x}) \coloneqq 2\,(x+y+z)^2 - 3\,(x+y+z) + 1 & \widehat{\psi}_6(\mathbf{x}) \coloneqq 4xy \\ \widehat{\psi}_2(\mathbf{x}) \coloneqq (2x-1)\,x & \widehat{\psi}_7(\mathbf{x}) \coloneqq 4y\,(1-x-y-z) \\ \widehat{\psi}_3(\mathbf{x}) \coloneqq (2y-1)\,y & \widehat{\psi}_8(\mathbf{x}) \coloneqq 4z\,(1-x-y-z) \\ \widehat{\psi}_4(\mathbf{x}) \coloneqq (2z-1)\,z & \widehat{\psi}_9(\mathbf{x}) \coloneqq 4xz \\ \widehat{\psi}_5(\mathbf{x}) \coloneqq 4x\,(1-x-y-z) & \widehat{\psi}_{10}(\mathbf{x}) \coloneqq 4yz \end{cases} \tag{4.24}$$

Each Lagrange polynomial has the value of 1 at one node and 0 at the rest of nodes; more precisely:

$$\widehat{\psi}_i(\mathbf{a}_j) = \delta_{ij} \qquad \forall i, j \in \{1, 2, \ldots, 10\}\,, \tag{4.25}$$

with δ_{ij} being the Kronecker delta. It follows that the coefficients of the expansion of any $p \in \mathbb{P}_2(\widehat{K})$ with respect to the basis (4.24) are the nodal values of p, i.e. it holds:

$$p = \sum_{i=1}^{10} p(\mathbf{a}_i)\widehat{\psi}_i \qquad \forall p \in \mathbb{P}_2(\widehat{K})\,. \tag{4.26}$$

Lagrangian polynomials allow to define for each $K \in \mathcal{T}_h$ a triple of functions:

$$\phi_K^x \coloneqq \sum_{i=j}^{10} x_j^K \widehat{\psi}_j\,, \qquad \phi_K^y \coloneqq \sum_{i=j}^{10} y_j^K \widehat{\psi}_j\,, \qquad \phi_K^z \coloneqq \sum_{i=j}^{10} z_j^K \widehat{\psi}_j\,, \tag{4.27}$$

where x_j^K, y_j^K, z_j^K are the coordinates of the j-th node, $\mathbf{a}_j^K$, of K. The transformation map $\phi_K \colon \widehat{K} \to \mathbb{R}^3$ can then be defined by [46]:

$$\phi_K(\mathbf{x}) \coloneqq (\phi_K^x(\mathbf{x}), \phi_K^y(\mathbf{x}), \phi_K^z(\mathbf{x})) \qquad \forall \mathbf{x} \in \widehat{K}. \tag{4.28}$$

It can be verified that (4.28) maps $\widehat{K}$ to K, i.e. $\phi_K(\widehat{K}) = K$.

Having established a particular transformation map for each $K \in \mathcal{T}_h$, we can define the space of approximation functions on K by [46]:

$$P_K \coloneqq \{f \colon K \to \mathbb{R} \mid f \circ \phi_K \in \mathbb{P}_2(\widehat{K})\}\,. \tag{4.29}$$

Finally, we can specify the FE space $\mathcal{V}_h$ to be the space of all continuous functions $f \colon \overline{\Omega}_h \to \mathbb{R}$ whose restrictions $f|_K$ for all $K \in \mathcal{T}_h$ belong to P_K, i.e. [46]:

$$\mathcal{V}_h \coloneqq \{f \colon \overline{\Omega}_h \to \mathbb{R} \mid f \text{ continuous}, f|_K \in P_K, \forall K \in \mathcal{T}_h\}\,. \tag{4.30}$$

Each space P_K has a natural basis $(\widehat{\psi}_1 \circ \phi_K^{-1}, \ldots, \widehat{\psi}_{10} \circ \phi_K^{-1})$. A natural basis $(\psi_1, \ldots, \psi_{N_h})$ of $\mathcal{V}_h$ is then formed by functions which take the value 1 at exactly one node of the mesh $\mathcal{T}_h$ and whose restrictions $\psi_j|_K$ are either zero, or equal to any one of the basis functions of P_K. In such way, the support[1] of each ψ_j in $\mathbb{R}^3$ will be as small as possible, which means that most elements in the matrix of the final linear system will be zero (i.e. the matrix will be *sparse*). It is not necessary to develop the precise analytical expressions

[1] See footnote on p. 35 for the definition of the *support* of a function.

for the basis functions ψ_j because all integrals will eventually be computed on the reference element $\widehat{K}$ by means of the transformation formula (4.21). For this reason, only the Lagrange polynomials (4.24) are necessary for the implementation of the FE method and the basis functions ψ_j are actually never needed in the process.

Having specified the FE space $\mathcal{V}_h$ and, to a sufficient degree, its basis $(\psi_1, \ldots, \psi_{N_h})$, we can specialize the Galerkin approximation (4.19) for this particular choice of space and basis. It is clear that the general form of expansion of solution $v(t)$ with respect to the basis has not changed by choosing the space and basis; i.e. the expansion has still the form given by (4.18) which is:

$$v(t) = \sum_{j=1}^{N_h} v_j(t)\, \psi_j \,.$$

The only difference is that only now the coefficients $v(t)$ have the special meaning of nodal values. Since the coefficient functions depend only on time and, on the contrary, the basis functions are independent of time, the following expressions can be derived from the general expansion:

$$\dot{v}(t) = \sum_{j=1}^{N_h} \dot{v}_j(t)\, \psi_j \,, \tag{4.31}$$

$$\nabla v(t) = \sum_{j=1}^{N_h} v_j(t) \nabla \psi_j \,. \tag{4.32}$$

Again, both these identities could have already been written in the previous section, but with their coefficients lacking the specific meaning of nodal values implied here.

The stimulus current $J_{\mathrm{stim}}(t)$ in the Galerkin approximation (4.19) can be treated in the same way as $v(t)$. By introducing nodal functions $J_{\mathrm{stim},1}, \ldots, J_{\mathrm{stim},N_r}$, it is possible to approximate it as

$$J_{\mathrm{stim}}(t) \approx \sum_{j=1}^{N_h} J_{\mathrm{stim},j}(t)\, \psi_j \,. \tag{4.33}$$

Regarding the ionic current function, $J_{\mathrm{ion}} \circ v(t)$, there exists an approximate method [50] which eventually allows to express the current in exactly the same form as $J_{\mathrm{stim}}(t)$ in (4.33). The current is evaluated at nodes and interpolated in space by means of the basis $(\psi_1, \ldots, \psi_{N_h})$. Since the basis is Lagrangian, the value of current at j-th node will depend only on the corresponding nodal value $v_j(t)$ and not on any other nodal values, nor on the basis functions. The approximation will then read

$$J_{\mathrm{ion}} \circ v(t) \approx \sum_{j=1}^{N_h} J_{\mathrm{ion}}(v_j(t))\, \psi_j \,, \tag{4.34}$$

where $v_j(t)$ is a real number (the value of v_j at t) and J_{ion} is the artificial ionic function defined by (4.9).

Expressions (4.31)–(4.34) can now be inserted into the Galerkin equation (4.19) which leads to the following semi-discrete finite element problem [52]: Find a family of functions $v_1, \ldots, v_{N_h}$ from $\langle 0, T\rangle$ to $\mathbb{R}$ satisfying $v_j(0) = 0$, such that the mapping $v : \langle 0, T\rangle \to \mathcal{V}_h$

defined by $v(t) \coloneqq \sum_{j=1}^{N_h} v_j(t)\,\psi_j$ satisfies, for all $t \in (0,T)$, the following condition:

$$\sum_{j=1}^{N_h} M_{ij}\dot{v}_j(t) + \sum_{j=1}^{N_h} K_{ij}v_j(t) = -\sum_{j=1}^{N_h} M_{ij}J_{\mathrm{ion}}(v_j(t)) + \sum_{j=1}^{N_h} M_{ij}J_{\mathrm{stim},j}(t) \qquad \forall i \in \{1,\ldots,N_h\}, \quad (4.35)$$

where

$$M_{ij} \coloneqq \int_{\overline{\Omega}_h} \psi_i\,\psi_j \qquad \forall i,j \in \{1,\ldots,N_h\}, \quad (4.36)$$

$$K_{ij} \coloneqq \int_{\overline{\Omega}_h} \nabla\psi_i \cdot (\mathbf{D}\nabla\psi_j) \qquad \forall i,j \in \{1,\ldots,N_h\}. \quad (4.37)$$

Note that Ω has been replaced by $\overline{\Omega}_h$ in (4.36) and (4.37). The problem (4.35) is, just like the general Galerkin approximation (4.19), a system of N_h nonlinear ordinary differential equations for determination of the unknown functions $v_1,\ldots,v_{N_h}$. It can be alternatively expressed in matrix form:

$$\mathbf{M}\,\dot{\mathbf{v}}(t) + \mathbf{K}\,\mathbf{v}(t) = -\mathbf{M}\,\mathbf{J}_{\mathrm{ion}}(\mathbf{v}(t)) + \mathbf{M}\,\mathbf{J}_{\mathrm{stim}}(t)\,, \quad (4.38)$$

where

$$\mathbf{M} \coloneqq [M_{ij}]_{i,j=1}^{N_h}\,, \quad (4.39)$$

$$\mathbf{K} \coloneqq [K_{ij}]_{i,j=1}^{N_h}\,, \quad (4.40)$$

$$\mathbf{v}(t) \coloneqq [v_1(t),\ldots,v_{N_h}(t)]^\top\,, \quad (4.41)$$

$$\dot{\mathbf{v}}(t) \coloneqq [\dot{v}_1(t),\ldots,\dot{v}_{N_h}(t)]^\top\,, \quad (4.42)$$

$$\mathbf{J}_{\mathrm{ion}}(\mathbf{v}(t)) \coloneqq [J_{\mathrm{ion}}(v_1(t)),\ldots,J_{\mathrm{ion}}(v_{N_h}(t))]^\top\,, \quad (4.43)$$

$$\mathbf{J}_{\mathrm{stim}}(t) \coloneqq [J_{\mathrm{stim},1}(t),\ldots,J_{\mathrm{stim},N_h}(t)]^\top\,. \quad (4.44)$$

4.8 Time discretization

The finite element problem (4.38) requires to find in total N_h real-valued functions $v_1,\ldots,v_{N_h}$ defined on $\langle 0,T\rangle$ (one function for each node). By discretizing the time interval, this task will be replaced by that of finding a finite sequence of vectors from $\mathbb{R}^{N_h}$ (one vector of nodal values for each time step).

Suppose that a time step $\Delta t > 0$ is given such that $n \coloneqq T/\Delta t$ is an integer determining the number of solution steps and let $t_0,\ldots,t_n$ be a finite sequence of times defined by: $t_k \coloneqq k\,\Delta t$ for $k \in \{0,\ldots,n\}$. Further, let $\mathbf{J}_{\mathrm{stim},k}$ be a vector of nodal stimuli at time t_k, i.e. $\mathbf{J}_{\mathrm{stim},k} \coloneqq \mathbf{J}_{\mathrm{stim}}(t_k)$ by (4.44), and let $\mathbf{v}_k$ be a numerical estimate of the exact solution $\mathbf{v}(t_k)$, for $k \in \{0,\ldots,n\}$. Note that $\mathbf{v}_0 \coloneqq \mathbf{0}$ by the initial condition. Finally, $\dot{\mathbf{v}}(t_{k+1})$ can be approximated, for each $k \in \{0,\ldots,n-1\}$, by a difference quotient $(\mathbf{v}_{k+1} - \mathbf{v}_k)/\Delta t$. Then, using the backward Euler method [40], one step of solution of (4.38) from time t_k to t_{k+1} can be expressed by:

$$\mathbf{M}\,\frac{\mathbf{v}_{k+1} - \mathbf{v}_k}{\Delta t} + \mathbf{K}\,\mathbf{v}_{k+1} = -\mathbf{M}\,\mathbf{J}_{\mathrm{ion}}(\mathbf{v}_{k+1}) + \mathbf{M}\,\mathbf{J}_{\mathrm{stim},k+1}\,. \quad (4.45)$$

The term $\mathbf{J}_{\text{ion}}(\mathbf{v}_{k+1})$ in the above equation is understood in the sense of (4.43); in general, $\mathbf{J}_{\text{ion}}$ can be considered a mapping from $\mathbb{R}^{N_h}$ to itself defined by:

$$\mathbf{J}_{\text{ion}}(\mathbf{v}) \coloneqq [J_{\text{ion}}(v_1), \ldots, J_{\text{ion}}(v_{N_h})]^\top \qquad \forall \mathbf{v} = [v_1, \ldots, v_{Nh}]^\top \in \mathbb{R}^{N_h}. \tag{4.46}$$

From the computational viewpoint, it is important that this mapping is nonlinear, owing to the nonlinear definition of J_{ion} by (4.9). Consequently, the discretized equation (4.45) must be solved iteratively using the Newton-Raphson procedure, which implies that linearized form of the equation must first be developed.

4.9 Linearization and Newton–Raphson solution

A clear explanation of linearization technique and description of the Newton-Raphson iterative procedure can be found, e.g., in the book by J. Bonet and R.D. Wood *Nonlinear Continuum Mechanics for Finite Element Analysis* (2008) [54]. This section is largely based on that book.

Suppose that a converged solution $\mathbf{v}_k$ at time t_k is known for some $k \in \{0, \ldots, n-1\}$ and it is desired to find an approximate solution $\mathbf{v}_{k+1} \approx \mathbf{v}(t_{k+1})$ at the subsequent time $t_{k+1} = t_k + \Delta t$ by means of Newton–Raphson iterative method. Such procedure requires an initial guess $\mathbf{v}_{k+1}^0$ of the exact solution $\mathbf{v}(t_{k+1})$, for which it is convenient to take the last converged solution $\mathbf{v}_k$, i.e. $\mathbf{v}_{k+1}^0 \coloneqq \mathbf{v}_k$. This initial guess is then refined in an iterative process whose every iteration, generally r-th for $r \geq 1$, consists in a solution of linear system of equations, finally yielding an incremental vector $\mathbf{a}_{k+1}^r$ which additively contributes to the last estimate $\mathbf{v}_{k+1}^{r-1}$ in order to bring it closer to the exact solution $\mathbf{v}(t_{k+1})$. More precisely, the new estimate is $\mathbf{v}_{k+1}^r \coloneqq \mathbf{v}_{k+1}^{r-1} + \mathbf{a}_{k+1}^r$. Every estimate is checked against the convergence criterion (or criteria) and if satisfied, the estimate is accepted as a reasonable approximation of $\mathbf{v}(t_{k+1})$ and as such it is denoted by $\mathbf{v}_{k+1}$.

In order to simplify the notation, in what follows the vectors $\mathbf{v}_k$, $\mathbf{v}_{k+1}^{r-1}$, $\mathbf{a}_{k+1}^r$ and $\mathbf{J}_{\text{stim},k+1}$ will be denoted simply as $\mathbf{u}$, $\mathbf{v}$, $\mathbf{a}$ and $\mathbf{J}_{\text{stim}}$, respectively. Subscripts and superscripts indicating the time step or the iteration number will be similarly omitted from some other symbols introduced in this section.

A common convergence criterion used in FE analyses can be written in the form[1]:

$$\|\mathbf{R}(\mathbf{v})\| < \varepsilon R_{\text{ref}}\,. \tag{4.47}$$

The term on the left-hand side of (4.47) is the Euclidean norm of the residual vector $\mathbf{R}(\mathbf{v})$ which is defined as

$$\mathbf{R}(\mathbf{v}) \coloneqq -\mathbf{M}\,\mathbf{J}_{\text{ion}}(\mathbf{v}) + \mathbf{M}\,\mathbf{J}_{\text{stim}} - \mathbf{M}\,\frac{\mathbf{v}-\mathbf{u}}{\Delta t} - \mathbf{K}\,\mathbf{v}\,. \tag{4.48}$$

The defining term in (4.48) is obtained by moving all terms in eq. (4.45) to the right-hand side. Moving all terms in equation to one side will produce zero on the other side; it follows that the residual vanishes when $\mathbf{v}$ is the exact solution. Thus, if the sequence of estimates converges toward the exact solution, the residual tends to zero.

On the right hand-side of (4.47) there is a product of the tolerance $\varepsilon > 0$ and the reference value R_{ref}. The latter represents the applied loads and it is defined by the right-hand side of (4.45) as:

$$R_{\text{ref}} \coloneqq \|-\mathbf{M}\,\mathbf{J}_{\text{ion}}(\mathbf{v}) + \mathbf{M}\,\mathbf{J}_{\text{stim}}\|\,. \tag{4.49}$$

[1]This is the default convergence criterion used by commercial FE software Ansys [55].

Tolerance ε will be set to 0.005 [55] in the subsequent simulations which means that an estimate $\mathbf{v}$ is accepted as a converged solution if the residual is less than 0.5 % of the reference value.

It remains to specify the linear system which should be solved in every iteration. Using the gradient[1] $\nabla_{\mathbf{v}}\mathbf{R}$ of $\mathbf{R}$ at $\mathbf{v}$, general form of the linearized equation can be written as:

$$\mathbf{R}(\mathbf{v}) + (\nabla_{\mathbf{v}}\mathbf{R})\mathbf{a} = \mathbf{0}\,, \tag{4.50}$$

where $\mathbf{a}$ is the sought increment that, if the solution is convergent, will improve the current estimate $\mathbf{v}$. Equation (4.50) represents a linear approximation of (4.45) near the point $\mathbf{v}$. Since the only nonlinear term in the definition of $\mathbf{R}(\mathbf{v})$ is $\mathbf{J}_{\text{ion}}(\mathbf{v})$, it follows that[2]

$$(\nabla_{\mathbf{v}}\mathbf{R})\mathbf{a} = -\mathbf{M}\,(\nabla_{\mathbf{v}}\mathbf{J}_{\text{ion}})\mathbf{a} - \mathbf{M}\,\frac{\mathbf{a}}{\Delta t} - \mathbf{K}\mathbf{a}\,. \tag{4.51}$$

It is now possible to insert (4.48) and (4.51) into (4.50), but we will first derive an expression for the evaluation of $\nabla_{\mathbf{v}}\mathbf{J}_{\text{ion}}$. Recalling that $\mathbf{J}_{\text{ion}}$ is in fact a mapping from $\mathbb{R}^{N_h}$ to itself defined by (4.46), its gradient can be evaluated if we define a family of functions $J_{\text{ion},i}\colon \mathbb{R}^{N_h} \to \mathbb{R}$, for $i \in \{1, \ldots, N_h\}$, by:

$$J_{\text{ion},i}(\mathbf{v}) \coloneqq J_{\text{ion}}(v_i) \qquad \forall \mathbf{v} = [v_1, \ldots, v_{Nh}]^\top \in \mathbb{R}^{N_h}\,. \tag{4.52}$$

The following statement then follows from definitions (4.46) and (4.52):

$$\mathbf{J}_{\text{ion}}(\mathbf{v}) = [J_{\text{ion},1}(\mathbf{v}), \ldots, J_{\text{ion},N_h}(\mathbf{v})]^\top \qquad \forall \mathbf{v} \in \mathbb{R}^{N_h}. \tag{4.53}$$

In this form, it can be shown that $\mathbf{J}_{\text{ion}}$ satisfies[3]:

$$(\nabla_{\mathbf{v}}\mathbf{J}_{\text{ion}})\mathbf{a} = [(\nabla_{\mathbf{v}}J_{\text{ion},1})\mathbf{a}, \ldots, (\nabla_{\mathbf{v}}J_{\text{ion},N_h})\mathbf{a}]^\top \qquad \forall \mathbf{v}, \mathbf{a} \in \mathbb{R}^{N_h}. \tag{4.54}$$

The terms on the right-hand side can be evaluated as:

$$(\nabla_{\mathbf{v}}J_{\text{ion},i})\mathbf{a} = \sum_{j=1}^{N_h} \frac{\partial J_{\text{ion},i}(\mathbf{v})}{\partial v_j} a_j \qquad \forall i \in \{1, \ldots, N_h\}. \tag{4.55}$$

But it follows from the definitions (4.52) that $J_{\text{ion},i}$ does not depend on v_j unless $i = j$; therefore we have $\dfrac{\partial J_{\text{ion},i}(\mathbf{v})}{\partial v_j} = 0$ if $i \neq j$ and consequently (4.55) simplifies as follows:

$$(\nabla_{\mathbf{v}}J_{\text{ion},i})\mathbf{a} = \frac{\partial J_{\text{ion},i}(\mathbf{v})}{\partial v_i} a_i = \frac{\mathrm{d}J_{\text{ion}}(v_i)}{\mathrm{d}v} a_i \qquad \forall i \in \{1, \ldots, N_h\}. \tag{4.56}$$

The last identity is a consequence of the definitions (4.52). If we now insert (4.56) into (4.54), it can be seen that $\nabla_{\mathbf{v}}\mathbf{J}_{\text{ion}}$ is an $N_h \times N_h$ diagonal matrix

$$\nabla_{\mathbf{v}}\mathbf{J}_{\text{ion}} = \operatorname{diag}\left(\left[\frac{\mathrm{d}J_{\text{ion}}(v_1)}{\mathrm{d}v}, \ldots, \frac{\mathrm{d}J_{\text{ion}}(v_{N_h})}{\mathrm{d}v}\right]\right). \tag{4.57}$$

[1] The notation for gradient used here was adopted from [48].

[2] Equation (4.51) makes use of the linearity of gradient (e.g. [48], p. 221), the chain rule (e.g. [48], p. 220), and the fact that the gradient of a linear mapping at a point is the linear mapping itself ([48], p. 219).

[3] See Proposition 2 on p. 220 in [48].

The derivative of J_{ion} can be expressed from (4.9) as

$$\frac{\mathrm{d}J_{\text{ion}}}{\mathrm{d}v} = \begin{cases} \alpha(2v-1) & \text{for} \quad v \in (0,1) \\ 0 & \text{for} \quad v \in \mathbb{R} \setminus (0,1)\ . \end{cases} \tag{4.58}$$

We can now substitute $\mathbf{R}(\mathbf{v})$ and $\nabla_{\mathbf{v}}\mathbf{R}$ in equation (4.50) by the right-hand sides of (4.48) and (4.51), respectively, and express linearized equation in its final form:

$$\left(\mathbf{M}(\nabla_{\mathbf{v}}\mathbf{J}_{\text{ion}}) + \frac{1}{\Delta t}\mathbf{M} + \mathbf{K}\right)\mathbf{a} = -\mathbf{M}\left(\mathbf{J}_{\text{ion}}(\mathbf{v}) - \mathbf{J}_{\text{stim}} + \frac{\mathbf{v}-\mathbf{u}}{\Delta t}\right) - \mathbf{K}\,\mathbf{v}\,. \tag{4.59}$$

4.10 Implementation

The linear system (4.59) is to be solved in every iteration within each time step. Clearly, in order to perform one such solution, it is necessary to calculate all the matrices and vectors forming the coefficient matrix of the system and the right-hand side vector. Namely, we need $\mathbf{M}$, $\mathbf{K}$, $\nabla_{\mathbf{v}}\mathbf{J}_{\text{ion}}$, $\mathbf{u}$, $\mathbf{v}$, $\mathbf{J}_{\text{ion}}(\mathbf{v})$ and $\mathbf{J}_{\text{stim}}$ before we can solve the system.

Vector $\mathbf{u} = \mathbf{v}_k$ is the converged solution obtained in the previous time t_k, except in the first step when it is zero (by the initial condition). Thus it is always known. The same applies to $\mathbf{v} = \mathbf{v}_{k+1}^{r-1}$ which is the last estimate of solution at time t_{k+1}. Since $\mathbf{v}$ is known, $\mathbf{J}_{\text{ion}}(\mathbf{v})$ and $\nabla_{\mathbf{v}}\mathbf{J}_{\text{ion}}$ can be easily calculated using (4.46) and (4.57), respectively. Nodal stimuli at time t_{k+1}, arranged in $\mathbf{J}_{\text{stim}} = \mathbf{J}_{\text{stim},k+1}$, must be suitably prescribed. Usually the stimulus is applied only within a short period of time at the beginning of simulation and only to those nodes located in the first activated regions. The values of stimuli are determined more or less by trial and error. It should be strong enough (and long enough) to initiate the spread of depolarization, but not too strong because then the potential could immediately exceed the assumed maximum value of 1. Vectors $\mathbf{v}$ and $\mathbf{J}_{\text{ion}}(\mathbf{v})$ as well as matrix $\nabla_{\mathbf{v}}\mathbf{J}_{\text{ion}}$ must be updated in each iteration, while $\mathbf{u}$ and $\mathbf{J}_{\text{stim}}$ do not change within one time step. Matrices $\mathbf{M}$ and $\mathbf{K}$ are independent of time and as such they need to be constructed only once at the beginning of the solution and afterwards they are used in every iteration without any change.

Entries of matrices $\mathbf{M} \coloneqq [M_{ij}]_{i,j=1}^{N_h}$ and $\mathbf{K} \coloneqq [K_{ij}]_{i,j=1}^{N_h}$ were defined by (4.36) and (4.37), respectively. To repeat the definitions:

$$M_{ij} \coloneqq \int_{\overline{\Omega}_h} \psi_i\,\psi_j\,, \qquad K_{ij} \coloneqq \int_{\overline{\Omega}_h} \nabla\psi_i \cdot (\mathbf{D}\nabla\psi_j)\,.$$

However, contrary to what may seem natural at first glance, M_{ij} and K_{ij} are in practice usually not calculated according to the above definitions because such implementation would be inefficient. In the words of Quarteroni [40], "... the need for a high computational efficiency leads to an implementation that is generally not the immediate translation of what has been seen during the theoretical presentation." The difference is that the practical approach is more oriented on individual elements, while the theory defines all integrals in terms of the basis functions ψ_i which are defined on the whole of $\overline{\Omega}_h$. More precisely, what we do in practice is that we take one element after another (in a cycle) and for each of them we calculate all the necessary integrals, but only over the corresponding set K (as if we replaced $\overline{\Omega}_h$ in the above integrals by K). However, since the basis functions are intentionally constructed in such a manner that only a few of them are non-zero on a given K, many integrals vanish and so they do not need to be calculated at all. Thus, we save the computational time by calculating only those few integrals which are non-zero.

Specifically, in the problem solved here, for each element K there will be only 10 basis functions ψ_i satisfying $\psi_i|_K \neq 0$ (i.e. the restriction of ψ_i to K is nonzero). These functions can be identified as those members of the basis which assume the value 1 at one of the ten nodes of K. Moreover, it is not difficult to realize that their non-zero restrictions are the composites $\widehat{\psi}_i \circ \phi_K^{-1}$ for $i \in \{1, 2, \ldots, 10\}$. Thus, the integration eventually needs to be realized with only 10 different functions for each K and we know their analytical expressions. The resulting integrals can be arranged into two 10×10 *local matrices* (or *element matrices*) $\mathbf{M}_K \coloneqq \left[M_{ij}^K\right]_{i,j=1}^{10}$ and $\mathbf{K}_K \coloneqq \left[K_{ij}^K\right]_{i,j=1}^{10}$ defined by

$$M_{ij}^K \coloneqq \int_K (\widehat{\psi}_i \circ \phi_K^{-1})(\widehat{\psi}_j \circ \phi_K^{-1})\,, \tag{4.60}$$

$$K_{ij}^K \coloneqq \int_K \nabla(\widehat{\psi}_i \circ \phi_K^{-1}) \cdot \mathbf{D}_K \nabla(\widehat{\psi}_j \circ \phi_K^{-1})\,. \tag{4.61}$$

The $\mathbf{D}_K$ in the last definition is the diffusion tensor expressed for a particular element K. It is constant within K and it can eventually be written as a 3×3 matrix which will be specified in the next section.

We can now apply the change of variable formula (4.21) and express both integrals in (4.60) and (4.61) on the reference element $\widehat{K}$:

$$\begin{aligned} M_{ij}^K &= \int_K (\widehat{\psi}_i \circ \phi_K^{-1})(\widehat{\psi}_j \circ \phi_K^{-1}) \\ &= \int_{\widehat{K}} |\det(\nabla \phi_K)| ((\widehat{\psi}_i \circ \phi_K^{-1})(\widehat{\psi}_j \circ \phi_K^{-1}) \circ \phi_K) \\ &= \int_{\widehat{K}} |\det(\nabla \phi_K)| (\widehat{\psi}_i \circ \phi_K^{-1} \circ \phi_K)(\widehat{\psi}_j \circ \phi_K^{-1} \circ \phi_K) \\ &= \int_{\widehat{K}} |\det(\nabla \phi_K)| \widehat{\psi}_i \widehat{\psi}_j\,, \end{aligned} \tag{4.62}$$

$$\begin{aligned} K_{ij}^K &= \int_K \nabla(\widehat{\psi}_i \circ \phi_K^{-1}) \cdot \mathbf{D}_K \nabla(\widehat{\psi}_j \circ \phi_K^{-1}) \\ &= \int_{\widehat{K}} |\det(\nabla \phi_K)| \left(\left(\nabla(\widehat{\psi}_i \circ \phi_K^{-1}) \cdot \mathbf{D}_K \nabla(\widehat{\psi}_j \circ \phi_K^{-1}) \right) \circ \phi_K \right) \\ &= \int_{\widehat{K}} |\det(\nabla \phi_K)| \left(\left(\nabla(\widehat{\psi}_i \circ \phi_K^{-1}) \circ \phi_K \right) \cdot \mathbf{D}_K \left(\nabla(\widehat{\psi}_j \circ \phi_K^{-1}) \circ \phi_K \right) \right)\,. \end{aligned} \tag{4.63}$$

The final integral in (4.63) contains gradients that have not been expressed so far. The whole term $\nabla(\widehat{\psi}_j \circ \phi_K^{-1}) \circ \phi_K$, which occurs twice in that integral, can be rephrased if we successively use the chain rule[1], the inverse function theorem[2], and the definition of the transpose of a linear transformation[3]. These operations lead, respectively, to the following identities:

$$\begin{aligned} \nabla(\widehat{\psi}_i \circ \phi_K^{-1}) \circ \phi_K &= (\nabla \widehat{\psi}_i)\, (\nabla(\phi_K^{-1}) \circ \phi_K) \\ &= (\nabla \widehat{\psi}_i)\, (\nabla \phi_K)^{-1} \\ &= (\nabla \phi_K)^{-\top} (\nabla \widehat{\psi}_i)\,. \end{aligned} \tag{4.64}$$

[1] E.g. [48], p. 220.
[2] E.g. [48], p. 245–246.
[3] E.g. [48], p. 71.

Using the definition (4.28) of ϕ_K, the gradients in (4.64) can be expressed as

$$\nabla\phi_K = \begin{bmatrix} \dfrac{\partial\phi_K^x}{\partial x} & \dfrac{\partial\phi_K^x}{\partial y} & \dfrac{\partial\phi_K^x}{\partial z} \\ \dfrac{\partial\phi_K^y}{\partial x} & \dfrac{\partial\phi_K^y}{\partial y} & \dfrac{\partial\phi_K^y}{\partial z} \\ \dfrac{\partial\phi_K^z}{\partial x} & \dfrac{\partial\phi_K^z}{\partial y} & \dfrac{\partial\phi_K^z}{\partial z} \end{bmatrix}, \qquad \nabla\widehat{\psi}_i = \begin{bmatrix} \dfrac{\partial\widehat{\psi}_i}{\partial x} \\ \dfrac{\partial\widehat{\psi}_i}{\partial y} \\ \dfrac{\partial\widehat{\psi}_i}{\partial z} \end{bmatrix}. \tag{4.65}$$

Vectors $\nabla\widehat{\psi}_i$ can be evaluated using definitions (4.24) of the Lagrange polynomials $\widehat{\psi}_i$. Matrix $\nabla\phi_K$ can be evaluated using definitions (4.27) of the transformation functions ϕ_K^x, ϕ_K^y and ϕ_K^z, from which it follows that

$$\nabla\phi_K = \mathbf{A}_K\mathbf{B}\,, \tag{4.66}$$

where

$$\mathbf{A}_K \coloneqq \begin{bmatrix} x_1^K & x_2^K & \cdots & x_{10}^K \\ y_1^K & y_2^K & \cdots & y_{10}^K \\ z_1^K & z_2^K & \cdots & z_{10}^K \end{bmatrix}, \qquad \mathbf{B} \coloneqq \begin{bmatrix} \dfrac{\partial\widehat{\psi}_1}{\partial x} & \dfrac{\partial\widehat{\psi}_1}{\partial y} & \dfrac{\partial\widehat{\psi}_1}{\partial z} \\ \dfrac{\partial\widehat{\psi}_2}{\partial x} & \dfrac{\partial\widehat{\psi}_2}{\partial y} & \dfrac{\partial\widehat{\psi}_2}{\partial z} \\ \vdots & \vdots & \vdots \\ \dfrac{\partial\widehat{\psi}_{10}}{\partial x} & \dfrac{\partial\widehat{\psi}_{10}}{\partial y} & \dfrac{\partial\widehat{\psi}_{10}}{\partial z} \end{bmatrix}. \tag{4.67}$$

Gradient $\nabla\phi_K$ can be conveniently computed using (4.66), but the final expression in (4.64) contains also the transpose of the inverse of $\nabla\phi_K$. Inverse matrix can be calculated from the cofactor matrix, $\operatorname{cof}(\nabla\phi_K)$, which can be obtained by an algorithm described elsewhere (e.g. [56]). Once the cofactor matrix is known, we can calculate [56]

$$(\nabla\phi_K)^{-\top} = \frac{1}{\det(\nabla\phi_K)}\operatorname{cof}(\nabla\phi_K)\,. \tag{4.68}$$

If we now assume that all quantities are given in matrix form, (4.64) can be substituted into (4.63) leading to:

$$\begin{aligned} K_{ij}^K &= \int_{\widehat{K}} |\det(\nabla\phi_K)|\,((\nabla\phi_K)^{-\top}\nabla\widehat{\psi}_i)^\top(\mathbf{D}_K(\nabla\phi_K)^{-\top}\nabla\widehat{\psi}_j) \\ &= \int_{\widehat{K}} |\det(\nabla\phi_K)|\,((\nabla\widehat{\psi}_i)^\top(\nabla\phi_K)^{-1})(\mathbf{D}_K(\nabla\phi_K)^{-\top}\nabla\widehat{\psi}_j) \\ &= \int_{\widehat{K}} |\det(\nabla\phi_K)|\,(\nabla\widehat{\psi}_i)^\top(\nabla\phi_K)^{-1}\mathbf{D}_K(\nabla\phi_K)^{-\top}\nabla\widehat{\psi}_j\,. \end{aligned} \tag{4.69}$$

Additionally, $(\nabla\phi_K)^{-\top}$ in (4.69) can be replaced by (4.68) which gives

$$K_{ij}^K = \int_{\widehat{K}} \frac{1}{|\det(\nabla\phi_K)|}\,(\nabla\widehat{\psi}_i)^\top(\operatorname{cof}(\nabla\phi_K))^\top\mathbf{D}_K\operatorname{cof}(\nabla\phi_K)\nabla\widehat{\psi}_j\,. \tag{4.70}$$

Equations (4.62) and (4.70) contain final analytical expressions for calculation of local matrices $\mathbf{M}_K$ and $\mathbf{K}_K$. However, the functions integrated in these expressions are too

complicated for analytical solution, which means that they must be integrated numerically. The fact that both integrals are expressed on the same set $\widehat{K}$ allows one to use the same *quadrature formula* for both of them. Specifically, in this work the integration will be performed using 4-point Gaussian quadrature rule, which is adequate for tetrahedral elements with quadratic basis functions [53]. The approximate formula yields exact result for polynomials of global degree ≤ 2 and, for a given $f\colon \widehat{K} \to \mathbb{R}$, it reads [53]:

$$\int_{\widehat{K}} f \approx \frac{1}{6} \sum_{i=1}^{4} w_i f(\mathbf{q}_i)\,, \tag{4.71}$$

where $\mathbf{q}_i \in \widehat{K}$ are integration points (or quadrature points, or Gauss points) and $w_i \in \mathbb{R}$ are weights normalized with respect to the volume of $\widehat{K}$ (which is represented by the factor 1/6 in the above formula). The points and weights are specified in Table 2.

Table 2: Integration points and weights for a 4-point Gaussian quadrature rule on the unit tetrahedron $\widehat{K}$ [53].

points $\mathbf{q}_i$	weights w_i
(β, β, β)	0.25
(α, β, β)	0.25
(β, α, β)	0.25
(β, β, α)	0.25
$\alpha = 0.585410196624968$	
$\beta = 0.138196601125010$	

The quadrature formula (4.71) produces the following approximations of the integrals in (4.62) and (4.70):

$$M_{ij}^K \approx \frac{1}{6} \sum_{k=1}^{4} w_k \left|\det(\nabla_{\mathbf{q}_k} \phi_K)\right| \widehat{\psi}_i(\mathbf{q}_k) \widehat{\psi}_j(\mathbf{q}_k)\,, \tag{4.72}$$

$$K_{ij}^K \approx \frac{1}{6} \sum_{k=1}^{4} \frac{w_k}{\left|\det(\nabla_{\mathbf{q}_k} \phi_K)\right|} (\nabla_{\mathbf{q}_k} \widehat{\psi}_i)^\top (\mathrm{cof}(\nabla_{\mathbf{q}_k} \phi_K))^\top \mathbf{D}_K \mathrm{cof}(\nabla_{\mathbf{q}_k} \phi_K) \nabla_{\mathbf{q}_k} \widehat{\psi}_j\,. \tag{4.73}$$

These expressions can be directly used in a computer code to calculate local matrices $\mathbf{M}_K$ and $\mathbf{K}_K$ for each $K \in \mathcal{T}_h$. A typical algorithm moves forward in a cycle over all elements in the mesh and every time a new pair of local matrices is calculated, their entries M_{ij}^K and K_{ij}^K are added to the corresponding places in the global matrices $\mathbf{M}$ and $\mathbf{K}$. Global matrices are initially zero $N_h \times N_h$ matrices which, as the loop proceeds, are incrementally filled. An important part of this *assembly* is a correct identification of rows and columns of global matrices in which the local terms should be added. To give an example of such assignment, let M_{ij}^K be given. This M_{ij}^K is located in the i-th row and j-th column of $\mathbf{M}_K$ and it relates in some way the i-th node of K with its j-th node (possibly the same node when $i = j$). Both nodes have also assigned a unique global number between 1 and N_h. Suppose that the global numbers of the i-th and j-th nodes are, respectively, r and s. Then the term M_{ij}^K should be added to the current value (generally non-zero) in the r-th row of the s-th column of the global matrix $\mathbf{M}$. When this rule is successively applied to all terms of all local matrices, the assembled global matrices are finally obtained.

4.11 Structural vectors and diffusion tensors

Expression (4.73) for approximate calculation of K_{ij}^K contains a matrix of the element-specific diffusion tensor $\mathbf{D}_K$. Using the general definition (4.8) of the diffusion tensor $\mathbf{D}$, the element-specific version of it can be expressed as

$$\mathbf{D}_K = D_{\mathbf{f}_K}\, \mathbf{f}_K \otimes \mathbf{f}_K + D_{\mathbf{s}_K}\, \mathbf{s}_K \otimes \mathbf{s}_K + D_{\mathbf{n}_K}\, \mathbf{n}_K \otimes \mathbf{n}_K\,, \tag{4.74}$$

where $D_{\mathbf{f}_K}$, $D_{\mathbf{s}_K}$, $D_{\mathbf{n}_K}$ are element-specific diffusion coefficients and $\mathbf{f}_K$, $\mathbf{s}_K$, $\mathbf{n}_K$ are element-specific structural vectors. Coefficients as well as vectors are constant within an element. Vectors $\mathbf{f}_K$, $\mathbf{s}_K$, $\mathbf{n}_K$ define the element coordinate system and they must be defined for each element separately in such a manner that the prescribed directions reflect the structure of LV myocardium described in Sec. 2.3. To be more specific, $\mathbf{f}_K$ should lie in the plane tangent to the wall and its direction within the plane should be determined by the helical angle measured from the local circumferential direction. Sheets at end-diastole are approximately tangent to the wall which means that $\mathbf{s}_K$ should also lie in the tangent plane, at a right angle to $\mathbf{f}_K$. Finally, $\mathbf{n}_K$ should be aligned with the local radial (or transversal) direction. These conditions do not define a unique set of vectors; in this work the vectors were defined in such a manner that the triple $(\mathbf{f}_K, \mathbf{s}_K, \mathbf{n}_K)$ always forms a right-hand orthonormal basis, just like the corresponding vectors in Fig. 5B. Once the vectors $\mathbf{f}_K, \mathbf{s}_K, \mathbf{n}_K \in \mathbb{R}^3$ are calculated for a given K, the diffusion matrix corresponding to the tensor (4.74) can be calculated as

$$\mathbf{D}_K = D_{\mathbf{f}_K}\, \mathbf{f}_K(\mathbf{f}_K)^\top + D_{\mathbf{s}_K}\, \mathbf{s}_K(\mathbf{s}_K)^\top + D_{\mathbf{n}_K}\, \mathbf{n}_K(\mathbf{n}_K)^\top, \tag{4.75}$$

provided that the diffusivities are known.

The rest of this section describes the procedure by which the structural vectors were calculated in this work for the tetrahedral mesh $\mathcal{T}_h$ shown earlier in Sec. 4.7. The whole procedure is illustrated in Fig. 14. Determination of the diffusion coefficients will be described in the subsequent sections.

In the first part of the process, the helical angles were calculated for all tetrahedrons in $\mathcal{T}_h$. In order to achieve this goal, fine triangular meshes with element diameters ≤ 1 mm were generated on surfaces Γ_{endo} and Γ_{epi} (red and green meshes in Fig. 14, respectively). Based on these meshes, two sets of points were defined, one for each surface. The first set, S_{endo}, contained all nodes of the endocardial mesh and additionally the centroids of all triangles in the mesh (in order to increase the number of points in the set). The second set, S_{epi}, was constructed by the same procedure, but from the epicardial mesh. Subsequently, for each element $K \in \mathcal{T}_h$ the distance of K from Γ_{endo} was defined as the distance between the centroid $\mathbf{q}_K$ of K and the point in S_{endo} closest to $\mathbf{q}_K$ (yellow point on red mesh in Fig. 14). The resulting value was denoted as δ_{endo}^K. The distance of K from Γ_{epi} was defined in the same way, only the closest point was looked for in S_{epi} and the resulting value was denoted as δ_{epi}^K. Formally, the definitions were:

$$\delta_{\text{endo}}^K \coloneqq \min\{\|\mathbf{x} - \mathbf{q}_K\| \mid \mathbf{x} \in S_{\text{endo}}\}\,, \tag{4.76}$$

$$\delta_{\text{epi}}^K \coloneqq \min\{\|\mathbf{x} - \mathbf{q}_K\| \mid \mathbf{x} \in S_{\text{epi}}\}\,. \tag{4.77}$$

Based on these values it was possible to define an approximate local wall thickness in the place of K:[1]

$$\tau_K \coloneqq \delta_{\text{endo}}^K + \delta_{\text{epi}}^K\,, \tag{4.78}$$

[1] Maximum and minimum calculated thicknesses were 9.20 mm and 3.73 mm.

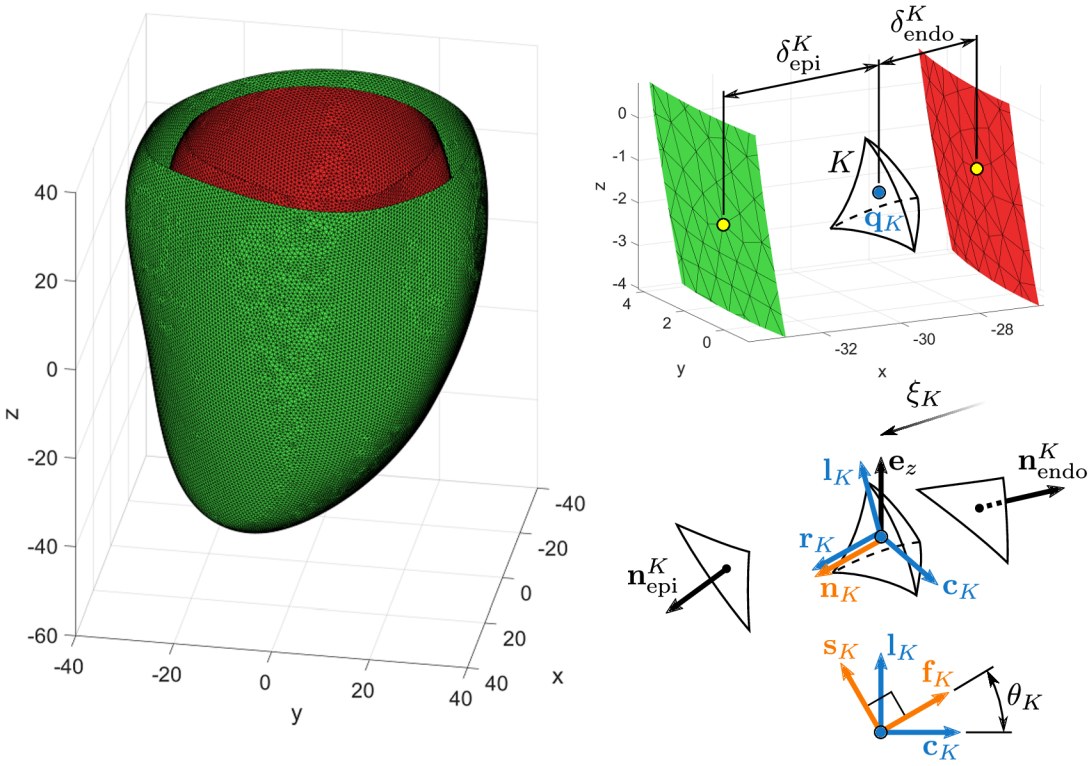

Fig. 14: An illustration of the procedure (described in the text) for obtaining the helical angle θ_K, the geometric directions $\mathbf{c}_K$, $\mathbf{l}_K$, $\mathbf{r}_K$ and the structural vectors $\mathbf{f}_K$, $\mathbf{s}_K$, $\mathbf{n}_K$ for a generic element K with centroid $\mathbf{q}_K$.

and then a normalized distance of $\mathbf{q}_K$ from Γ_{endo}:

$$\xi_K := \frac{\delta^K_{\text{endo}}}{\tau_K} \,. \tag{4.79}$$

Finally, with the assumption that the helical angle changes linearly across the wall from $\theta_{\text{endo}} := 60°$ to $\theta_{\text{epi}} := -60°$ (cf. Sec. 2.3) regardless of the local thickness of the wall, the helical angle θ_K at the centroid $\mathbf{q}_K$ was calculated by linear interpolation as

$$\theta_K := (1 - \xi_K)\, \theta_{\text{endo}} + \xi_K \theta_{\text{epi}} \,. \tag{4.80}$$

Second ingredient necessary for the calculation of vectors $\mathbf{f}_K$, $\mathbf{s}_K$, $\mathbf{n}_K$ is represented by a triple of vectors defining local radial, $\mathbf{r}_K$, circumferential, $\mathbf{c}_K$, and longitudinal, $\mathbf{l}_K$, directions. In order to calculate $\mathbf{r}_K$, the above described procedure of obtaining two closest points from two different sets was repeated, but this time it involved only subsets of S_{endo} and S_{epi} consisting of all centroids of triangles (i.e. the nodes were omitted). In this manner, two closest triangles were found for each K, one on the endocardial and the other on the epicardial surface (see the bottom right corner of Fig. 14). These triangles have each a unique outer unit normal vector which can be readily calculated, for both triangles, as a vector product of two vectors aligned with two different edges of the triangle, divided by its magnitude. Of course, the edges must be suitably chosen so as to produce an *outward* vector. Once the endocardial normal $\mathbf{n}^K_{\text{endo}}$ and the epicardial normal $\mathbf{n}^K_{\text{epi}}$ for a given K are known, the unit radial vector can be defined by

$$\mathbf{r}_K := \frac{(1 - \xi_K)\left(-\mathbf{n}^K_{\text{endo}}\right) + \xi_K \mathbf{n}^K_{\text{epi}}}{\left\|(1 - \xi_K)\left(-\mathbf{n}^K_{\text{endo}}\right) + \xi_K \mathbf{n}^K_{\text{epi}}\right\|} \,, \tag{4.81}$$

provided the denominator is non-zero.[1] Knowing $\mathbf{r}_K$, the circumferential direction can be defined as

$$\mathbf{c}_K \coloneqq \frac{\mathbf{e}_z \times \mathbf{r}_K}{\|\mathbf{e}_z \times \mathbf{r}_K\|}\,, \tag{4.82}$$

where $\mathbf{e}_z \coloneqq [0,0,1]^\top$ is the unit vector along the global z axis which, as already mentioned in Sec. 4.1, coincides with the geometric long axis of our model of LV (our domain Ω). The third geometric vector, $\mathbf{l}_K$, can be defined as the cross product of $\mathbf{r}_K$ and $\mathbf{c}_K$, i.e.:

$$\mathbf{l}_K \coloneqq \mathbf{r}_K \times \mathbf{c}_K\,. \tag{4.83}$$

Knowing the helical angle θ_K and the geometric vectors $\mathbf{c}_K$, $\mathbf{l}_K$, $\mathbf{r}_K$ for each $K \in \mathcal{T}_h$, the structural vectors can be defined as follows:

$$\mathbf{f}_K \coloneqq \cos(\theta_K)\,\mathbf{c}_K + \sin(\theta_K)\,\mathbf{l}_K\,, \tag{4.84}$$

$$\mathbf{s}_K \coloneqq -\sin(\theta_K)\,\mathbf{c}_K + \cos(\theta_K)\,\mathbf{l}_K\,, \tag{4.85}$$

$$\mathbf{n}_K \coloneqq \mathbf{r}_K\,. \tag{4.86}$$

4.12 Fast-conducting layers, early-activated areas and diffusion coefficients

Ventricular conduction system is usually modeled either as a tree of one-dimensional elements coupled to the myocardium (e.g. [57]), or as a thin rapidly conducting endocardial layer (e.g. [58]). In this work, the latter (simpler) approach was adopted.

General anatomy of ventricular conduction system was presented in Sec. 2.4. That section provided also basic description of positions of individual compartments of the system with respect to the ventricular muscle. The description was based mainly on the paper by Stephenson et al. [21] where more detailed information can be found as well as 3-dimensional graphical reconstructions of the conduction system. On the basis of these facts, and taking also into account the locations of the first-activated endocardial areas, as reported by Durrer et al. [25] (see Sec. 2.4), the fast-conducting layers representing left- and right-sided Purkinje network were defined as shown in Fig. 15. The layers in the figure can be regarded as subsets of $\mathcal{T}_h$, therefore the left-sided layer is denoted as $\mathcal{T}_h^L$ and analogously that on the right side of the septum is denoted as $\mathcal{T}_h^R$. In order to obtain $\mathcal{T}_h^L$, a subset of nodes on Γ_{endo} was first selected and afterwards $\mathcal{T}_h^L$ was defined as the set of elements having at least one node in that subset. The second set, $\mathcal{T}_h^R$, was defined in the same way but from a subset of nodes located on low septal part of Γ_{epi}. By assigning a high value of diffusion coefficient to the elements in $\mathcal{T}_h^L$ and $\mathcal{T}_h^R$, it is possible to achieve high conduction velocity in these layers, matching the reported velocities in Purkinje fibres given in Sec. 2.4.

Propagation of potential in the model must be initiated by application of electrical stimulus to appropriately selected nodes. Four sets of nodes were selected for this purpose in such a manner that their locations correspond with the early-activated areas described by Durrer et al. [25] (see Sec. 2.4). These sets are represented by red surfaces in Fig. 15. Only surface nodes (lying on the boundary $\partial\Omega_h$) were included in the sets. The sets will hereinafter be referred to by the symbols defined in Fig. 15, i.e. S_h^{ant} (anterior nodes),

[1] Since $\mathbf{n}_{\text{endo}}^K$ and $\mathbf{n}_{\text{epi}}^K$ are both unit vectors, the denominator is zero if and only if $\mathbf{n}_{\text{endo}}^K = \mathbf{n}_{\text{epi}}^K$ and at the same time $\xi_K = 0.5$. The shape of our boundary $\partial\Omega$ guarantees that the first of these conditions cannot be met.

S_h^{sep} (septal nodes), S_h^{pos} (posterior nodes) and S_h^{R} (nodes on the right side of the septum). In simulations the stimulus will always be prescribed per sets (i.e. the same value to all nodes in a set) and its value will be kept constant during the stimulation period.

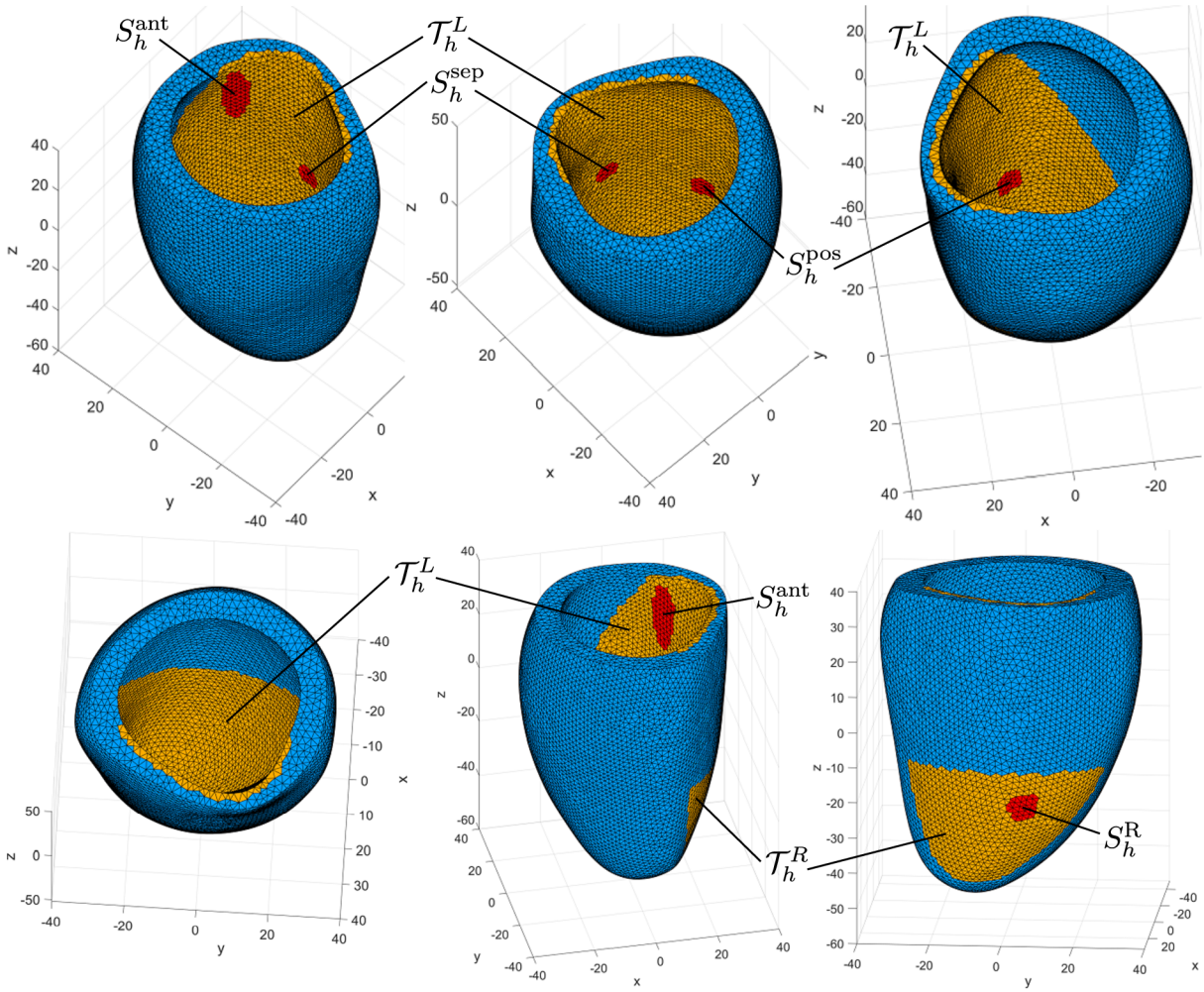

Fig. 15: Fast-conducting layers (orange) and early-activated areas (red) in the model of left ventricle. Fast-conducting layers represent Purkinje fibres originating from the left bundle branch (layer $\mathcal{T}_h^L$) and the right bundle branch (layer $\mathcal{T}_h^R$). Layer $\mathcal{T}_h^L$ covers lower parts of the left ventricular endocardium and the whole left septal surface. Layer $\mathcal{T}_h^R$ covers low right septal surface. Early-activated areas are contained in the layers. Surface nodes inside the areas form sets S_h^{ant}, S_h^{sep}, S_h^{pos} and S_h^{R} on which electrical stimulus can be applied in simulations.

In order to determine suitable values of diffusion coefficients, several trial simulations were performed on meshes with simple geometry and small number of elements. For illustration, one such simulation is shown in Fig. 16. All trial simulations used the same element size $h = 2$ mm, time step $\Delta t = 0.5$ ms and rate parameter $\alpha = 0.1$ ms^{-1} (parameter in the ionic model (4.9)). The same values were used also in the subsequent simulations of activation of left ventricle. The value of stimulus and the duration of its application varied because different geometries, stimulated regions and diffusivities generally required different stimulation conditions. As already mentioned in Sec. (4.3), a particular node was considered activated when its dimensionless potential v (the degree of freedom) reached 0.5. Final chosen values of diffusion coefficients, producing approximately the

experimental velocities reported in Sec. 2.4, are given in Table 3.[1] Nevertheless it should be remembered that true local conduction velocities in FE models depend on many factors, including local or directional variations of element size and even the curvature of the propagating wavefront (cf. Sec. 4.2).

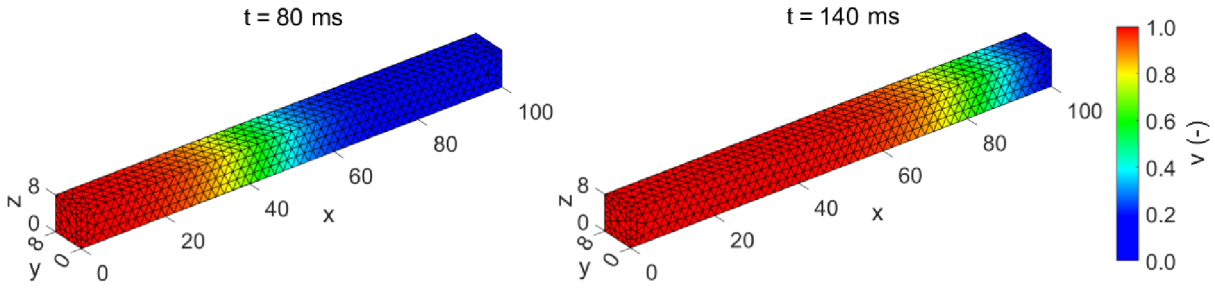

Fig. 16: Simulated propagation of dimensionless potential v along a rectangular block with dimensions $100 \times 8 \times 8$ mm. Initial stimulus was applied to all nodes with coordinate $x = 0$ mm. Simulated conduction velocity corresponds to the velocity in myocardium in the direction of muscle fibres. Time t is measured from the beginning of application of stimulus.

Table 3: Selected (tuned) diffusivities (1st column) and the corresponding approximate conduction velocities (2nd column) for fibre (f), sheet (s) and sheet-normal (n) directions in myocardium and for the fast-conducting layers (fc).

$D_f := 2.5\ \text{mm}^2 \cdot \text{ms}^{-1}$	$v_f \approx 0.67\ \text{mm} \cdot \text{ms}^{-1}$
$D_s := 0.53\ \text{mm}^2 \cdot \text{ms}^{-1}$	$v_s \approx 0.30\ \text{mm} \cdot \text{ms}^{-1}$
$D_n := 0.18\ \text{mm}^2 \cdot \text{ms}^{-1}$	$v_n \approx 0.17\ \text{mm} \cdot \text{ms}^{-1}$
$D_{fc} := 28\ \text{mm}^2 \cdot \text{ms}^{-1}$	$v_{fc} \approx 2.3\ \text{mm} \cdot \text{ms}^{-1}$

4.13 Specification of simulated conditions

It was mentioned in Sec. 2.4 that electrical impulse enters the myocardium by means of the Purkinje-muscle junctions, located under the endocardium. Interestingly, excitation can proceed through the junctions also in the opposite direction, from the muscle cells to the Purkinje fibres [59, 60]. Theoretically, then, if no other conduction abnormality is present besides the LBBB, nothing prevents the impulse, originating in the right ventricle, from traveling across the septum and entering the LV purkinje network, reducing thus partially the delay caused by the block. Some authors [61] describe the general mechanism of spread of excitation in LBBB in precisely this way, which is supported by some experimental [62] as well as computational studies [63] whose results suggest that rapid endocardial conduction is preserved in LBBB. On the other hand, Grant & Dodge [64] analyzed electrocardiographic data from a group of patients with isolated LBBB and concluded that "... in left bundle branch block excitation never regains passage in

[1]Note that the subscripts in D_f, D_s, D_n in Table 3 are light-faced as opposed to the bold-faced $D_{\mathbf{f}}, D_{\mathbf{s}}, D_{\mathbf{n}}$ in the general definition (4.8) of the tensor field $\mathbf{D}$. The goal is to distinguish the former three diffusivities, which are fixed scalars specified in the table, from the latter which are generally scalar fields defined on Ω.

the Purkinje network but spreads from the right ventricle by fiber-to-fiber conduction throughout the left ventricle. This mechanism of spread is of course much slower than when Purkinje fibre pathways are used." Again, there are also computational studies supporting this opposite conclusion [58, 65], their authors claiming that they were unable to reproduce some patient-specific electrophysiological characteristics until the rapid endocardial conduction was disabled in their models. The most likely conclusion resulting from these contradictory findings is that in some patients the rapid conduction is preserved, while in others it is missing; or at least reduced. Perhaps that is the reason why there are considerable differences in reported degrees of prolongation of QRS complex due to the LBBB[1].

In this computational study, two simulations of LV activation must be performed. First will be a control simulation representing normal, healthy conduction, while the second will represent a ventricle with the LBBB. In the context of the discussion in the previous paragraph, it is now necessary to decide whether or not the second simulation should include rapid conduction in layer $\mathcal{T}_h^L$ of the model (see Fig. 15). Since this study aims mainly to determine the possible *extent* of reduction of ejection fraction due to the isolated LBBB, it should be sufficient to investigate only the worst possible case; thus the rapid conduction in LV endocardium will be removed in the simulation of the LBBB, which means that layer $\mathcal{T}_h^L$ will be regarded as a regular muscular tissue with diffusion coefficients D_f, D_s and D_n specified in Table 3. Having made this decision, it is now possible to specify rules for assignment of diffusion coefficients for both simulations. In general, to each element $K \in \mathcal{T}_h$ a triple of diffusion coefficients $(D_{\mathbf{f}_K}, D_{\mathbf{s}_K}, D_{\mathbf{n}_K})$ must be prescribed in each simulation, as indicated by the general expression of the element diffusion matrix $\mathbf{D}_K$ in (4.75). In control simulation, both $\mathcal{T}_h^L$ and $\mathcal{T}_h^R$ will serve as fast-conducting layers and the rest of elements will represent a standard myocardial tissue with orthotropic conductivity. Thus the rule for prescription of coefficients in this simulation can be formulated as follows:

$$(D_{\mathbf{f}_K}, D_{\mathbf{s}_K}, D_{\mathbf{n}_K}) := \begin{cases} (D_{fc}, D_{fc}, D_n) & \text{if} \quad K \in \mathcal{T}_h^L \cup \mathcal{T}_h^R \\ (D_f, D_s, D_n) & \text{if} \quad K \notin \mathcal{T}_h^L \cup \mathcal{T}_h^R \end{cases} . \tag{4.87}$$

In LBBB simulation, rapid conduction will be assumed only in $\mathcal{T}_h^R$ and consequently the diffusivities can be assigned according to:

$$(D_{\mathbf{f}_K}, D_{\mathbf{s}_K}, D_{\mathbf{n}_K}) := \begin{cases} (D_{fc}, D_{fc}, D_n) & \text{if} \quad K \in \mathcal{T}_h^R \\ (D_f, D_s, D_n) & \text{if} \quad K \notin \mathcal{T}_h^R \end{cases} . \tag{4.88}$$

Note that in fast-conducting layers, $D_{\mathbf{n}_K}$ equals to D_n rather than D_{fc}. This is so because $\mathbf{n}_K$ points in a direction transverse to the fast-conducting layers in which rapid propagation cannot be expected.

It now remains to specify the loading conditions which are represented by stimuli applied to the nodes contained in sets S_h^{ant}, S_h^{sep}, S_h^{pos} and S_h^{R}, depicted in Fig. 15. Values of stimuli as well as durations of their application were determined more or less by trial and error. The goal was to achieve synchronous activation of S_h^{ant}, S_h^{sep} and S_h^{pos} in the

[1]Standard electrocardiographic criteria for the diagnosis of complete LBBB include QRS duration exceeding 120 ms [15], but several clinical studies [34, 35, 36] reported mean values in the range 140–150 ms and for example Grant & Dodge [64] observed QRS complex prolonged by more than 80 ms in 20 % of their patients, which means that QRS duration in these patients was higher than 160–170 ms (see normal values in Sec. 2.4).

control simulation and to delay the activation of S_h^{R} by about 10 ms relative to the former three sets (cf. Sec. 2.4). The final values are summarized in Table. 4. Note that all stimuli as well as durations of their application are substantially greater than those used in the single-cell simulations presented earlier in Fig. 12. The reason for this is that the single-cell trials were, in fact, 0-dimensional simulations in which the stimulus supplied only a single point. On the contrary, in 3-dimensional simulations the current spreads from the point of application which means that a greater stimulus is needed for a longer period of time. In the particular case of this study, the stimulation period is especially prolonged because the simulated increase of potential is very slow owing to the low value of the rate parameter α.

Table 4: Values of stimuli, J_{stim}, and time periods of their application, t_{stim}, in the control simulation and in the simulation of LBBB. Stimuli were prescribed separately to nodes in sets S_h^{ant}, S_h^{sep}, S_h^{pos} and S_h^{R} (see Fig. 15).

	S_h^{ant}		S_h^{sep}		S_h^{pos}		S_h^{R}	
	J_{stim} (ms^{-1})	t_{stim} (ms)	J_{stim} (ms^{-1})	t_{stim} (ms)	J_{stim} (ms^{-1})	t_{stim} (ms)	J_{stim} (ms^{-1})	t_{stim} (ms)
Control	1.0	$\langle 0, 50\rangle$	2.0	$\langle 0, 50\rangle$	1.85	$\langle 0, 50\rangle$	1.6	$\langle 10, 60\rangle$
LBBB	0	–	0	–	0	–	1.6	$\langle 0, 50\rangle$

4.14 Results

Both simulations specified in the previous section were realized in software Matlab R2021b in which the FE algorithm presented in this chapter was implemented. All systems of linear equations were solved using Matlab built-in direct solver. Calculated propagation of potential from both simulations is shown in Fig. 17. In the control simulation, nodes in S_h^{ant}, S_h^{sep} and S_h^{pos} were activated 8–8.5 ms after the start of stimulation; nodes in S_h^{R} were activated 10 ms later. Activation of the whole ventricle was complete at $t = 110.5$ ms which means that the total activation time was $110.5\ \mathrm{ms} - 8\ \mathrm{ms} = 102.5$ ms. This time is little longer than an average normal QRS complex but it is still within the range of normal values (cf. Sec. 2.4). The prolongation might be attributed to the fact that activation in the model was initiated in only four small regions, while in real heart Purkinje fibres surely have much more connections with working myocardium. It is also possible that Purkinje network in reality spans larger portion of LV endocardium than assumed in the model; the size of the conducting layer $\mathcal{T}_h^L$ was selected on the basis of the work of Stephenson et al. [21] who themselves recognized that their reconstruction of Purkinje network was not complete, despite high resolution of their imaging device. It should also be remembered that a basal portion of the original model of LV was cut out before generation of mesh (see Sec. 4.1). If the original model was used, the prolongation of depolarization would be even more pronounced. In that case it would probably be appropriate to assume larger conducting layer $\mathcal{T}_h^L$ or to increase the coefficient D_{fc} in order to achieve higher conduction velocity in fast-conducting layers (recall from Sec. 2.4 that conduction velocities as high as $3.50\ \mathrm{mm} \cdot \mathrm{ms}^{-1}$ were measured in Purkinje fibres).

Regarding the second simulation representing the LBBB, nodes in S_h^{R} were activated after 8.5–9 ms and activation of whole ventricle was complete at $t = 162$ ms. Total activation time in this case was thus $162\ \mathrm{ms} - 8.5\ \mathrm{ms} = 153.5$ ms which means that complete depolarization required 51 ms more than in the control case (50% increase).

This prolongation corresponds with prolongations of QRS complex reported in literature (see footnote on p. 53).

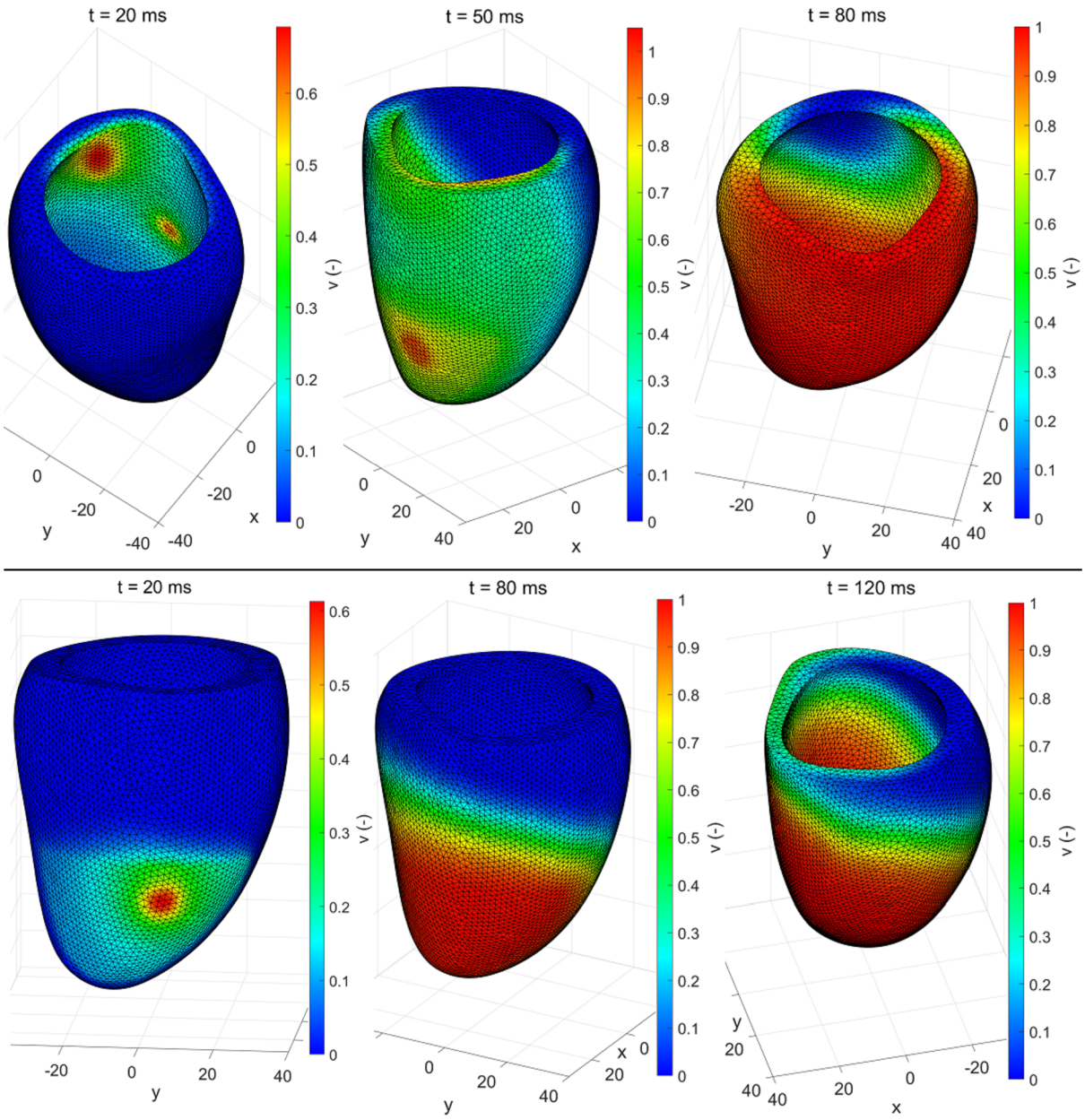

Fig. 17: Propagation of dimensionless potential v in the control simulation (top row) and in the simulation of LBBB (bottom row). Time t is measured from the beginning of application of stimulus in both simulations.

Since the initial latency of 8 ms in control simulation and 8.5 ms in LBBB simulation both have no physiological meaning, these values were finally subtracted from the calculated nodal activation times. Thus, final activation times prepared for further use range from 0 ms to 102.5 ms in healthy conditions and from 0 ms to 153.5 ms in the LBBB case. Activation maps reconstructed from these times are depicted in Fig. 18.

Activation maps should generally be regarded as mathematical functions of the form (4.7). If we denote by t_j^{eac} the time of electrical activation of j-th node under either control or LBBB conditions, then an electrical activation map eac: $\overline{\Omega}_h \to \mathbb{R}$ can be defined, using

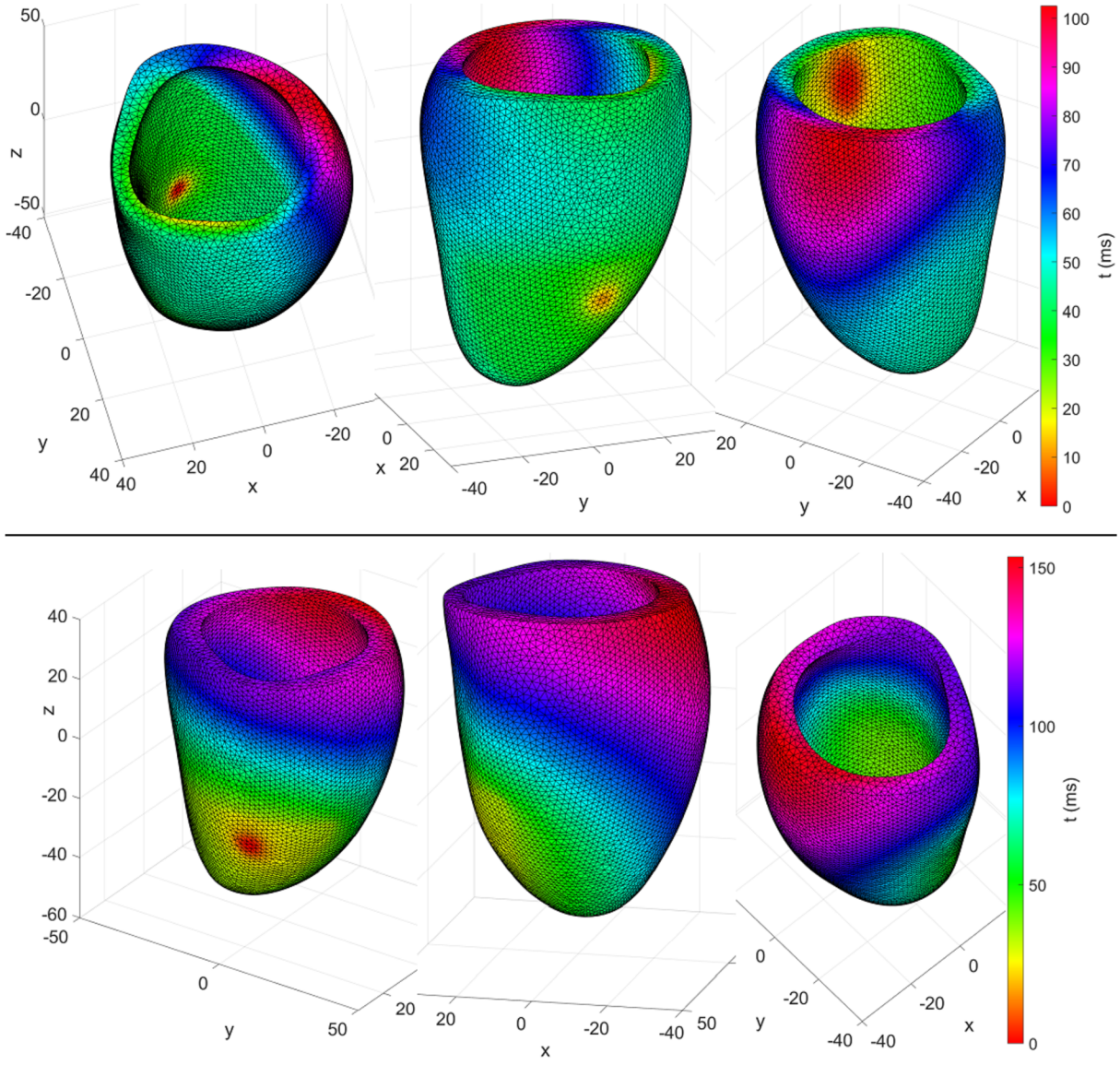

Fig. 18: Activation times measured from the onset of activation in the model; i.e. $t = 0$ ms marks the instant of the first occurrence of $v > 0.5$. Top row: control simulation, bottom row: LBBB simulation.

the Lagrangian basis $(\psi_1, \ldots, \psi_{N_h})$, as:

$$\mathrm{eac} \coloneqq \sum_{j=1}^{N_h} t_j^{\mathrm{eac}} \psi_j \,. \tag{4.89}$$

Maps of this kind could be used to prescribe the distributions of the beginning of contraction in the simulations of ventricular mechanics. However, much simpler maps can be used in this work because in the subsequent simulations the onsets of contraction will always be prescribed per element. Thus it is sufficient to assume activation maps of the form

$$\mathrm{eac} \colon \mathcal{T}_h \to \mathbb{R} \tag{4.90}$$

which assign one activation time to each element in $\mathcal{T}_h$. A natural choice is then to define $\mathrm{eac}(K)$ to be the activation time at the centroid $\mathbf{q}_K$ of an element $K \in \mathcal{T}_h$, which can

be easily calculated by interpolating nodal activation times to the centroid of K. In this manner, two activation maps were calculated in this work from the results depicted in Fig. 18. First of these was calculated from the results of the control simulation and it will hereinafter be denoted as $\mathrm{eac_c}$ (subscript "c" for *control*); the second map was calculated from the results of the simulation with the branch block and it will therefore be denoted as $\mathrm{eac_b}$. These maps are the final outcome of the simulations of electrophysiology presented in this chapter.

5 Simulations of ventricular contraction

In this chapter, the FE model introduced in Chapter 4 will be used to simulate a contraction of normal, healthy ventricle and of ventricle with the left bundle branch block. Electrical activation maps, defined in the end of Chapter 4, will be used to distribute the onset of mechanical activation (beginning of contraction) througout the model. As opposed to the simulations of electrophysiology, which were completely programmed in Matlab, simulations of mechanics will be realized in commercial FE software Ansys[1]. For this reason, the explanation of the theory in this chapter will be less detailed then in the previous chapter. In particular, the individual steps of the FE approximation of the equilibrium equation $\operatorname{div}(\boldsymbol{\sigma}) = \mathbf{0}$, which governs motion of a deforming continuous body [43], will not be discussed at all. The chapter will focus mainly on the constitutive description of passive myocardium, incorporation of initial prestress and modeling of muscle contraction because these are elements that actually have to be programmed in Ansys in order to perform the intended simulations. After that, the methods of modeling of pressure and volume changes during the cardiac cycle will be explained and finally the results will be presented.

5.1 Description of kinematics

The purpose of this section is to introduce some important kinematic quantities that will be needed in the subsequent sections and to establish notation and terminology related to the motion of a continuous body.

It is clear that the shape of the ventricle changes during the cardiac cycle, mainly because of its contraction. From the computational point of view, this means that the domain Ω (or Ω_h), introduced in the previous chapter, will no longer be a fixed domain occupied by the vetricle at all times t. Instead, it will serve as a *reference configuration* [66] which we will assume that the LV occupies at time $t = 0$ ms and with respect to which we will describe the motion of the ventricle. Such description of motion is called the *referential description* [43]. A region which the ventricle occupies at some time $t > 0$ ms is called an *actual* (or *current* or *present*) *configuration* [66] and it will be denoted by Ω_t.[2] Both configurations are sketched in Fig. 19. The mapping

$$\chi_t \colon \Omega \to \Omega_t \tag{5.1}$$

which maps points of the ventricle from their reference places $\mathbf{X} \in \Omega$ into actual places $\mathbf{x} \coloneqq \chi_t(\mathbf{X}) \in \Omega_t$ is called the *transplacement* from the reference configuration to the actual configuration at time t [43]. It is assumed to be at least a C^1-diffeomorphism [43].[3] Consequently, it is possible to take its gradient $\nabla\chi_t$ for which an appropriate name would be the *transplacement gradient* [43, 67] but which is almost invariably called the *deformation gradient* [66, 54], even though it is not necessarily related to any deformation[4]

[1] Ansys Mechanical APDL 2021 R2 exactly.

[2] A reference configuration does not necessarily have to be a region occupied by a given body in the course of its motion [43]. If it coincides with the region occupied by the body at time $t = 0$ ms, as it does in the present study, it is also called an *initial configuration*. The word *configuration* is sometimes replaced by the word *shape* [43].

[3] A C^1-diffeomorphism is a continuously differentiable bijection whose inverse is also continuously differentiable [43]. In situations when C^1 is not sufficient, it must be replaced by C^n with $n > 1$ [67].

[4] A body in a rigid motion does not change its shape; thus it does not "deform" in the ordinary meaning of the word.

[66]. The deformation gradient is denoted by $\mathbf{F}$, i.e.

$$\mathbf{F} \coloneqq \nabla \chi_t \,. \tag{5.2}$$

If there is no special reason to do so, the dependence of $\mathbf{F}$ on time is usually not made explicit in the notation. Also, the symbol $\mathbf{F}$ is commonly used in literature to denote both the tensor field (5.2) as well as its value $(\nabla \chi_t)(\mathbf{X}) = \nabla_{\mathbf{X}}(\chi_t)$ at some $\mathbf{X} \in \Omega$. In this work, the symbol will be used in both meanings. The deformation gradient $\mathbf{F}$ at $\mathbf{X}$ is a linear transformation which can be regarded as the best linear approximation of χ_t in a neighborhood of $\mathbf{X}$ [43].

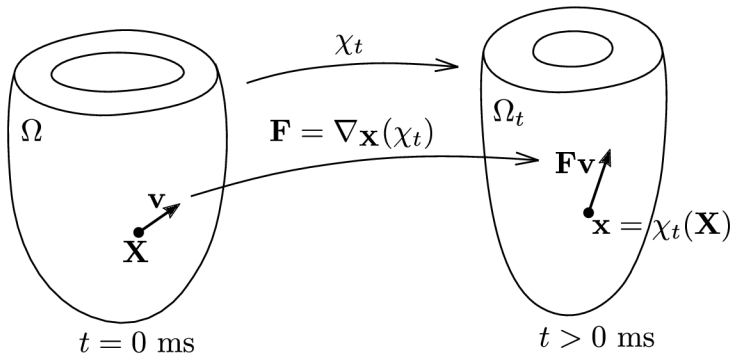

Fig. 19: An illustration of the deformation of the ventricle from the initial (reference) configuration Ω into the current configuration Ω_t. The transplacement χ_t maps places occupied by points of the ventricle at time $t = 0$ ms into places occupied by the same points at time $t > 0$ ms. The deformation gradient $\mathbf{F}$ at $\mathbf{X}$ transforms vectors in the reference configuration into vectors in the current configuration.

Since χ_t is a diffeomorphism, the determinant of $\mathbf{F}$ is non-zero at all $\mathbf{X} \in \Omega$. Although the general mathematical theory does not exclude the possibility that $\det(\mathbf{F}) < 0$, in practical applications it is common to assume that all transplacements are such that $\det(\mathbf{F}) > 0$ [43]. We can then define a positive Jacobian

$$J \coloneqq \det(\mathbf{F}) > 0 \tag{5.3}$$

whose physical meaning is the volume ratio of an infinitesimal volume near $\mathbf{x} = \chi_t(\mathbf{X})$ (i.e. in the actual configuration) to an infinitesimal volume near $\mathbf{X}$ (i.e. in the reference configuration) [66].

The deformation gradient $\mathbf{F}$ is invertible and the inverse function theorem[1] asserts that

$$\nabla_{\chi_t(\mathbf{X})}(\chi_t^{-1}) = (\nabla_{\mathbf{X}}(\chi_t))^{-1} = \mathbf{F}^{-1} \qquad \forall \mathbf{X} \in \Omega \,. \tag{5.4}$$

Invertibility also implies, by means of the polar decomposition theorem[2], that there exists a unique multiplicative decomposition

$$\mathbf{F} = \mathbf{RU} \tag{5.5}$$

in which $\mathbf{R}$ is the *rotation tensor* and $\mathbf{U}$ is the *right stretch tensor* [43]. The rotation tensor is a proper orthogonal tensor which means that $\mathbf{R}^{-1} = \mathbf{R}^\top$ and $\det(\mathbf{R}) = 1$. The

[1] E.g. [48], p. 245–246.
[2] E.g. [48], p. 322.

right stretch tensor is a symmetric, positive definite tensor which means that $\mathbf{U} = \mathbf{U}^\top$ and $\mathbf{v} \cdot \mathbf{U}\mathbf{v} > 0$ for every non-zero vector $\mathbf{v}$. The fact that $\det(\mathbf{R}) = 1$ implies that

$$\det(\mathbf{U}) = \det(\mathbf{F}) = J. \tag{5.6}$$

The deformation gradient $\mathbf{F}$ is a linear transformation which maps vectors in the reference configuration into deformed vectors in the current configuration. Thus a vector $\mathbf{v}$ in the reference configuration will appear as $\mathbf{F}\mathbf{v}$ in the current configuration (see Fig. 19). Since both $\mathbf{R}$ and $\mathbf{U}$ are linear transformations as well, the polar decomposition (5.5) suggests that the action of $\mathbf{F}$ on $\mathbf{v}$ can be effected by applying first a *pure stretch*, expressed by $\mathbf{U}$, and then a *pure rotation*, expressed by $\mathbf{R}$ [43]; more precisely:

$$\mathbf{F}\mathbf{v} = (\mathbf{R}\mathbf{U})\mathbf{v} = \mathbf{R}(\mathbf{U}\mathbf{v})\,. \tag{5.7}$$

An illustrative example of this two-step transformation process in a 2-dimensional space is shown in Fig. 20.

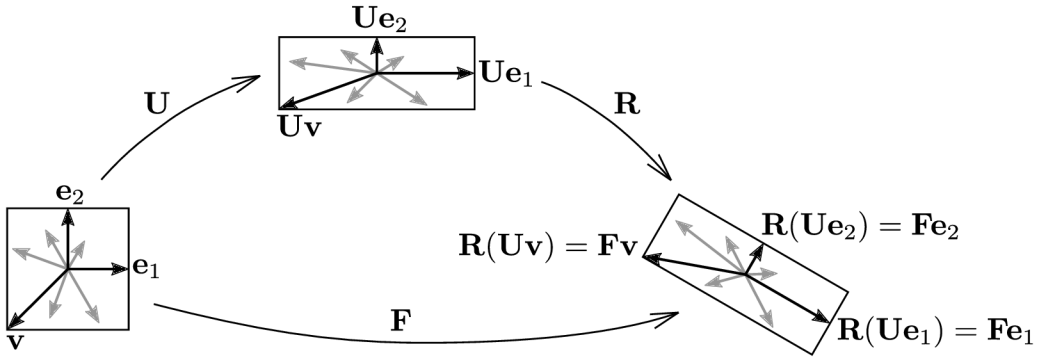

Fig. 20: An example showing how $\mathbf{F}$, $\mathbf{U}$ and $\mathbf{R}$ act on vectors in a 2-dimensional space (inspired by Figure 1 on p. 324 in [48]). Consider all vectors emanating from the centroid of the square on the left which are contained inside the square. Such vectors are, for example, $\mathbf{e}_1$, $\mathbf{e}_2$ and $\mathbf{v}$ (some other vectors are shown in gray). Suppose that $\mathbf{F}$ is a deformation gradient which transforms the vectors inside the square into the rotated rectangle shown on the right. In particular, $\mathbf{e}_1$, $\mathbf{e}_2$ and $\mathbf{v}$ are mapped into $\mathbf{F}\mathbf{e}_1$, $\mathbf{F}\mathbf{e}_2$ and $\mathbf{F}\mathbf{v}$, respectively. Suppose that $\mathbf{F} = \mathbf{R}\mathbf{U}$ is the polar decomposition of $\mathbf{F}$ and that $\mathbf{e}_1$ and $\mathbf{e}_2$ are principal vectors (eigenvectors) of $\mathbf{U}$ forming an orthonormal basis. Then the transformation of vectors can be realized by first stretching the square in the principal directions by means of $\mathbf{U}$ (producing $\mathbf{U}\mathbf{e}_1$, $\mathbf{U}\mathbf{e}_2$ and $\mathbf{U}\mathbf{v}$), and then rotating the intermediate rectangle by means of $\mathbf{R}$ (producing $\mathbf{R}(\mathbf{U}\mathbf{e}_1) = \mathbf{F}\mathbf{e}_1$, $\mathbf{R}(\mathbf{U}\mathbf{e}_2) = \mathbf{F}\mathbf{e}_2$, and $\mathbf{R}(\mathbf{U}\mathbf{v}) = \mathbf{F}\mathbf{v}$).

Constitutive equations are often expressed in terms of the *right Cauchy-Green tensor*

$$\mathbf{C} \coloneqq \mathbf{F}^\top\mathbf{F} = (\mathbf{R}\mathbf{U})^\top\mathbf{R}\mathbf{U} = \mathbf{U}^\top\mathbf{R}^\top\mathbf{R}\mathbf{U} = \mathbf{U}\mathbf{U} = \mathbf{U}^2 \tag{5.8}$$

or the *left Cauchy-Green tensor*

$$\mathbf{B} \coloneqq \mathbf{F}\mathbf{F}^\top = \mathbf{R}\mathbf{U}(\mathbf{R}\mathbf{U})^\top = \mathbf{R}\mathbf{U}\mathbf{U}^\top\mathbf{R}^\top = \mathbf{R}\mathbf{C}\mathbf{R}^\top. \tag{5.9}$$

Both these tensors are symmetric and positive definite. It follows from the definitions (5.8) and (5.9) that

$$\det(\mathbf{C}) = \det(\mathbf{B}) = (\det(\mathbf{F}))^2 = J^2\,. \tag{5.10}$$

Later, we will also need the isochoric version of $\mathbf{B}$ which is defined as

$$\bar{\mathbf{B}} = J^{-2/3}\,\mathbf{B}\,. \tag{5.11}$$

5.2 Passive mechanical properties of myocardium

Sec. 2.3 presented essential information about the microstructure of LV myocardium. It was stated there that locally one can distinguish the predominant fibre direction, **f**, the sheet direction, **s**, and the sheet-normal direction, **n**. In Sec. 2.4, an evidence was given that electrical conduction velocity of myocardium is orthotropic, with principal directions coinciding with the structural directions **f**, **s**, **n**. It is by no means surprising that the same conclusion applies also for the mechanical properties of myocardium which will now be discussed in more detail.

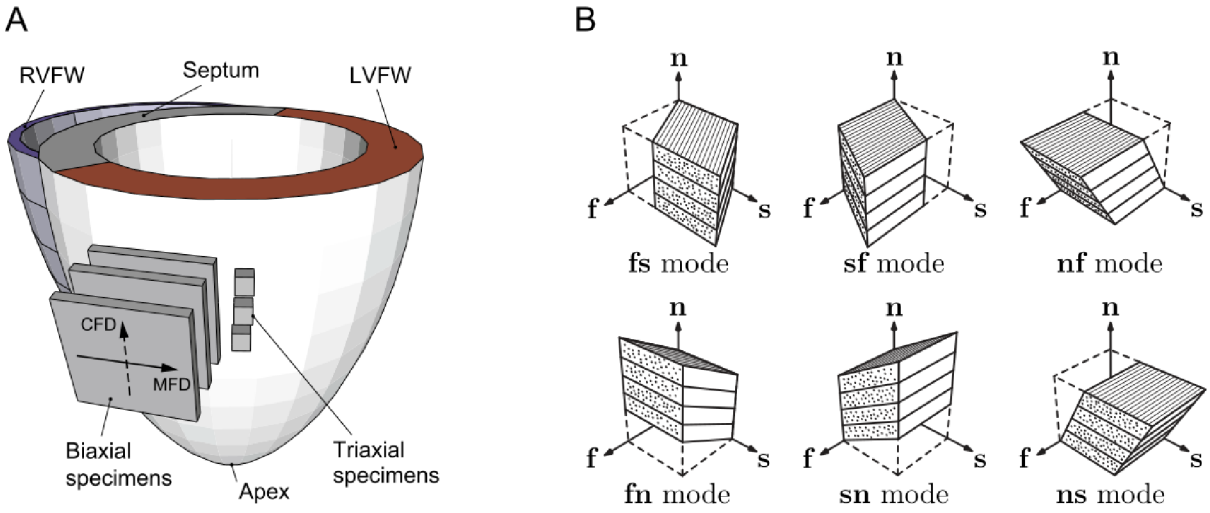

Fig. 21: (A) Schematic representation of ventricles showing typical locations from which squared biaxial specimens and cubic triaxial shear specimens were excised in the experimental study by Sommer et al. [12]. MFD: mean-fibre direction, CFD: cross-fibre direction, LVFW: left ventricular free wall, RVFR: right ventricular free wall. (B) Six possible simple shear modes for cubic myocardial specimens. The modes are denoted by specifying two vectors; the first is the normal vector to the face that is shifted by the simple shear and the second denotes the direction in which the face is shifted. Thus, e.g., the **fs** mode means simple shear in which the face with normal vector **f** is shifted in the direction **s**. Figure was adopted from [12] and modified.

Passive mechanical properties of myocardium (stress-strain relations) are most often determined by quasi-static biaxial extension tests [68, 12] or simple shear tests [39, 12]. Biaxial tests are typically performed with thin squared specimens excised parallel to the ventricular wall, as shown in Fig. 21A. Two parallel edges of the specimens are always aligned with the mean-fibre direction, while the other two correspond to a cross-fibre direction. Interpretation of the cross-fibre direction of the specimens is somewhat questionable because it probably coincides neither with **s**, nor with **n** direction. However, for the computational purposes, the relation between the cross-fibre direction and the structural (principal) directions must be specified in some way, because otherwise orthotropic constitutive equations could not be fitted to the biaxial data. Since the sheets an end-diastole are approximately tangent to the wall (cf. Sec. 2.3), it is probably best to assume that the cross-fibre direction coincides with the **s** direction. This assumption will be adopted in this work. However, whatever be the assumption, it is obvious that biaxial tests alone are not sufficient for a complete characterization of the passive properties of myocardium because they do not capture the response in the direction perpendicular to the plane of the specimen (i.e. transverse to the wall) [14]. In order to capture the

response in three independent directions, biaxial tests must be complemented by triaxial simple shear tests [12]. These are performed on small cubic specimens with edges aligned with the local **f**, **s**, **n** directions. Fig. 21B shows six possible shear modes in which the cubic specimens can be deformed.

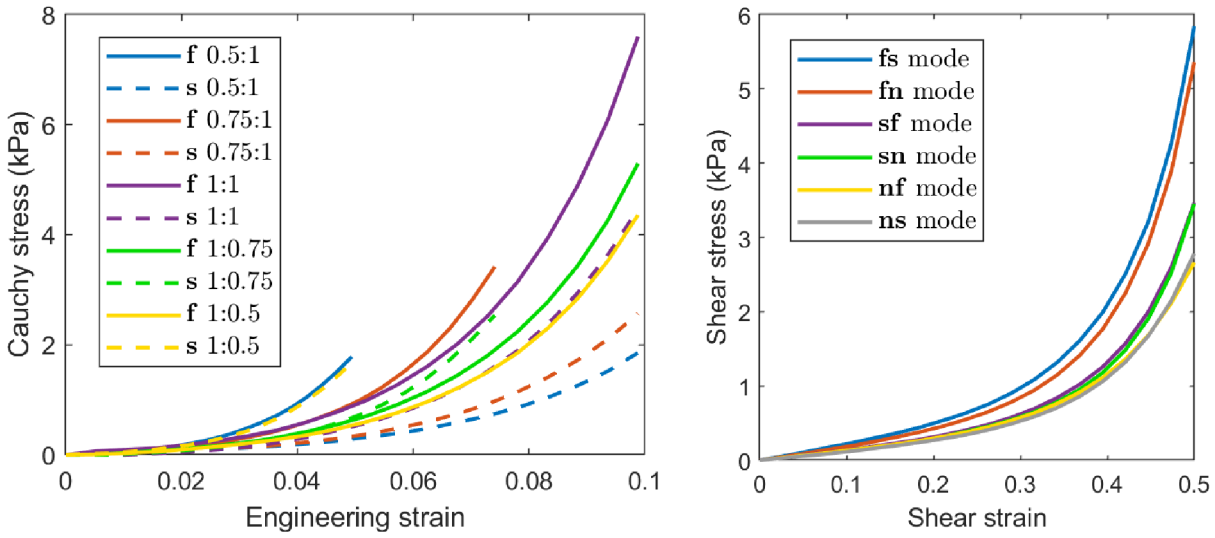

Fig. 22: Average responses of human ventricular myocardium to biaxial (left) and simple shear (right) loading, extracted from [12]. Biaxial specimens were loaded in mean-fibre direction, **f**, and the cross-fibre direction. The latter is here assumed to coincide with the sheet direction, **s**. Five biaxial protocols were used with strain ratios between **f** and **s** directions specified in the legend. Each biaxial curve is an average of the results from 26 specimens and each simple shear curve is an average of the results from 18 specimens.

Currently, the only study which provides results from both biaxial and simple shear tests of human ventricular myocardium is that by Sommer et al. (2015) [12]. The shear protocol of the study included all six possible simple shear modes and the biaxial testing protocol included five different strain ratios between the mean-fibre direction and the cross-fibre direction, namely: $0.5:1$, $0.75:1$, $1:1$ (equibiaxial loading), $1:0.75$, $1:0.5$. Since the responses to both types of tests exhibited hysteresis, the authors calculated for each test the average between the loading and the unloading curves, claiming that this represents an *elastic* response of the tissue. These "elastic" responses were further averaged for all tested specimens and the resulting average responses were presented in Figs. 9 and 13 in the original paper [12]. For the purpose of this thesis, the data were extracted from those figures in order to determine material parameters of the constitutive model that will be presented in Sec. 5.4. The extracted data are re-plotted in Fig. 22. Note that in that figure, the mean-fibre direction is denoted by **f** and the cross-fibre direction is denoted by **s** in accordance with the assumption made above. From the simple shear results, it can be seen that myocardium exhibits highest resistance to shear when it is deformed in **fs** and **fn** modes, intermediate resistance when deformed in **sf** and **sn** modes, and lowest resistance when deformed in **nf** and **ns** modes. In other words the stiffness in simple shear is highest when the face with normal vector **f** is displaced (because such deformation causes extension of muscle fibres), intermediate when the face with normal

s is displaced, and lowest when the face with normal **n** is displaced.[1] Thus the passive mechanical behavior of human myocardium is clearly orthotropic and, as demonstrated by the curves in Fig. 22, highly nonlinear.[2]

5.3 A brief introduction to hyperelastic models for myocardium

Passive mechanical behavior of myocardium is usually mathematically described within the framework of hyperelasticity [14, 69, 70] which means that scalar-valued *strain-energy function*, or *stored-energy function*, Ψ is formulated and all necessary stress tensors are subsequently obtained by taking the gradient of Ψ with respect to a particular deformation tensor in terms of which the function is formulated [66] (see Sec. 5.5). Although there are strain-energy functions for myocardium defined in terms of components of deformation tensors [70], it is more common nowadays to use models expressed in terms of scalar invariants which are independent of coordinates [14, 69]. Since the myocardium is anisotropic, the models use not only isotropic invariants of a particular deformation tensor but also *mixed invariants* [71] formulated in terms of the *structural tensors* $\mathbf{f}\otimes\mathbf{f}$, $\mathbf{s}\otimes\mathbf{s}$ or $\mathbf{n}\otimes\mathbf{n}$ [14].[3] A widely used model for myocardium proposed by Holzapfel and Ogden [14] employs, in addition, a coupling invariant defined by means of the structural tensor $\mathbf{f}\otimes\mathbf{s}$ which couples two preferred material directions. In general, by choosing a suitable set of physically relevant invariants, it is possible to formulate models which incorporate some characteristic histological properties of the tissue [72]. Such models are then referred to as *structurally based* or *structurally motivated* [14].

Similarly to other types of soft tissues, like e.g. arteries [73], the myocardium is commonly treated, in the framework of hyperelasticity, as a fibre-reinforced composite consisting of isotropic matrix and one or more families of fibres [14]. In such approach, each considered constituent of the tissue is usually represented by a separate term, dependent on a suitable invariant, and the strain-energy function of the entire composite is then obtained as the sum of the individual terms. In the above mentioned model by Holzapfel and Ogden [14], the isotropic non-collagenous and non-muscular matrix (which includes fluids and elastin) is represented by an exponential term

$$\Psi_{\text{iso}} \coloneqq \frac{a}{2b}(\exp(b(I_1-3))-1) \tag{5.12}$$

which is dependent on the isotropic invariant

$$I_1 \coloneqq \operatorname{tr}(\mathbf{C})\,. \tag{5.13}$$

Exponential stiffening in the fiber direction, which the authors attribute not only to the extension of muscle fibres but also to the resistance of collagen network, is represented by a term

$$\Psi_{\mathbf{f}} \coloneqq \frac{a_{\mathbf{f}}}{2b_{\mathbf{f}}}(\exp(b_{\mathbf{f}}(I_{4\mathbf{f}}-1)^2)-1) \tag{5.14}$$

[1] More pronounced differences between the individual simple shear modes than that shown in Fig. 22 were reported by Dokos et al. (2003) [39], but they tested samples from pig ventricles rather than human. In particular, they observed significant distinctions not only between **fs** and **fn** modes but also between **sf** and **sn** modes, which almost coincide in Fig. 22. These results of Dokos et al. motivated Holzapfel and Ogden to include in their famous hyperelastic model of human myocardium from 2009 [14] a term with a coupling invariant $I_{8\mathbf{fs}} \coloneqq \operatorname{tr}(\mathbf{C}(\mathbf{f}\otimes\mathbf{s}))$ ($\mathbf{C}$ being the right Cauchy-Green tensor) which allows to distinguish mode **fs** from **fn** and mode **sf** from **sn**.

[2] Besides this the myocardium also exhibits viscoelastic behavior (hysteresis formation) and irreversible stress softening (Mullins effect) [12], but these effects will not be taken into account in this work.

[3] These tensors were already introduced in the definition (4.8) of the diffusion tensor $\mathbf{D}$.

in which

$$I_{4\mathbf{f}} \coloneqq \operatorname{tr}(\mathbf{C}(\mathbf{f}\otimes\mathbf{f}))\,. \tag{5.15}$$

The geometrical meaning of this invariant becomes obvious if we use (5.8) and rewrite the above definition as

$$\begin{aligned} I_{4\mathbf{f}} &= \operatorname{tr}(\mathbf{C}(\mathbf{f}\otimes\mathbf{f})) = \operatorname{tr}(\mathbf{F}^\top\mathbf{F}(\mathbf{f}\otimes\mathbf{f})) = \operatorname{tr}(\mathbf{F}(\mathbf{f}\otimes\mathbf{f})\mathbf{F}^\top) = \operatorname{tr}((\mathbf{F}\mathbf{f})\otimes(\mathbf{F}\mathbf{f})) \\ &= (\mathbf{F}\mathbf{f})\cdot(\mathbf{F}\mathbf{f}) = \|\mathbf{F}\mathbf{f}\|^2\,. \end{aligned} \tag{5.16}$$

$\mathbf{F}\mathbf{f}$ is the deformed unit vector $\mathbf{f}$ (see Fig. 19). Its magnitude $\|\mathbf{F}\mathbf{f}\|$ corresponds to the stretch of a material fiber initially aligned with $\mathbf{f}$. It follows from (5.16) that $I_{4\mathbf{f}}$ is the square of stretch in the fibre direction. The same form of function as in (5.14) is used also to model the exponential response in the sheet direction which is assumed to result from the stretching of collagen fibres laterally binding the the muscle fibres [14]:

$$\Psi_{\mathbf{s}} \coloneqq \frac{a_{\mathbf{s}}}{2b_{\mathbf{s}}}(\exp(b_{\mathbf{s}}(I_{4\mathbf{s}}-1)^2)-1)\,. \tag{5.17}$$

The definition of invariant $I_{4\mathbf{s}}$ is analogous to (5.15):

$$I_{4\mathbf{s}} \coloneqq \operatorname{tr}(\mathbf{C}(\mathbf{s}\otimes\mathbf{s}))\,. \tag{5.18}$$

Lastly, the model contains a coupling term associated with directions $\mathbf{f}$ and $\mathbf{s}$:

$$\Psi_{\mathbf{fs}} \coloneqq \frac{a_{\mathbf{fs}}}{2b_{\mathbf{fs}}}(\exp(b_{\mathbf{fs}}(I_{8\mathbf{fs}})^2)-1)\,. \tag{5.19}$$

As mentioned in the footnote on p. 64, the coupling invariant $I_{8\mathbf{fs}}$ is defined by

$$I_{8\mathbf{fs}} \coloneqq \operatorname{tr}(\mathbf{C}(\mathbf{f}\otimes\mathbf{s}))\,. \tag{5.20}$$

It captures the change of the right angle between $\mathbf{f}$ and $\mathbf{s}$, as can be seen from the following result:

$$\begin{aligned} I_{8\mathbf{fs}} &= \operatorname{tr}(\mathbf{C}(\mathbf{f}\otimes\mathbf{s})) = \operatorname{tr}(\mathbf{F}^\top\mathbf{F}(\mathbf{f}\otimes\mathbf{s})) = \operatorname{tr}(\mathbf{F}(\mathbf{f}\otimes\mathbf{s})\mathbf{F}^\top) = \operatorname{tr}((\mathbf{F}\mathbf{f})\otimes(\mathbf{F}\mathbf{s})) \\ &= (\mathbf{F}\mathbf{f})\cdot(\mathbf{F}\mathbf{s})\,. \end{aligned} \tag{5.21}$$

If the deformed vectors $\mathbf{F}\mathbf{f}$ and $\mathbf{F}\mathbf{s}$ remain orthogonal, as is the case for the shear modes **fn**, **sn**, **nf** and **ns**, then $I_{8\mathbf{fs}}$ vanishes and the term $\Psi_{\mathbf{fs}}$ will generate no stress. On the contrary, if the angle between $\mathbf{f}$ and $\mathbf{s}$ is changed after deformation, which occurs in shear modes **fs** and **sf**, then additional stresses are generated by $\Psi_{\mathbf{fs}}$. Consequently, the shear stress in **fs** and **sf** modes will be higher than that in the corresponding modes **fn** and **sn**, respectively.

The full form of the strain-energy function proposed by Holzapfel and Ogden [14] reads:[1]

$$\begin{aligned} \Psi_{\mathrm{HO}} &\coloneqq \Psi_{\mathrm{iso}} + \Psi_{\mathbf{f}} + \Psi_{\mathbf{s}} + \Psi_{\mathbf{fs}} \\ &= \frac{a}{2b}(\exp(b(I_1-3))-1) + \sum_{i=\mathbf{f},\mathbf{s}} \frac{a_i}{2b_i}(\exp(b_i(I_{4i}-1)^2)-1) + \frac{a_{\mathbf{fs}}}{2b_{\mathbf{fs}}}(\exp(b_{\mathbf{fs}}(I_{8\mathbf{fs}})^2)-1)\,. \end{aligned} \tag{5.22}$$

[1] It should be noted that Holzapfel and Ogden in their paper [14] introduced their model with a mistake in the first term (their equation (5.38)). There, the term was written as $\frac{a}{2b}\exp(b(I_1-3))$. The correct form they gave a few pages later in equation (6.3).

It is important to note that the terms $\Psi_{\mathbf{f}}$ and $\Psi_{\mathbf{s}}$ are included in the model only if $I_{4\mathbf{f}} > 1$ and $I_{4\mathbf{s}} > 1$, respectively, because fibres are assumed to generate no stress under compression [14]. Of course, $a,\ b,\ a_{\mathbf{f}},\ b_{\mathbf{f}},\ a_{\mathbf{s}},\ b_{\mathbf{s}},\ a_{\mathbf{fs}},\ b_{\mathbf{fs}}$ in (5.22) are material parameters which must be determined by fitting the model to experimental data.

In some more recent papers [74, 75, 76], the Holzapfel-Ogden model was used in an alternative nearly incompressible form in which the standard invariants, used in (5.22), are replaced by modified isochoric invariants and additional volumetric term is included in the strain-energy function in order to enforce approximately incompressible behavior. However, some authors [77, 78] pointed out that isochoric versions of anisotropic invariants produce unexpected and unphysical results and they suggested that full anisotropic invariants should be used in nearly incompressible hyperelastic models in order to obtain correct results. Thus, it is now common to formulate strain-energy functions for soft tissues with isotropic part described by the isochoric invariant

$$\bar{I}_1 := J^{-\frac{2}{3}} I_1 \tag{5.23}$$

and anisotropic part described in terms of standard (full) invariants (e.g. [77, 79]).

5.4 An alternative hyperelastic model for human myocardium

In this work an alternative hyperelastic model will be used which is largely based on the nearly incompressible form of the Holzapfel-Ogden model, discussed in the previous section, but which treats differently the contribution of sheets inside the myocardium. The Holzapfel-Ogden model describes myocardium as an isotropic matrix reinforced by muscle fibres and collagen fibres (mutually coupled by the invariant $I_{8\mathbf{fs}}$). In this work, the myocardium will also be treated as a reinforced composite but the constituents which will be taken into consideration are: an isotropic matrix, planar sheets (with isotropic in-plane response) and a family of parallel muscle fibres reinforcing the sheets. The constitutive description of the matrix and the muscle fibres will be the same as in the (nearly incompressible) Holzapfel-Ogden model; i.e. the strain-energy function will include terms

$$\Psi_{\text{iso}} := \frac{a}{2b}(\exp(b(\bar{I}_1 - 3)) - 1) \tag{5.24}$$

and

$$\Psi_{\mathbf{f}} := \frac{a_{\mathbf{f}}}{2b_{\mathbf{f}}}(\exp(b_{\mathbf{f}}(I_4 - 1)^2) - 1) \tag{5.25}$$

which depend on invariants $\bar{I}_1$ and I_4 given by (5.23) and (5.15), respectively. Note that (5.24), contrary to (5.12), is defined in terms of the isochoric invariant $\bar{I}_1$ and that in (5.25) we have omitted the subscript "**f**" from the invariant $I_{4\mathbf{f}}$.

The planar sheets will be represented by an exponential term proposed, among several other polyconvex functions, by Balzani et al. [72] as a potentially suitable function for description of soft biological tissues. However, no practical application of the function in the field of biomechanics (or any other) is known to the author of this thesis. The function reads:

$$\Psi_{\mathbf{fs}} := \frac{a_{\mathbf{fs}}}{2b_{\mathbf{fs}}}(\exp(b_{\mathbf{fs}}(K_1 - 1)^2) - 1)\,. \tag{5.26}$$

Invariant K_1 is defined as [72, 71]:

$$K_1 := \text{tr}(\text{cof}(\mathbf{C})(\mathbf{n} \otimes \mathbf{n}))\,. \tag{5.27}$$

In general, the cofactor of an invertible linear transformation $\mathbf{L}$ is defined by [71]:

$$\mathrm{cof}(\mathbf{L}) \coloneqq \det(\mathbf{L})\mathbf{L}^{-\top} \tag{5.28}$$

(see also (4.68)). Since the right Cauchy-Green tensor $\mathbf{C}$ is symmetric, its inverse is also symmetric and we have:

$$\mathrm{cof}(\mathbf{C}) = \det(\mathbf{C})\mathbf{C}^{-\top} = \det(\mathbf{C})\mathbf{C}^{-1}\,; \tag{5.29}$$

Although it is perhaps not evident at first glance, invariant K_1 has a simple geometrical interpretation which can be revealed by rewriting the definition (5.27). To that end, we first insert (5.8) into (5.29) and express

$$\mathrm{cof}(\mathbf{C}) = \det(\mathbf{C})\mathbf{C}^{-1} = \det(\mathbf{F}^\top\mathbf{F})(\mathbf{F}^\top\mathbf{F})^{-1} = (\det(\mathbf{F}))^2\,\mathbf{F}^{-1}\mathbf{F}^{-\top} = (\mathrm{cof}(\mathbf{F}))^\top\mathrm{cof}(\mathbf{F})\,. \tag{5.30}$$

The result of (5.30) can be used in (5.27) and after some manipulation of the resulting expression, we obtain:

$$\begin{aligned} K_1 &= \mathrm{tr}(\mathrm{cof}(\mathbf{C})(\mathbf{n}\otimes\mathbf{n})) = \mathrm{tr}((\mathrm{cof}(\mathbf{F}))^\top\mathrm{cof}(\mathbf{F})(\mathbf{n}\otimes\mathbf{n})) \\ &= \mathrm{tr}(\mathrm{cof}(\mathbf{F})(\mathbf{n}\otimes\mathbf{n})(\mathrm{cof}(\mathbf{F}))^\top) = \mathrm{tr}((\mathrm{cof}(\mathbf{F})\mathbf{n})\otimes(\mathrm{cof}(\mathbf{F})\mathbf{n})) \\ &= (\mathrm{cof}(\mathbf{F})\mathbf{n})\cdot(\mathrm{cof}(\mathbf{F})\mathbf{n}) = \|\mathrm{cof}(\mathbf{F})\mathbf{n}\|^2\,. \end{aligned} \tag{5.31}$$

Thus, K_1 is the square of the magnitude of vector $\mathrm{cof}(\mathbf{F})\mathbf{n}$. The meaning of this vector explains the Nanson's formula (e.g. [72]) which basically says that $\mathrm{cof}(\mathbf{F})$ maps planar (i.e. 2-dimensional) elements in the reference configuration into deformed planar elements in the current configuration. The principle is similar to $\mathbf{F}$ which maps *line* elements, represented by vectors, into deformed line elements (see again Fig. 19). In order to give a precise meaning to $\mathrm{cof}(\mathbf{F})\mathbf{n}$, we must regard the unit vector $\mathbf{n}$ as representing a unit planar surface to which $\mathbf{n}$ is a normal. Such surface lies in the plane defined by vectors $\mathbf{f}$ and $\mathbf{s}$; thus it can be seen as representing a myocardial sheet. The Nanson's formula says that $\mathrm{cof}(\mathbf{F})$ is a linear transformation which maps $\mathbf{n}$ into another vector, $\mathrm{cof}(\mathbf{F})\mathbf{n}$, which represents the original surface after its deformation. The deformed surface is still planar (just like the line element represented by $\mathbf{Fv}$ in Fig. 19 is still straight), its normal coincide with the direction of $\mathrm{cof}(\mathbf{F})\mathbf{n}$ and its area equals to $\|\mathrm{cof}(\mathbf{F})\mathbf{n}\|$. Thus K_1 controls the deformation of a preferred planar element initially perpendicular to $\mathbf{n}$. We can emphasize the analogy between I_4 and K_1 by saying that $\sqrt{I_4}$ is the local stretch of a material fibre aligned with $\mathbf{f}$ and $\sqrt{K_1}$ is the local *areal* stretch of the material surface transverse to $\mathbf{n}$ [80].

The last term of the strain energy function will be a volumetric term

$$\Psi_{\mathrm{vol}} \coloneqq \frac{\kappa}{2}(J-1)^2 \tag{5.32}$$

in which κ is the bulk modulus which serves as a penalty parameter for imposing approximately incompressible behavior.

The full form of the proposed alternative strain-energy function reads:

$$\begin{aligned} \Psi_{\mathrm{alt}} &\coloneqq \Psi_{\mathrm{iso}} + \Psi_{\mathbf{f}} + \Psi_{\mathbf{fs}} + \Psi_{\mathrm{vol}} \\ &= \frac{a}{2b}(\exp(b(\bar{I}_1-3))-1) + \frac{a_{\mathbf{f}}}{2b_{\mathbf{f}}}(\exp(b_{\mathbf{f}}(I_4-1)^2)-1) + \frac{a_{\mathbf{fs}}}{2b_{\mathbf{fs}}}(\exp(b_{\mathbf{fs}}(K_1-1)^2)-1) \\ &\qquad + \frac{\kappa}{2}(J-1)^2\,. \end{aligned} \tag{5.33}$$

Similarly to the Holzapfel-Odgen model, the anisotropic terms $\Psi_{\mathbf{f}}$ and $\Psi_{\mathbf{fs}}$ will be included in the model only if $I_4 > 1$ and $K_1 > 1$, respectively. It must nevertheless be admitted that deactivation of $\Psi_{\mathbf{fs}}$ is debatable because it does not have so clear physical justification as the deactivation of $\Psi_{\mathbf{f}}$ has (fibres do not support compression). However, in the paper by Balzani et al. [72], $\Psi_{\mathbf{fs}}$ is defined only for $K_1 > 1$ and it is replaced by zero if $K_1 \leq 1$.

5.5 The Cauchy stress tensor

In order to determine material parameters in the proposed strain-energy function (5.33) and to implement the model into FE software Ansys, it is necessary to derive the expression for the Cauchy stress tensor. Hyperelastic materials in general satisfy the following relation between the strain-energy function Ψ and the *second Piola-Kirchhoff stress tensor*[1] $\mathbf{S}$ [66]:

$$\mathbf{S} = 2\,\nabla_{\mathbf{C}}\Psi\,. \tag{5.34}$$

The *Cauchy stress tensor* $\boldsymbol{\sigma}$ can then be obtained as follows [66]:

$$\boldsymbol{\sigma} = J^{-1}\mathbf{F}\mathbf{S}\mathbf{F}^{\top}\,. \tag{5.35}$$

The Cauchy stress tensor is a linear transformation which maps unit vectors $\mathbf{n}$ (which are normals to surfaces inside the current shape Ω_t) into *tractions* $\mathbf{t}$ (which are forces acting on those surfaces), i.e.:[2]

$$\mathbf{t} = \boldsymbol{\sigma}\mathbf{n}\,. \tag{5.36}$$

For the particular case of the strain-energy function Ψ_{alt}, given by (5.33), equation (5.34) can be expanded as follows[3]:

$$\begin{aligned}\mathbf{S} &= 2\left(\nabla_{\mathbf{C}}\Psi_{\text{iso}} + \nabla_{\mathbf{C}}\Psi_{\mathbf{f}} + \nabla_{\mathbf{C}}\Psi_{\mathbf{fs}} + \nabla_{\mathbf{C}}\Psi_{\text{vol}}\right)\\ &= 2\left(\Psi'_{\text{iso}}\nabla_{\mathbf{C}}\bar{I}_1 + \Psi'_{\mathbf{f}}\nabla_{\mathbf{C}}I_4 + \Psi'_{\mathbf{fs}}\nabla_{\mathbf{C}}K_1 + \Psi'_{\text{vol}}\nabla_{\mathbf{C}}J\right)\,.\end{aligned} \tag{5.37}$$

Here, Ψ'_{iso}, $\Psi'_{\mathbf{f}}$, $\Psi'_{\mathbf{fs}}$ and Ψ'_{vol} are the derivatives of the individual terms of the strain-erergy function Ψ_{alt} with respect to the corresponding invariants; they are given by:

$$\Psi'_{\text{iso}} = \frac{a}{2}\exp(b(\bar{I}_1 - 3))\,, \tag{5.38}$$

$$\Psi'_{\mathbf{f}} = a_{\mathbf{f}}(I_4 - 1)\exp(b_{\mathbf{f}}(I_4 - 1)^2)\,, \tag{5.39}$$

$$\Psi'_{\mathbf{fs}} = a_{\mathbf{fs}}(K_1 - 1)\exp(b_{\mathbf{fs}}(K_1 - 1)^2)\,, \tag{5.40}$$

$$\Psi'_{\text{vol}} = \kappa(J - 1)\,. \tag{5.41}$$

The *tensor generators* [71] $\nabla_{\mathbf{C}}\bar{I}_1$, $\nabla_{\mathbf{C}}I_4$, $\nabla_{\mathbf{C}}K_1$ and $\nabla_{\mathbf{C}}J$, that appear in (5.37), are independent of the specific forms of Ψ_{iso}, $\Psi_{\mathbf{f}}$, $\Psi_{\mathbf{fs}}$ and Ψ_{vol}. To proceed, it is now necessary to express them in terms of the right Cauchy-Green tensor, the structural tensors and the invariants. Such expressions can be derived using various combinations of the chain rule, the product rule and some other rules, theorems and identities which can all be found in the book by Noll [48], mostly in Chapter 6. As some of these identities will be used

[1] To see how the second Piola-Kirchhoff stress tensor, as well as the first one, arises in the general theory, consult Appendix A on p. 124 of [66].

[2] For a comprehensive explanation of the concept of stress, refer to Chapter III of the book [43] by Truesdell. Note that the unit normal $\mathbf{n}$ in (5.36) should not be confused with the sheet-normal direction.

[3] The first right-hand side of (5.37) originates from eq. (63.12) on p. 221 in [48] and the second from the chain rule.

repeatedly in many equations given below, from now on their usage will, in most cases, not be explicitly mentioned in the text because doing so would affect its readability.

We will start with finding the expression for $\nabla_{\mathbf{C}} J$. Using the fact that [48]

$$\nabla_{\mathbf{C}}(\det(\mathbf{C})) = \det(\mathbf{C})\mathbf{C}^{-\top} = \det(\mathbf{C})\mathbf{C}^{-1} \tag{5.42}$$

and recalling from (5.10) that $J = \sqrt{\det(\mathbf{C})}$, we can proceed as follows:

$$\nabla_{\mathbf{C}} J = \nabla_{\mathbf{C}} \sqrt{\det(\mathbf{C})} = \frac{1}{2}(\det(\mathbf{C}))^{-1/2}\, \nabla_{\mathbf{C}}(\det(\mathbf{C})) = \frac{1}{2}\sqrt{\det(\mathbf{C})}\, \mathbf{C}^{-1} = \frac{1}{2} J \mathbf{C}^{-1}\,. \tag{5.43}$$

The result of (5.43) is needed for the calculation of $\nabla_{\mathbf{C}} \bar{I}_1$. Beside that, we will need the definitions (5.13) and (5.23) of I_1 and $\bar{I}_1$, respectively. With the help of these equations, we can write:

$$\begin{aligned} \nabla_{\mathbf{C}} \bar{I}_1 &= \nabla_{\mathbf{C}}(J^{-2/3}\mathrm{tr}(\mathbf{C})) = J^{-2/3}\, \nabla_{\mathbf{C}}(\mathrm{tr}(\mathbf{C})) + \mathrm{tr}(\mathbf{C}) \nabla_{\mathbf{C}}(J^{-2/3}) \\ &= J^{-2/3}\, \mathbf{I} - \frac{2}{3} J^{-5/3}\, \mathrm{tr}(\mathbf{C}) \nabla_{\mathbf{C}} J = J^{-2/3}\, \mathbf{I} - \frac{1}{3} \bar{I}_1 \mathbf{C}^{-1}\,, \end{aligned} \tag{5.44}$$

where $\mathbf{I}$ is the identity tensor. Tensor $\nabla_{\mathbf{C}} I_4$ can be obtained easily because I_4 depends linearly on $\mathbf{C}$ by the definition (5.15). Consequently:

$$\nabla_{\mathbf{C}} I_4 = \nabla_{\mathbf{C}}(\mathrm{tr}(\mathbf{C}(\mathbf{f} \otimes \mathbf{f}))) = \mathbf{f} \otimes \mathbf{f}\,. \tag{5.45}$$

Derivation of $\nabla_{\mathbf{C}} K_1$ is more intricate. We start by introducing two special tensor products, $\underline{\otimes}$ and $\overline{\otimes}$, which Bellini and Federico [81] call *tensor-down* and *tensor-up*, respectively. They are defined by

$$(\mathbf{A} \,\underline{\otimes}\, \mathbf{B})\mathbf{M} \coloneqq \mathbf{A}\mathbf{M}\mathbf{B}^{\top}\,, \tag{5.46}$$

$$(\mathbf{A} \,\overline{\otimes}\, \mathbf{B})\mathbf{M} \coloneqq \mathbf{A}\mathbf{M}^{\top}\mathbf{B}^{\top}\,, \tag{5.47}$$

where $\mathbf{A}$, $\mathbf{B}$ and $\mathbf{M}$ are second order tensors. It can be seen from the above definitions that both products are linear mappings which transform second-order tensors into other second-order tensors. Combining (5.46) and (5.47), we can further define[1] [81]

$$\mathbf{A} \,\underline{\overline{\otimes}}\, \mathbf{B} \coloneqq \frac{1}{2}(\mathbf{A} \,\underline{\otimes}\, \mathbf{B} + \mathbf{B} \,\overline{\otimes}\, \mathbf{A})\,. \tag{5.48}$$

With this definition, the gradient of the inverse of $\mathbf{C}$ can be expressed as [82]

$$\nabla_{\mathbf{C}}(\mathbf{C}^{-1}) \coloneqq -\mathbf{C}^{-1} \,\underline{\overline{\otimes}}\, \mathbf{C}^{-1}\,. \tag{5.49}$$

The gradient of $\mathrm{cof}(\mathbf{C})$ can be obtained using (5.49), (5.42) and (5.29) as follows:

$$\begin{aligned} \nabla_{\mathbf{C}}(\mathrm{cof}(\mathbf{C})) &= \nabla_{\mathbf{C}}(\det(\mathbf{C})\mathbf{C}^{-1}) \\ &= (\mathbf{C}^{-1} \otimes \nabla_{\mathbf{C}}(\det(\mathbf{C})) + \det(\mathbf{C}) \nabla_{\mathbf{C}}(\mathbf{C}^{-1})) \\ &= \det(\mathbf{C})\,(\mathbf{C}^{-1} \otimes \mathbf{C}^{-1} - \mathbf{C}^{-1} \,\underline{\overline{\otimes}}\, \mathbf{C}^{-1})\,. \end{aligned} \tag{5.50}$$

[1] Holzapfel [82] uses the symbol "$\odot$" instead of "$\underline{\overline{\otimes}}$".

Using the result of (5.50), it can be seen that the gradient of K_1 satisfies:

$$\begin{aligned}(\nabla_{\mathbf{C}} K_1)\mathbf{M} &= \nabla_{\mathbf{C}}(\,\mathrm{tr}(\mathrm{cof}(\mathbf{C})(\mathbf{n}\otimes\mathbf{n}))\,)\mathbf{M} \\ &= \mathrm{tr}[\,(\nabla_{\mathbf{C}}(\mathrm{cof}(\mathbf{C}))\mathbf{M})(\mathbf{n}\otimes\mathbf{n})\,] \\ &= \det(\mathbf{C})\,\mathrm{tr}[\,((\mathbf{C}^{-1}\otimes\mathbf{C}^{-1})\mathbf{M})(\mathbf{n}\otimes\mathbf{n})\,] \\ &\qquad\qquad - \det(\mathbf{C})\,\mathrm{tr}[\,((\mathbf{C}^{-1}\,\overline{\otimes}\,\mathbf{C}^{-1})\mathbf{M})(\mathbf{n}\otimes\mathbf{n})\,] \\ &= \det(\mathbf{C})\,\mathrm{tr}(\mathbf{C}^{-1}(\mathbf{n}\otimes\mathbf{n}))\,\mathrm{tr}(\mathbf{C}^{-1}\mathbf{M}) \\ &\quad - \frac{1}{2}\det(\mathbf{C})[\,\mathrm{tr}(\mathbf{C}^{-1}\mathbf{M}\mathbf{C}^{-1}(\mathbf{n}\otimes\mathbf{n})) + \mathrm{tr}(\mathbf{C}^{-1}\mathbf{M}^{\top}\mathbf{C}^{-1}(\mathbf{n}\otimes\mathbf{n}))\,] \\ &= K_1\mathrm{tr}(\mathbf{C}^{-1}\mathbf{M}) - \det(\mathbf{C})\,\mathrm{tr}(\mathbf{C}^{-1}(\mathbf{n}\otimes\mathbf{n})\,\mathbf{C}^{-1}\mathbf{M}) \\ &= \mathrm{tr}[(K_1\mathbf{C}^{-1} - \det(\mathbf{C})\,\mathbf{C}^{-1}(\mathbf{n}\otimes\mathbf{n})\,\mathbf{C}^{-1})\mathbf{M}]\,.\end{aligned} \tag{5.51}$$

Thus we finally obtain:

$$\nabla_{\mathbf{C}} K_1 = K_1\mathbf{C}^{-1} - \det(\mathbf{C})\,\mathbf{C}^{-1}(\mathbf{n}\otimes\mathbf{n})\mathbf{C}^{-1}\,. \tag{5.52}$$

It would now be possible to express the second Piola-Kirchhoff tensor $\mathbf{S}$ in terms of the basic tensors and invariants by inserting the derived expressions for gradients into (5.37), but it is not necessary because we need only the Cauchy stress tensor $\boldsymbol{\sigma}$ which will now be derived. First, we substitute $\mathbf{S}$ in (5.35) by the right-hand side of (5.37); we obtain:

$$\boldsymbol{\sigma} = 2J^{-1}\left(\Psi'_{\mathrm{iso}}\,\mathbf{F}(\nabla_{\mathbf{C}}\bar{I}_1)\mathbf{F}^{\top} + \Psi'_{\mathbf{f}}\,\mathbf{F}(\nabla_{\mathbf{C}}I_4)\mathbf{F}^{\top} + \Psi'_{\mathbf{fs}}\,\mathbf{F}(\nabla_{\mathbf{C}}K_1)\mathbf{F}^{\top} + \Psi'_{\mathrm{vol}}\,\mathbf{F}(\nabla_{\mathbf{C}}J)\mathbf{F}^{\top}\right)\,. \tag{5.53}$$

It can be seen that we now need to provide the tensor generators $\mathbf{F}(\nabla_{\mathbf{C}}J)\mathbf{F}^{\top}$, $\mathbf{F}(\nabla_{\mathbf{C}}\bar{I}_1)\mathbf{F}^{\top}$, $\mathbf{F}(\nabla_{\mathbf{C}}I_4)\mathbf{F}^{\top}$ and $\mathbf{F}(\nabla_{\mathbf{C}}K_1)\mathbf{F}^{\top}$. Using the gradients (5.43), (5.44), (5.45) and (5.52) along with the relation (5.10) and the definitions (5.8), (5.11) and (5.28), these tensors can be obtained as follows:

$$\mathbf{F}(\nabla_{\mathbf{C}}J)\mathbf{F}^{\top} = \mathbf{F}\left(\frac{1}{2}J\mathbf{C}^{-1}\right)\mathbf{F}^{\top} = \frac{1}{2}J\,\mathbf{F}\mathbf{C}^{-1}\mathbf{F}^{\top} = \frac{1}{2}J\,\mathbf{F}\mathbf{F}^{-1}\mathbf{F}^{-\top}\mathbf{F}^{\top} = \frac{1}{2}J\,\mathbf{I}\,. \tag{5.54}$$

$$\begin{aligned}\mathbf{F}(\nabla_{\mathbf{C}}\bar{I}_1)\mathbf{F}^{\top} &= \mathbf{F}\left(J^{-2/3}\,\mathbf{I} - \frac{1}{3}\bar{I}_1\mathbf{C}^{-1}\right)\mathbf{F}^{\top} = J^{-2/3}\,\mathbf{F}\mathbf{I}\mathbf{F}^{\top} - \frac{1}{3}\bar{I}_1\,\mathbf{F}\mathbf{C}^{-1}\mathbf{F}^{\top} \\ &= J^{-2/3}\,\mathbf{F}\mathbf{F}^{\top} - \frac{1}{3}\bar{I}_1\,\mathbf{F}\mathbf{F}^{-1}\mathbf{F}^{-\top}\mathbf{F}^{\top} = \bar{\mathbf{B}} - \frac{1}{3}\bar{I}_1\,\mathbf{I}\,,\end{aligned} \tag{5.55}$$

$$\mathbf{F}(\nabla_{\mathbf{C}}I_4)\mathbf{F}^{\top} = \mathbf{F}(\mathbf{f}\otimes\mathbf{f})\mathbf{F}^{\top} = (\mathbf{F}\mathbf{f})\otimes(\mathbf{F}\mathbf{f})\,, \tag{5.56}$$

$$\begin{aligned}\mathbf{F}(\nabla_{\mathbf{C}}K_1)\mathbf{F}^{\top} &= \mathbf{F}\left(K_1\mathbf{C}^{-1} - \det(\mathbf{C})\,\mathbf{C}^{-1}(\mathbf{n}\otimes\mathbf{n})\mathbf{C}^{-1}\right)\mathbf{F}^{\top} \\ &= K_1\mathbf{F}\mathbf{F}^{-1}\mathbf{F}^{-\top}\mathbf{F}^{\top} - (\det(\mathbf{F}))^2\,\mathbf{F}\mathbf{F}^{-1}\mathbf{F}^{-\top}(\mathbf{n}\otimes\mathbf{n})\mathbf{F}^{-1}\mathbf{F}^{-\top}\mathbf{F}^{\top} \\ &= K_1\mathbf{I} - (\det(\mathbf{F}))^2\,(\mathbf{F}^{-\top}\mathbf{n})\otimes(\mathbf{F}^{-\top}\mathbf{n}) \\ &= K_1\mathbf{I} - (\mathrm{cof}(\mathbf{F})\mathbf{n})\otimes(\mathrm{cof}(\mathbf{F})\mathbf{n})\,.\end{aligned} \tag{5.57}$$

The final expression for the Cauchy stress tensor $\boldsymbol{\sigma}$ is obtained by inserting the results of (5.54)–(5.57) into (5.53). The latter then reads:

$$\begin{aligned}\boldsymbol{\sigma} = 2J^{-1}\Bigg(\Psi'_{\mathrm{iso}}\left(\bar{\mathbf{B}} - \frac{1}{3}\bar{I}_1\,\mathbf{I}\right) + \Psi'_{\mathbf{f}}\,(\mathbf{F}\mathbf{f})\otimes(\mathbf{F}\mathbf{f}) + \Psi'_{\mathbf{fs}}\,(K_1\,\mathbf{I} - (\mathrm{cof}(\mathbf{F})\mathbf{n})\otimes(\mathrm{cof}(\mathbf{F})\mathbf{n}))\Bigg) \\ + \Psi'_{\mathrm{vol}}\,\mathbf{I}\,.\end{aligned} \tag{5.58}$$

5.6 Estimation of material parameters

Once the general equation (5.58) for the Cauchy stress tensor is known, it can be used to find a suitable set of material parameters that would ensure an optimal correspondence between the calculated response of the model and the experimental data plotted in Fig. 22. In order to do so, equation (5.58) must first be expressed in the component form with respect to an orthonormal basis ($\mathbf{f}$, $\mathbf{s}$, $\mathbf{n}$). After that, the particular forms of the deformation gradient $\mathbf{F}$ for biaxial and simple shear deformations must be formulated and inserted into the stress relation. In this way, one can obtain two scalar functions describing the normal stresses in $\mathbf{f}$ and $\mathbf{s}$ directions during biaxial loading and another six functions for the shear stresses corresponding to the six simple shear modes depicted in Fig. 21B. Afterwards, a nonlinear least squares problem can be formulated and solved. In this work, the solution was performed in Matlab using the Gauss-Newton algorithm. The penalty parameter was set to $\kappa = 1$ MPa and it was considered fixed while the rest of the parameters were iteratively adjusted. The final values obtained from the fitting process are given in Table. 5 and the corresponding stress-strain curves obtained from the model for all considered tests are plotted in Fig. 23 against the experimental data from Sommer et al. [12].

Table 5: Values of material parameters for the strain-energy function (5.33) which were used to fit the corresponding stress response (5.58) to the experimental data extracted from Sommer et al. [12].

a	b	$a_{\mathbf{f}}$	$b_{\mathbf{f}}$	$a_{\mathbf{fs}}$	$b_{\mathbf{fs}}$	κ
(kPa)	(–)	(kPa)	(–)	(kPa)	(–)	(kPa)
1.1672	6.4795	1.0270	38.8499	0.2807	11.6417	10^3

It can be seen from Fig. 23 that the experimental results can be reproduced very well by the proposed model. However, it must be pointed out that there is one significant drawback of the model which, to some extent, limits its suitability for the description of myocardium. The problem is that the model exhibits stiffer behavior in the **fn** mode than in the **fs** mode, while the experiments of Sommer et al. [12] (Fig. 22) show the opposite. This is evident from the small text boxes attached to the shear responses in Fig. 23. Each of these boxes displays the shear stress calculated for the shear strain of 0.4474. It can be seen that the **fn** mode is indeed stiffer than the **fs** mode, although the difference is quite small. Similarly, the **sn** mode is slightly stiffer than the **sf** mode, whereas in experiments (Fig. 22) they are almost identical. The explanation of this behavior of the model is simple. If the term $\Psi_{\mathbf{fs}}$ was not included in the strain-energy function (5.33), the response of the resulting model would be the same for the associated modes **fs**, **fn** as well as for the modes **sf**, **sn** and likewise for the modes **nf**, **ns**. The term $\Psi_{\mathbf{fs}}$ (dependent on K_1) distinguishes the **fs** mode from the **fn** mode and the **sf** mode from the **sn** mode which means that its role is similar to that of the coupling term $\Psi_{\mathbf{fs}}$ (dependent on $I_{8\mathbf{fs}}$) in the Holzapfel-Ogden model. However, contrary to that model, in the model used here the function $\Psi_{\mathbf{fs}}$ makes the **fn** mode slightly stiffer than the **fs** mode, and the **sn** mode stiffer than the **sf** mode. This is so because (if we assume a fully incompressible behavior) the **fs** and **sf** modes do not produce any change in the sheet area which means that $K_1 = 1$ and thus $\Psi_{\mathbf{fs}}$ vanishes. On the contrary, the shear modes **fn** and **sn** clearly do change the sheet area. In these modes $K_1 = 1 + (\text{shear strain})^2$ which means that there is non-zero contribution of $\Psi_{\mathbf{fs}}$ to the shear stress.

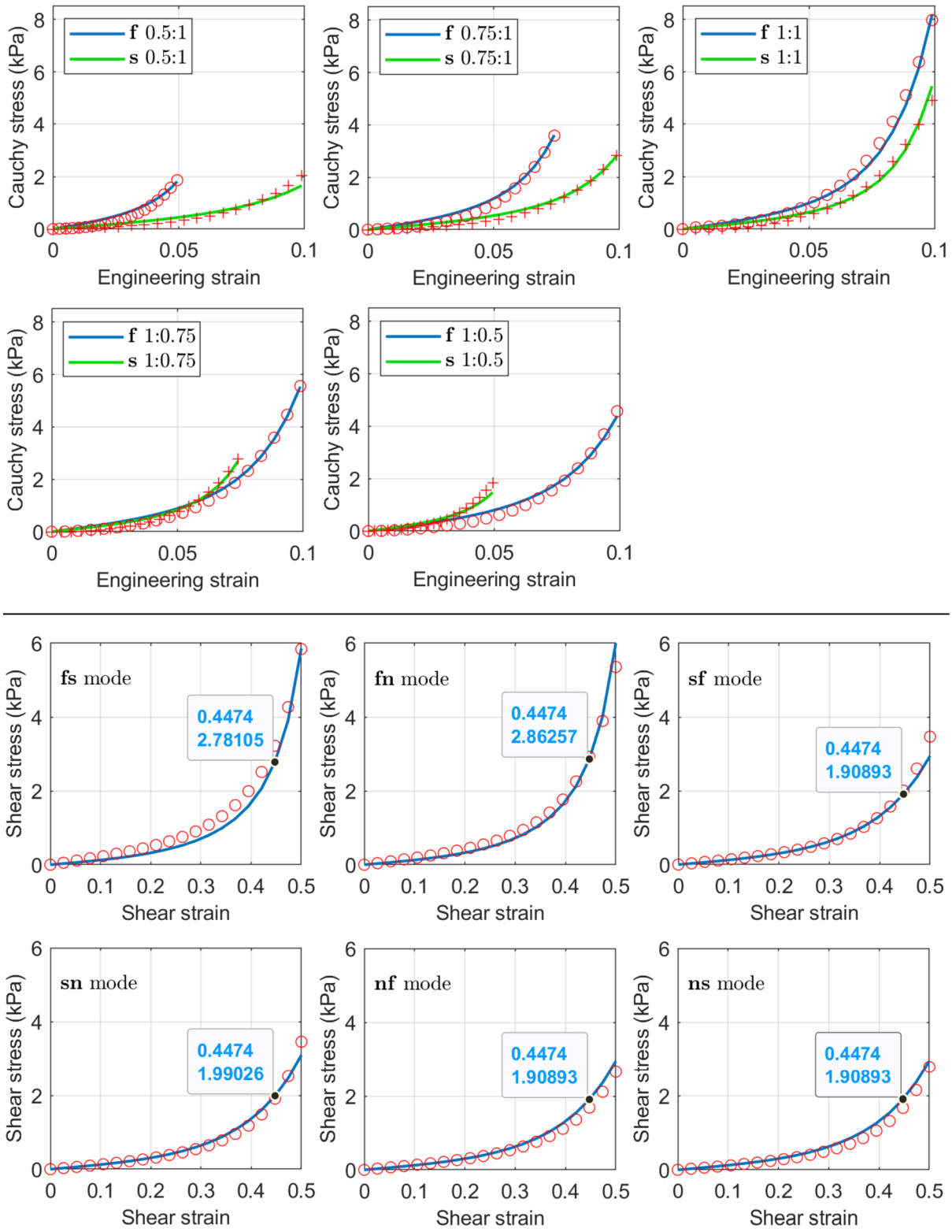

Fig. 23: Fit of the model (5.33) (solid curves) to the experimental data extracted from Sommer et al. [12] (red circles and plus signs). The same experimental data were plotted earlier in Fig. 22. The top 5 graphs show the biaxial responses while the bottom six graphs compare responses to the simple shear tests. The material parameters used are given in Table 5. See Fig. 21 for the explanation of shear modes and the caption to Fig. 22 for the description of biaxial testing protocol.

As the differences between the associated pairs of modes are rather small (in the experiments as well as in the response of the model), the described shortcoming of the model should not have a significant impact on the results, but if we were to simulate, e.g., the mechanics of pig heart, then the model could probably not be used because it has been shown that pig myocardium exhibits more pronounced differences between individual shear modes [39] with the following stiffness order: **fs** > **fn** > **sf** > **sn** > **nf** ≈ **ns**.[1] Also, looking at the shear responses in Fig. 22, one might come to the conclusion that distinguishing between the associated pairs of modes is perhaps not worth the effort because, for some constitutive models, the difference between the fitted response and the experimental data could easily be greater than that between the most distinct associated modes **fs** and **fn** in Fig. 22. If we decided to ignore these distinctions, it could be sufficient to use, e.g., the nearly incompressible Holzapfel-Ogden model without the coupling term, although in such case the agreement between the model and the experimental data would probably not be as good as in Fig. 23. However, this option was not investigated in this study.

Another shortcoming of the model is that the deformed fibre direction, **Ff**, will in most cases not be perpendicular to the deformed sheet-normal direction, cof(**F**)**n**, which physically does not make much sense (deformed fibres do not lie in the plane of the sheet which they should form). Thus the proposed model should probably be viewed only as an interesting alternative to the existing models, which can accurately reproduce combined biaxial and simple shear tests but whose applicability to human myocardium should be further examined.

5.7 Elasticity tensors

The two most important quantities that are needed for the implementation of a hyperelastic model into FE software Ansys by means of the general material subroutine `UserMat` [83] (written in Fortran) are the Cauchy stress tensor, $\boldsymbol{\sigma}$, and the *Jaumann tangent stiffness tensor*, $\mathbb{c}^J$. The first of these was already derived in Sec. 5.5 (eq. (5.58)). The second one will be derived in this section. The whole procedure can be divided into three steps. First, the *material elasticity tensor* $\mathbb{C}$ must be derived. Afterwards, its spatial counterpart $\mathbb{c}$, called the *spatial elasticity tensor*, can be obtained by the *push-forward operation* (see [81]) applied on $\mathbb{C}$. Finally, the Jaumann tensor $\mathbb{c}^J$ can be calculated from $\mathbb{c}$.

The material elasticity tensor is defined in terms of the second Piola-Kirchhoff stress **S** and the right Cauchy-Green tensor **C** as [54]:

$$\mathbb{C} \coloneqq 2\,\nabla_{\mathbf{C}}\mathbf{S}\,. \tag{5.59}$$

Here, **S** is considered to be a tensor-valued function of **C**. In the present case, such function can be obtained from the specific form of **S** given in (5.37). It reads:

$$\mathbf{S} = 2\left(\Psi'_{\text{iso}}\,\nabla\bar{I}_1 + \Psi'_{\mathbf{f}}\,\nabla I_4 + \Psi'_{\mathbf{fs}}\,\nabla K_1 + \Psi'_{\text{vol}}\,\nabla J\right)\,, \tag{5.60}$$

where the gradients $\nabla\bar{I}_1$, ∇I_4, ∇K_1 and ∇J are also functions of **C**. For instance, $\nabla\bar{I}_1$ is

[1] It should be noted here that in Fig. 6 of [39], which shows responses of pig myocardium to simple shear, the symbols for the modes **fs** and **fn** were mistakenly switched, as pointed out by Holzapfel and Ogden [14]. Thus the figure erroneously claims that **fn** > **fs**, but it is clear from the text of the paper that the stiffest mode was in fact **fs**.

defined by $(\nabla \bar{I}_1)(\mathbf{C}) \coloneqq \nabla_{\mathbf{C}} \bar{I}_1$. Equation (5.60) can be inserted into (5.59) producing:

$$\begin{aligned}
\mathbb{C} &= 2\,\nabla_{\mathbf{C}}\mathbf{S} \\
&= 4\,\nabla_{\mathbf{C}}(\Psi'_{\text{iso}}\,\nabla \bar{I}_1 + \Psi'_{\mathbf{f}}\,\nabla I_4 + \Psi'_{\mathbf{fs}}\,\nabla K_1 + \Psi'_{\text{vol}}\,\nabla J) \\
&= 4\,(\,\nabla_{\mathbf{C}}\bar{I}_1 \otimes \nabla_{\mathbf{C}}\Psi'_{\text{iso}} + \nabla_{\mathbf{C}} I_4 \otimes \nabla_{\mathbf{C}}\Psi'_{\mathbf{f}} + \nabla_{\mathbf{C}} K_1 \otimes \nabla_{\mathbf{C}}\Psi'_{\mathbf{fs}} + \nabla_{\mathbf{C}} J \otimes \nabla_{\mathbf{C}}\Psi'_{\text{vol}} \\
&\qquad\qquad + \Psi'_{\text{iso}}\,\nabla^{(2)}_{\mathbf{C}}\bar{I}_1 + \Psi'_{\mathbf{f}}\,\nabla^{(2)}_{\mathbf{C}} I_4 + \Psi'_{\mathbf{fs}}\,\nabla^{(2)}_{\mathbf{C}} K_1 + \Psi'_{\text{vol}}\,\nabla^{(2)}_{\mathbf{C}} J\,) \\
&= 4\,(\,\Psi''_{\text{iso}}\nabla_{\mathbf{C}}\bar{I}_1 \otimes \nabla_{\mathbf{C}}\bar{I}_1 + \Psi''_{\mathbf{f}}\nabla_{\mathbf{C}} I_4 \otimes \nabla_{\mathbf{C}} I_4 + \Psi''_{\mathbf{fs}}\nabla_{\mathbf{C}} K_1 \otimes \nabla_{\mathbf{C}} K_1 + \Psi''_{\text{vol}}\nabla_{\mathbf{C}} J \otimes \nabla_{\mathbf{C}} J \\
&\qquad\qquad + \Psi'_{\text{iso}}\,\nabla^{(2)}_{\mathbf{C}}\bar{I}_1 + \Psi'_{\mathbf{f}}\,\nabla^{(2)}_{\mathbf{C}} I_4 + \Psi'_{\mathbf{fs}}\,\nabla^{(2)}_{\mathbf{C}} K_1 + \Psi'_{\text{vol}}\,\nabla^{(2)}_{\mathbf{C}} J\,)\,.
\end{aligned} \tag{5.61}$$

The symbol "$^{(2)}$" in the above expressions denotes the second gradient[1]; for instance, the second gradient of $\bar{I}_1$ can be obtained as $\nabla^{(2)}_{\mathbf{C}}\bar{I}_1 = \nabla_{\mathbf{C}}(\nabla \bar{I}_1)$. The double prime symbol "$''$" denotes the second derivatives of the individual terms of Ψ_{alt} with respect to the corresponding invariants; these derivatives can be obtained directly from (5.38)–(5.41) in the form:

$$\Psi''_{\text{iso}} = \frac{ab}{2}\exp(b(\bar{I}_1 - 3))\,, \tag{5.62}$$

$$\Psi''_{\mathbf{f}} = a_{\mathbf{f}}\exp(b_{\mathbf{f}}(I_4 - 1)^2)(2b_{\mathbf{f}}(I_4 - 1)^2 + 1)\,, \tag{5.63}$$

$$\Psi''_{\mathbf{fs}} = a_{\mathbf{fs}}\exp(b_{\mathbf{fs}}(K_1 - 1)^2)(2b_{\mathbf{fs}}(K_1 - 1)^2 + 1)\,, \tag{5.64}$$

$$\Psi''_{\text{vol}} = \kappa\,. \tag{5.65}$$

The tensor products and the second gradients in (5.61) can all be calculated from the first gradients $\nabla_{\mathbf{C}} J$, $\nabla_{\mathbf{C}}\bar{I}_1$, $\nabla_{\mathbf{C}} I_4$ and $\nabla_{\mathbf{C}} K_1$ which are given by (5.43), (5.44), (5.45) and (5.52), respectively. First, we will calculate the tensor products:

$$\nabla_{\mathbf{C}} J \otimes \nabla_{\mathbf{C}} J = \left(\frac{1}{2}J\mathbf{C}^{-1}\right) \otimes \left(\frac{1}{2}J\mathbf{C}^{-1}\right) = \frac{1}{4}\det(\mathbf{C})\,\mathbf{C}^{-1} \otimes \mathbf{C}^{-1}\,, \tag{5.66}$$

$$\begin{aligned}
\nabla_{\mathbf{C}}\bar{I}_1 \otimes \nabla_{\mathbf{C}}\bar{I}_1 &= \left(J^{-2/3}\,\mathbf{I} - \frac{1}{3}\bar{I}_1\mathbf{C}^{-1}\right) \otimes \left(J^{-2/3}\,\mathbf{I} - \frac{1}{3}\bar{I}_1\mathbf{C}^{-1}\right) \\
&= J^{-4/3}\,\mathbf{I} \otimes \mathbf{I} - \frac{1}{3}J^{-2/3}\,\bar{I}_1\,(\,\mathbf{I} \otimes \mathbf{C}^{-1} + \mathbf{C}^{-1} \otimes \mathbf{I}\,) + \frac{1}{9}\bar{I}_1^2\,\mathbf{C}^{-1} \otimes \mathbf{C}^{-1},
\end{aligned} \tag{5.67}$$

$$\nabla_{\mathbf{C}} I_4 \otimes \nabla_{\mathbf{C}} I_4 = (\mathbf{f} \otimes \mathbf{f}) \otimes (\mathbf{f} \otimes \mathbf{f})\,, \tag{5.68}$$

$$\begin{aligned}
\nabla_{\mathbf{C}} K_1 \otimes \nabla_{\mathbf{C}} K_1 &= \left[K_1\mathbf{C}^{-1} - \det(\mathbf{C})\,\mathbf{C}^{-1}(\mathbf{n} \otimes \mathbf{n})\mathbf{C}^{-1}\right] \\
&\qquad\qquad \otimes \left[K_1\mathbf{C}^{-1} - \det(\mathbf{C})\,\mathbf{C}^{-1}(\mathbf{n} \otimes \mathbf{n})\mathbf{C}^{-1}\right] \\
&= K_1^2\,\mathbf{C}^{-1} \otimes \mathbf{C}^{-1} - K_1\det(\mathbf{C})\left[\mathbf{C}^{-1} \otimes (\mathbf{C}^{-1}(\mathbf{n} \otimes \mathbf{n})\mathbf{C}^{-1}) \right. \\
&\qquad\qquad \left. + (\mathbf{C}^{-1}(\mathbf{n} \otimes \mathbf{n})\mathbf{C}^{-1}) \otimes \mathbf{C}^{-1}\right] \\
&\qquad + (\det(\mathbf{C}))^2(\mathbf{C}^{-1}(\mathbf{n} \otimes \mathbf{n})\mathbf{C}^{-1}) \otimes (\mathbf{C}^{-1}(\mathbf{n} \otimes \mathbf{n})\mathbf{C}^{-1})\,.
\end{aligned} \tag{5.69}$$

Expressions for the second gradients $\nabla^{(2)}_{\mathbf{C}} J$, $\nabla^{(2)}_{\mathbf{C}}\bar{I}_1$ and $\nabla^{(2)}_{\mathbf{C}} I_4$ can be obtained relatively

[1] This notation for the second gradient was adopted from [48].

easily:

$$\begin{aligned}\nabla^{(2)}_{\mathbf{C}} J &= \nabla_{\mathbf{C}}\left(\frac{1}{2} J \mathbf{C}^{-1}\right) = \frac{1}{2}(\mathbf{C}^{-1}\otimes\nabla_{\mathbf{C}} J + J\,\nabla_{\mathbf{C}}(\mathbf{C}^{-1})) \\ &= \frac{1}{4}\,J(\mathbf{C}^{-1}\otimes\mathbf{C}^{-1} - 2\,\mathbf{C}^{-1}\,\underline{\otimes}\,\mathbf{C}^{-1})\,,\end{aligned} \tag{5.70}$$

$$\begin{aligned}\nabla^{(2)}_{\mathbf{C}} \bar{I}_1 &= \nabla_{\mathbf{C}}(J^{-2/3}\mathbf{I}) - \frac{1}{3}\nabla_{\mathbf{C}}(\bar{I}_1\mathbf{C}^{-1}) \\ &= \mathbf{I}\otimes\nabla_{\mathbf{C}}(J^{-2/3}) - \frac{1}{3}\,\mathbf{C}^{-1}\otimes\nabla_{\mathbf{C}}\bar{I}_1 - \frac{1}{3}\bar{I}_1\nabla_{\mathbf{C}}(\mathbf{C}^{-1}) \\ &= -\frac{2}{3}J^{-5/3}\,\mathbf{I}\otimes\nabla_{\mathbf{C}} J - \frac{1}{3}J^{-2/3}\,\mathbf{C}^{-1}\otimes\mathbf{I} + \frac{1}{9}\bar{I}_1\mathbf{C}^{-1}\otimes\mathbf{C}^{-1} + \frac{1}{3}\bar{I}_1\mathbf{C}^{-1}\,\underline{\otimes}\,\mathbf{C}^{-1} \\ &= -\frac{1}{3}J^{-2/3}\,(\,\mathbf{I}\otimes\mathbf{C}^{-1} + \mathbf{C}^{-1}\otimes\mathbf{I}\,) + \frac{1}{9}\bar{I}_1\,(\,\mathbf{C}^{-1}\otimes\mathbf{C}^{-1} + 3\,\mathbf{C}^{-1}\,\underline{\otimes}\,\mathbf{C}^{-1}\,)\,,\end{aligned} \tag{5.71}$$

$$\nabla^{(2)}_{\mathbf{C}} I_4 = \nabla_{\mathbf{C}}(\mathbf{f}\otimes\mathbf{f}) = \mathbf{0}\,. \tag{5.72}$$

Derivation of $\nabla^{(2)}_{\mathbf{C}} K_1$ requires more effort. We will start by expressing this gradient in terms of several simpler ones, using equation (5.52):

$$\begin{aligned}\nabla^{(2)}_{\mathbf{C}} K_1 &= \nabla_{\mathbf{C}}(K_1\mathbf{C}^{-1} - \det(\mathbf{C})\,\mathbf{C}^{-1}(\mathbf{n}\otimes\mathbf{n})\mathbf{C}^{-1}) \\ &= \nabla_{\mathbf{C}}(K_1\mathbf{C}^{-1}) - \nabla_{\mathbf{C}}(\det(\mathbf{C})\,\mathbf{C}^{-1}(\mathbf{n}\otimes\mathbf{n})\mathbf{C}^{-1}) \\ &= \nabla_{\mathbf{C}}(K_1\mathbf{C}^{-1}) - (\mathbf{C}^{-1}(\mathbf{n}\otimes\mathbf{n})\mathbf{C}^{-1})\otimes\nabla_{\mathbf{C}}(\det(\mathbf{C})) \\ &\qquad - \det(\mathbf{C})\nabla_{\mathbf{C}}(\mathbf{C}^{-1}(\mathbf{n}\otimes\mathbf{n})\mathbf{C}^{-1})\,.\end{aligned} \tag{5.73}$$

The first gradient in the final expression in (5.73) is given by

$$\begin{aligned}\nabla_{\mathbf{C}}(K_1\mathbf{C}^{-1}) &= \mathbf{C}^{-1}\otimes\nabla_{\mathbf{C}} K_1 + K_1\nabla_{\mathbf{C}}(\mathbf{C}^{-1}) \\ &= K_1\mathbf{C}^{-1}\otimes\mathbf{C}^{-1} - \det(\mathbf{C})\,\mathbf{C}^{-1}\otimes(\mathbf{C}^{-1}(\mathbf{n}\otimes\mathbf{n})\mathbf{C}^{-1}) - K_1\mathbf{C}^{-1}\,\underline{\otimes}\,\mathbf{C}^{-1} \\ &= K_1(\mathbf{C}^{-1}\otimes\mathbf{C}^{-1} - \mathbf{C}^{-1}\,\underline{\otimes}\,\mathbf{C}^{-1}) - \det(\mathbf{C})\,\mathbf{C}^{-1}\otimes(\mathbf{C}^{-1}(\mathbf{n}\otimes\mathbf{n})\mathbf{C}^{-1})\end{aligned} \tag{5.74}$$

and the second one, $\nabla_{\mathbf{C}}(\det(\mathbf{C}))$, is given by (5.42). The third gradient can be expressed as follows:

$$\begin{aligned}\nabla_{\mathbf{C}}(\mathbf{C}^{-1}(\mathbf{n}\otimes\mathbf{n})\mathbf{C}^{-1})\,\mathbf{M} &= (\nabla_{\mathbf{C}}(\mathbf{C}^{-1})\,\mathbf{M})(\mathbf{n}\otimes\mathbf{n})\mathbf{C}^{-1} + \mathbf{C}^{-1}(\nabla_{\mathbf{C}}((\mathbf{n}\otimes\mathbf{n})\mathbf{C}^{-1})\mathbf{M}) \\ &= (\nabla_{\mathbf{C}}(\mathbf{C}^{-1})\,\mathbf{M})(\mathbf{n}\otimes\mathbf{n})\mathbf{C}^{-1} + \mathbf{C}^{-1}(\mathbf{n}\otimes\mathbf{n})(\nabla_{\mathbf{C}}(\mathbf{C}^{-1})\,\mathbf{M}) \\ &= -((\mathbf{C}^{-1}\,\underline{\otimes}\,\mathbf{C}^{-1})\,\mathbf{M})(\mathbf{n}\otimes\mathbf{n})\mathbf{C}^{-1} - \mathbf{C}^{-1}(\mathbf{n}\otimes\mathbf{n})((\mathbf{C}^{-1}\,\underline{\otimes}\,\mathbf{C}^{-1})\,\mathbf{M}) \\ &= -(\mathbf{C}^{-1}\mathbf{M}\mathbf{C}^{-1})(\mathbf{n}\otimes\mathbf{n})\mathbf{C}^{-1} - (\mathbf{C}^{-1}\mathbf{M}^{\top}\mathbf{C}^{-1})(\mathbf{n}\otimes\mathbf{n})\mathbf{C}^{-1} \\ &\qquad - \mathbf{C}^{-1}(\mathbf{n}\otimes\mathbf{n})(\mathbf{C}^{-1}\mathbf{M}\mathbf{C}^{-1}) - \mathbf{C}^{-1}(\mathbf{n}\otimes\mathbf{n})(\mathbf{C}^{-1}\mathbf{M}^{\top}\mathbf{C}^{-1}) \\ &= -\mathbf{C}^{-1}\mathbf{M}(\mathbf{C}^{-1}(\mathbf{n}\otimes\mathbf{n})\mathbf{C}^{-1}) - \mathbf{C}^{-1}\mathbf{M}^{\top}(\mathbf{C}^{-1}(\mathbf{n}\otimes\mathbf{n})\mathbf{C}^{-1}) \\ &\qquad - (\mathbf{C}^{-1}(\mathbf{n}\otimes\mathbf{n})\mathbf{C}^{-1})\mathbf{M}\mathbf{C}^{-1} - (\mathbf{C}^{-1}(\mathbf{n}\otimes\mathbf{n})\mathbf{C}^{-1})\mathbf{M}^{\top}\mathbf{C}^{-1} \\ &= -[\mathbf{C}^{-1}\,\underline{\otimes}\,(\mathbf{C}^{-1}(\mathbf{n}\otimes\mathbf{n})\mathbf{C}^{-1})]\,\mathbf{M} - [(\mathbf{C}^{-1}(\mathbf{n}\otimes\mathbf{n})\mathbf{C}^{-1})\,\underline{\otimes}\,\mathbf{C}^{-1}]\,\mathbf{M} \\ &= -[\mathbf{C}^{-1}\,\underline{\otimes}\,(\mathbf{C}^{-1}(\mathbf{n}\otimes\mathbf{n})\mathbf{C}^{-1}) + (\mathbf{C}^{-1}(\mathbf{n}\otimes\mathbf{n})\mathbf{C}^{-1})\,\underline{\otimes}\,\mathbf{C}^{-1}]\,\mathbf{M}\end{aligned} \tag{5.75}$$

Since (5.75) must hold for all second order tensors $\mathbf{M}$, it follows that

$$\nabla_{\mathbf{C}}(\mathbf{C}^{-1}(\mathbf{n}\otimes\mathbf{n})\mathbf{C}^{-1}) = -\mathbf{C}^{-1}\,\underline{\otimes}\,(\mathbf{C}^{-1}(\mathbf{n}\otimes\mathbf{n})\mathbf{C}^{-1}) - (\mathbf{C}^{-1}(\mathbf{n}\otimes\mathbf{n})\mathbf{C}^{-1})\,\underline{\otimes}\,\mathbf{C}^{-1}\,. \tag{5.76}$$

If we now insert (5.74), (5.42) and (5.76) into (5.73), we obtain the final expression for the second gradient of the invariant K_1:

$$\begin{aligned}
\nabla^{(2)}_{\mathbf{C}} K_1 &= \nabla_{\mathbf{C}}(K_1 \mathbf{C}^{-1} - \det(\mathbf{C})\, \mathbf{C}^{-1}(\mathbf{n}\otimes\mathbf{n})\mathbf{C}^{-1}) \\
&= \nabla_{\mathbf{C}}(K_1 \mathbf{C}^{-1}) - \nabla_{\mathbf{C}}(\det(\mathbf{C})\, \mathbf{C}^{-1}(\mathbf{n}\otimes\mathbf{n})\mathbf{C}^{-1}) \\
&= \nabla_{\mathbf{C}}(K_1 \mathbf{C}^{-1}) - (\mathbf{C}^{-1}(\mathbf{n}\otimes\mathbf{n})\mathbf{C}^{-1}) \otimes \nabla_{\mathbf{C}}(\det(\mathbf{C})) \\
&\qquad\qquad - \det(\mathbf{C}) \nabla_{\mathbf{C}}(\mathbf{C}^{-1}(\mathbf{n}\otimes\mathbf{n})\mathbf{C}^{-1}) \qquad (5.77) \\
&= K_1(\mathbf{C}^{-1}\otimes\mathbf{C}^{-1} - \mathbf{C}^{-1}\,\underline{\overline{\otimes}}\,\mathbf{C}^{-1}) \\
&\qquad - \det(\mathbf{C})\,[\mathbf{C}^{-1}\otimes(\mathbf{C}^{-1}(\mathbf{n}\otimes\mathbf{n})\mathbf{C}^{-1}) + (\mathbf{C}^{-1}(\mathbf{n}\otimes\mathbf{n})\mathbf{C}^{-1})\otimes\mathbf{C}^{-1}] \\
&\qquad + \det(\mathbf{C})\,[\mathbf{C}^{-1}\,\underline{\overline{\otimes}}\,(\mathbf{C}^{-1}(\mathbf{n}\otimes\mathbf{n})\mathbf{C}^{-1}) + (\mathbf{C}^{-1}(\mathbf{n}\otimes\mathbf{n})\mathbf{C}^{-1})\,\underline{\overline{\otimes}}\,\mathbf{C}^{-1}]\,.
\end{aligned}$$

It would now be possible to insert the above expressions for the second gradients and the fourth-order tensor products into (5.61) and thus obtain the full form of the material elasticity tensor $\mathbb{C}$. But such explicit form of $\mathbb{C}$ is not needed for the implementation of the material model and therefore we will move on to the next step and express the spatial elasticity tensor $\mathbb{c}$ which is defined by [81]:

$$\mathbb{c} := J^{-1}\,\mathbb{F}\,\mathbb{C}\,\mathbb{F}^{\top}\,. \qquad (5.78)$$

The above definition uses fourth-order tensors

$$\mathbb{F} := \mathbf{F}\,\underline{\otimes}\,\mathbf{F} \qquad \text{and} \qquad \mathbb{F}^{\top} := \mathbf{F}^{\top}\,\underline{\otimes}\,\mathbf{F}^{\top} \qquad (5.79)$$

which are linear mappings transforming second-order tensors into second-order tensors.[1] Using the general form of $\mathbb{C}$ given in (5.61), the right-hand side of (5.78) can be expanded as follows:

$$\begin{aligned}
\mathbb{c} &= J^{-1}\,\mathbb{F}\,\mathbb{C}\,\mathbb{F}^{\top} \\
&= 4J^{-1}\,[\,\Psi''_{\text{iso}}\,\mathbb{F}\,(\nabla_{\mathbf{C}}\bar{I}_1\otimes\nabla_{\mathbf{C}}\bar{I}_1)\,\mathbb{F}^{\top} + \Psi''_{\mathbf{f}}\,\mathbb{F}\,(\nabla_{\mathbf{C}}I_4\otimes\nabla_{\mathbf{C}}I_4)\,\mathbb{F}^{\top} \\
&\qquad\qquad + \Psi''_{\mathbf{fs}}\,\mathbb{F}\,(\nabla_{\mathbf{C}}K_1\otimes\nabla_{\mathbf{C}}K_1)\,\mathbb{F}^{\top} + \Psi''_{\text{vol}}\,\mathbb{F}\,(\nabla_{\mathbf{C}}J\otimes\nabla_{\mathbf{C}}J)\,\mathbb{F}^{\top} \\
&\quad + \Psi'_{\text{iso}}\,\mathbb{F}\,(\nabla^{(2)}_{\mathbf{C}}\bar{I}_1)\,\mathbb{F}^{\top} + \Psi'_{\mathbf{f}}\,\mathbb{F}\,(\nabla^{(2)}_{\mathbf{C}}I_4)\,\mathbb{F}^{\top} + \Psi'_{\mathbf{fs}}\,\mathbb{F}\,(\nabla^{(2)}_{\mathbf{C}}K_1)\,\mathbb{F}^{\top} + \Psi'_{\text{vol}}\,\mathbb{F}\,(\nabla^{(2)}_{\mathbf{C}}J)\,\mathbb{F}^{\top}\,]\,.
\end{aligned} \qquad (5.80)$$

In order to obtain $\mathbb{c}$ in a form suitable for implementation, we must derive equations for all the tensors inside the square brackets in (5.80). The following equations provide some intermediate results:

$$\begin{aligned}
[\mathbb{F}\,(J^{-4/3}\,\mathbf{I}\otimes\mathbf{I})\,\mathbb{F}^{\top}]\,\mathbf{M} &= J^{-4/3}\,\mathbb{F}\,((\mathbf{I}\otimes\mathbf{I})(\mathbf{F}^{\top}\mathbf{M}\mathbf{F})) = J^{-4/3}\,\text{tr}(\mathbf{I}\mathbf{F}^{\top}\mathbf{M}\mathbf{F})\,\mathbb{F}\,\mathbf{I} \\
&= J^{-4/3}\,\text{tr}(\mathbf{F}\mathbf{F}^{\top}\mathbf{M})\,\mathbf{F}\mathbf{F}^{\top} = J^{-4/3}\,\text{tr}(\mathbf{B}\mathbf{M})\,\mathbf{B} \qquad (5.81) \\
&= \text{tr}(\bar{\mathbf{B}}\mathbf{M})\,\bar{\mathbf{B}} = (\bar{\mathbf{B}}\otimes\bar{\mathbf{B}})\mathbf{M}\,,
\end{aligned}$$

$$\begin{aligned}
[\mathbb{F}\,(J^{-2/3}\,(\mathbf{I}\otimes\mathbf{C}^{-1} + \mathbf{C}^{-1}\otimes\mathbf{I}))\,\mathbb{F}^{\top}]\,\mathbf{M} &= J^{-2/3}\,\mathbb{F}\,[(\mathbf{I}\otimes\mathbf{C}^{-1})(\mathbf{F}^{\top}\mathbf{M}\mathbf{F}) \\
&\qquad\qquad + (\mathbf{C}^{-1}\otimes\mathbf{I})(\mathbf{F}^{\top}\mathbf{M}\mathbf{F})] \\
&= J^{-2/3}\,\text{tr}(\mathbf{C}^{-1}\mathbf{F}^{\top}\mathbf{M}\mathbf{F})\,\mathbb{F}\,\mathbf{I} + J^{-2/3}\,\text{tr}(\mathbf{I}\mathbf{F}^{\top}\mathbf{M}\mathbf{F})\,\mathbb{F}\,\mathbf{C}^{-1} \qquad (5.82) \\
&= J^{-2/3}\,\text{tr}(\mathbf{F}\mathbf{F}^{-1}\mathbf{F}^{-\top}\mathbf{F}^{\top}\mathbf{M})\,\mathbf{F}\mathbf{F}^{\top} + J^{-2/3}\,\text{tr}(\mathbf{F}\mathbf{F}^{\top}\mathbf{M})\,\mathbf{F}\mathbf{F}^{-1}\mathbf{F}^{-\top}\mathbf{F}^{\top} \\
&= \text{tr}(\mathbf{I}\mathbf{M})\,\bar{\mathbf{B}} + \text{tr}(\bar{\mathbf{B}}\mathbf{M})\,\mathbf{I} = (\bar{\mathbf{B}}\otimes\mathbf{I} + \mathbf{I}\otimes\bar{\mathbf{B}})\mathbf{M}\,,
\end{aligned}$$

[1] Tensor $\mathbb{F}$ could also be used to relate the Cauchy stress tensor $\boldsymbol{\sigma}$ to the second Piola-Kirchhoff stress tensor $\mathbf{S}$. In Sec. 5.5 the relation $\boldsymbol{\sigma} = J^{-1}\mathbf{F}\mathbf{S}\mathbf{F}^{\top}$ was given. The alternative form would be $\boldsymbol{\sigma} = J^{-1}\mathbb{F}\,\mathbf{S}$.

$$
\begin{aligned}
[\mathbb{F}\,(\mathbf{C}^{-1}\otimes\mathbf{C}^{-1})\,\mathbb{F}^{\top}]\,\mathbf{M} &= \mathbb{F}\,((\mathbf{C}^{-1}\otimes\mathbf{C}^{-1})(\mathbf{F}^{\top}\mathbf{M}\mathbf{F})) = \operatorname{tr}(\mathbf{C}^{-1}\mathbf{F}^{\top}\mathbf{M}\mathbf{F})\,\mathbb{F}\,\mathbf{C}^{-1}\\
&= \operatorname{tr}(\mathbf{F}\mathbf{F}^{-1}\mathbf{F}^{-\top}\mathbf{F}^{\top}\mathbf{M})\,\mathbf{F}\mathbf{F}^{-1}\mathbf{F}^{-\top}\mathbf{F}^{\top} = \operatorname{tr}(\mathbf{I}\mathbf{M})\,\mathbf{I}\\
&= (\mathbf{I}\otimes\mathbf{I})\mathbf{M}\,,
\end{aligned}
\tag{5.83}
$$

$$
\begin{aligned}
[\mathbb{F}\,(\mathbf{C}^{-1}\,\overline{\otimes}\,\mathbf{C}^{-1})\,\mathbb{F}^{\top}]\,\mathbf{M} &= \mathbb{F}\,((\mathbf{C}^{-1}\,\overline{\otimes}\,\mathbf{C}^{-1})(\mathbf{F}^{\top}\mathbf{M}\mathbf{F}))\\
&= \frac{1}{2}\,\mathbb{F}\,(\mathbf{C}^{-1}\mathbf{F}^{\top}\mathbf{M}\mathbf{F}\mathbf{C}^{-1} + \mathbf{C}^{-1}\mathbf{F}^{\top}\mathbf{M}^{\top}\mathbf{F}\mathbf{C}^{-1})\\
&= \frac{1}{2}\,(\mathbf{F}\mathbf{F}^{-1}\mathbf{F}^{-\top}\mathbf{F}^{\top}\mathbf{M}\mathbf{F}\mathbf{F}^{-1}\mathbf{F}^{-\top}\mathbf{F}^{\top} + \mathbf{F}\mathbf{F}^{-1}\mathbf{F}^{-\top}\mathbf{F}^{\top}\mathbf{M}^{\top}\mathbf{F}\mathbf{F}^{-1}\mathbf{F}^{-\top}\mathbf{F}^{\top})\\
&= \frac{1}{2}\,(\mathbf{I}\mathbf{M}\mathbf{I} + \mathbf{I}\mathbf{M}^{\top}\mathbf{I}) = (\mathbf{I}\,\overline{\otimes}\,\mathbf{I})\mathbf{M}\,,
\end{aligned}
\tag{5.84}
$$

$$
\begin{aligned}
[\mathbb{F}\,((\mathbf{f}\otimes\mathbf{f})\otimes(\mathbf{f}\otimes\mathbf{f}))\,\mathbb{F}^{\top}]\,\mathbf{M} &= \mathbb{F}\,[((\mathbf{f}\otimes\mathbf{f})\otimes(\mathbf{f}\otimes\mathbf{f}))(\mathbf{F}^{\top}\mathbf{M}\mathbf{F})]\\
&= \operatorname{tr}((\mathbf{f}\otimes\mathbf{f})\mathbf{F}^{\top}\mathbf{M}\mathbf{F})\,\mathbb{F}(\mathbf{f}\otimes\mathbf{f}) = \operatorname{tr}(\mathbf{F}(\mathbf{f}\otimes\mathbf{f})\mathbf{F}^{\top}\mathbf{M})\,(\mathbf{F}(\mathbf{f}\otimes\mathbf{f})\mathbf{F}^{\top})\\
&= \operatorname{tr}[((\mathbf{F}\mathbf{f})\otimes(\mathbf{F}\mathbf{f}))\mathbf{M}]\,(\mathbf{F}\mathbf{f})\otimes(\mathbf{F}\mathbf{f}) = [((\mathbf{F}\mathbf{f})\otimes(\mathbf{F}\mathbf{f}))\otimes((\mathbf{F}\mathbf{f})\otimes(\mathbf{F}\mathbf{f}))]\mathbf{M}\,,
\end{aligned}
\tag{5.85}
$$

$$
\begin{aligned}
&\det(\mathbf{C})\,\{\mathbb{F}\,[\mathbf{C}^{-1}\otimes(\mathbf{C}^{-1}(\mathbf{n}\otimes\mathbf{n})\mathbf{C}^{-1}) + (\mathbf{C}^{-1}(\mathbf{n}\otimes\mathbf{n})\mathbf{C}^{-1})\otimes\mathbf{C}^{-1}]\,\mathbb{F}^{\top}\}\,\mathbf{M}\\
&\quad= \det(\mathbf{C})\operatorname{tr}(\mathbf{C}^{-1}(\mathbf{n}\otimes\mathbf{n})\mathbf{C}^{-1}\mathbf{F}^{\top}\mathbf{M}\mathbf{F})\,\mathbf{F}\mathbf{C}^{-1}\mathbf{F}^{\top}\\
&\qquad\qquad + \det(\mathbf{C})\operatorname{tr}(\mathbf{C}^{-1}\mathbf{F}^{\top}\mathbf{M}\mathbf{F})\,\mathbf{F}\mathbf{C}^{-1}(\mathbf{n}\otimes\mathbf{n})\mathbf{C}^{-1}\mathbf{F}^{\top}\\
&\quad= \det(\mathbf{C})\operatorname{tr}(\mathbf{F}\mathbf{F}^{-1}\mathbf{F}^{-\top}(\mathbf{n}\otimes\mathbf{n})\mathbf{F}^{-1}\mathbf{F}^{-\top}\mathbf{F}^{\top}\mathbf{M})\,\mathbf{F}\mathbf{F}^{-1}\mathbf{F}^{-\top}\mathbf{F}^{\top}\\
&\qquad\qquad + \det(\mathbf{C})\operatorname{tr}(\mathbf{F}\mathbf{F}^{-1}\mathbf{F}^{-\top}\mathbf{F}^{\top}\mathbf{M})\,\mathbf{F}\mathbf{F}^{-1}\mathbf{F}^{-\top}(\mathbf{n}\otimes\mathbf{n})\mathbf{F}^{-1}\mathbf{F}^{-\top}\mathbf{F}^{\top}\\
&\quad= (\det(\mathbf{F}))^2\operatorname{tr}[((\mathbf{F}^{-\top}\mathbf{n})\otimes(\mathbf{F}^{-\top}\mathbf{n}))\mathbf{M}]\,\mathbf{I}\\
&\qquad\qquad + (\det(\mathbf{F}))^2\operatorname{tr}(\mathbf{I}\mathbf{M})\,(\mathbf{F}^{-\top}\mathbf{n})\otimes(\mathbf{F}^{-\top}\mathbf{n})\\
&\quad= [\,\mathbf{I}\otimes((\operatorname{cof}(\mathbf{F})\mathbf{n})\otimes(\operatorname{cof}(\mathbf{F})\mathbf{n})) + ((\operatorname{cof}(\mathbf{F})\mathbf{n})\otimes(\operatorname{cof}(\mathbf{F})\mathbf{n}))\otimes\mathbf{I}\,]\mathbf{M}\,,
\end{aligned}
\tag{5.86}
$$

$$
\begin{aligned}
&(\det(\mathbf{C}))^2\,\{\mathbb{F}\,[\,(\mathbf{C}^{-1}(\mathbf{n}\otimes\mathbf{n})\mathbf{C}^{-1})\otimes(\mathbf{C}^{-1}(\mathbf{n}\otimes\mathbf{n})\mathbf{C}^{-1})\,]\,\mathbb{F}^{\top}\}\,\mathbf{M}\\
&\quad= (\det(\mathbf{C}))^2\operatorname{tr}(\mathbf{C}^{-1}(\mathbf{n}\otimes\mathbf{n})\mathbf{C}^{-1}\mathbf{F}^{\top}\mathbf{M}\mathbf{F})\,\mathbf{F}\mathbf{C}^{-1}(\mathbf{n}\otimes\mathbf{n})\mathbf{C}^{-1}\mathbf{F}^{\top}\\
&\quad= (\det(\mathbf{C}))^2\operatorname{tr}(\mathbf{F}\mathbf{F}^{-1}\mathbf{F}^{-\top}(\mathbf{n}\otimes\mathbf{n})\mathbf{F}^{-1}\mathbf{F}^{-\top}\mathbf{F}^{\top}\mathbf{M})\,\mathbf{F}\mathbf{F}^{-1}\mathbf{F}^{-\top}(\mathbf{n}\otimes\mathbf{n})\mathbf{F}^{-1}\mathbf{F}^{-\top}\mathbf{F}^{\top}\\
&\quad= (\det(\mathbf{F}))^4\operatorname{tr}[((\mathbf{F}^{-\top}\mathbf{n})\otimes(\mathbf{F}^{-\top}\mathbf{n}))\mathbf{M}]\,(\mathbf{F}^{-\top}\mathbf{n})\otimes(\mathbf{F}^{-\top}\mathbf{n})\\
&\quad= [\,((\operatorname{cof}(\mathbf{F})\mathbf{n})\otimes(\operatorname{cof}(\mathbf{F})\mathbf{n}))\otimes((\operatorname{cof}(\mathbf{F})\mathbf{n})\otimes(\operatorname{cof}(\mathbf{F})\mathbf{n}))\,]\mathbf{M}\,,
\end{aligned}
\tag{5.87}
$$

$$
\begin{aligned}
&\det(\mathbf{C})\,\{\mathbb{F}\,[\mathbf{C}^{-1}\,\overline{\otimes}\,(\mathbf{C}^{-1}(\mathbf{n}\otimes\mathbf{n})\mathbf{C}^{-1}) + (\mathbf{C}^{-1}(\mathbf{n}\otimes\mathbf{n})\mathbf{C}^{-1})\,\overline{\otimes}\,\mathbf{C}^{-1}]\,\mathbb{F}^{\top}\}\,\mathbf{M}\\
&\quad= \det(\mathbf{C})\,\mathbf{F}\mathbf{C}^{-1}\mathbf{F}^{\top}\mathbf{M}\mathbf{F}\mathbf{C}^{-1}(\mathbf{n}\otimes\mathbf{n})\mathbf{C}^{-1}\mathbf{F}^{\top}\\
&\qquad\qquad + \det(\mathbf{C})\,\mathbf{F}\mathbf{C}^{-1}(\mathbf{n}\otimes\mathbf{n})\mathbf{C}^{-1}\mathbf{F}^{\top}\mathbf{M}^{\top}\mathbf{F}\mathbf{C}^{-1}\mathbf{F}^{\top}\\
&\qquad\qquad + \det(\mathbf{C})\,\mathbf{F}\mathbf{C}^{-1}(\mathbf{n}\otimes\mathbf{n})\mathbf{C}^{-1}\mathbf{F}^{\top}\mathbf{M}\mathbf{F}\mathbf{C}^{-1}\mathbf{F}^{\top}\\
&\qquad\qquad + \det(\mathbf{C})\,\mathbf{F}\mathbf{C}^{-1}\mathbf{F}^{\top}\mathbf{M}^{\top}\mathbf{F}\mathbf{C}^{-1}(\mathbf{n}\otimes\mathbf{n})\mathbf{C}^{-1}\mathbf{F}^{\top}\\
&\quad= (\det(\mathbf{F}))^2\,\mathbf{I}\mathbf{M}((\mathbf{F}^{\top}\mathbf{n}\otimes(\mathbf{F}^{\top}\mathbf{n})) + (\det(\mathbf{F}))^2\,((\mathbf{F}^{\top}\mathbf{n}\otimes(\mathbf{F}^{\top}\mathbf{n}))\mathbf{M}^{\top}\mathbf{I}\\
&\qquad + (\det(\mathbf{F}))^2\,((\mathbf{F}^{\top}\mathbf{n}\otimes(\mathbf{F}^{\top}\mathbf{n}))\mathbf{M}\mathbf{I} + (\det(\mathbf{F}))^2\,\mathbf{I}\mathbf{M}^{\top}((\mathbf{F}^{\top}\mathbf{n}\otimes(\mathbf{F}^{\top}\mathbf{n}))\\
&\quad= \mathbf{I}\mathbf{M}((\operatorname{cof}(\mathbf{F})\mathbf{n})\otimes(\operatorname{cof}(\mathbf{F})\mathbf{n})) + ((\operatorname{cof}(\mathbf{F})\mathbf{n})\otimes(\operatorname{cof}(\mathbf{F})\mathbf{n}))\mathbf{M}^{\top}\mathbf{I}\\
&\qquad + ((\operatorname{cof}(\mathbf{F})\mathbf{n})\otimes(\operatorname{cof}(\mathbf{F})\mathbf{n}))\mathbf{M}\mathbf{I} + \mathbf{I}\mathbf{M}^{\top}((\operatorname{cof}(\mathbf{F})\mathbf{n})\otimes(\operatorname{cof}(\mathbf{F})\mathbf{n}))\\
&\quad= [\,\mathbf{I}\,\overline{\otimes}\,((\operatorname{cof}(\mathbf{F})\mathbf{n})\otimes(\operatorname{cof}(\mathbf{F})\mathbf{n})) + ((\operatorname{cof}(\mathbf{F})\mathbf{n})\otimes(\operatorname{cof}(\mathbf{F})\mathbf{n}))\,\overline{\otimes}\,\mathbf{I}\,]\mathbf{M}\,.
\end{aligned}
\tag{5.88}
$$

Combining the results of equations (5.66)–(5.69), (5.81)–(5.83) and (5.85)–(5.87), we can arrive at the following expressions for the push-forwards of the fourth-order tensor products in (5.80):

$$\mathbb{F}\left(\nabla_{\mathbf{C}} J \otimes \nabla_{\mathbf{C}} J\right)\mathbb{F}^{\top} = \frac{1}{4} J^2 \mathbf{I} \otimes \mathbf{I}\,, \tag{5.89}$$

$$\mathbb{F}\left(\nabla_{\mathbf{C}} \bar{I}_1 \otimes \nabla_{\mathbf{C}} \bar{I}_1\right)\mathbb{F}^{\top} = \bar{\mathbf{B}} \otimes \bar{\mathbf{B}} - \frac{1}{3}\bar{I}_1(\bar{\mathbf{B}} \otimes \mathbf{I} + \mathbf{I} \otimes \bar{\mathbf{B}}) + \frac{1}{9}\bar{I}_1^2 \mathbf{I} \otimes \mathbf{I}\,, \tag{5.90}$$

$$\mathbb{F}\left(\nabla_{\mathbf{C}} I_4 \otimes \nabla_{\mathbf{C}} I_4\right)\mathbb{F}^{\top} = ((\mathbf{F}\mathbf{f}) \otimes (\mathbf{F}\mathbf{f})) \otimes ((\mathbf{F}\mathbf{f}) \otimes (\mathbf{F}\mathbf{f}))\,, \tag{5.91}$$

$$\begin{aligned}\mathbb{F}\left(\nabla_{\mathbf{C}} K_1 \otimes \nabla_{\mathbf{C}} K_1\right)\mathbb{F}^{\top} = {} & K_1^2 \mathbf{I} \otimes \mathbf{I} \\ & - K_1[\mathbf{I} \otimes ((\mathrm{cof}(\mathbf{F})\mathbf{n}) \otimes (\mathrm{cof}(\mathbf{F})\mathbf{n})) + ((\mathrm{cof}(\mathbf{F})\mathbf{n}) \otimes (\mathrm{cof}(\mathbf{F})\mathbf{n})) \otimes \mathbf{I}] \\ & + ((\mathrm{cof}(\mathbf{F})\mathbf{n}) \otimes (\mathrm{cof}(\mathbf{F})\mathbf{n})) \otimes ((\mathrm{cof}(\mathbf{F})\mathbf{n}) \otimes (\mathrm{cof}(\mathbf{F})\mathbf{n}))\,.\end{aligned} \tag{5.92}$$

Analogously, combining the results of equations (5.70)–(5.72), (5.77), (5.82)–(5.84), (5.86) and (5.88), we can obtain the following expressions for the push-forwards of the second gradients in (5.80):

$$\mathbb{F}\left(\nabla^{(2)}_{\mathbf{C}} J\right)\mathbb{F}^{\top} = \frac{1}{4} J(\mathbf{I} \otimes \mathbf{I} - 2\mathbf{I} \,\underline{\otimes}\, \mathbf{I})\,, \tag{5.93}$$

$$\mathbb{F}\left(\nabla^{(2)}_{\mathbf{C}} \bar{I}_1\right)\mathbb{F}^{\top} = -\frac{1}{3}(\bar{\mathbf{B}} \otimes \mathbf{I} + \mathbf{I} \otimes \bar{\mathbf{B}}) + \frac{1}{9}\bar{I}_1(\mathbf{I} \otimes \mathbf{I} + 3\mathbf{I} \,\underline{\otimes}\, \mathbf{I})\,, \tag{5.94}$$

$$\mathbb{F}\left(\nabla^{(2)}_{\mathbf{C}} I_4\right)\mathbb{F}^{\top} = \mathbf{0}\,, \tag{5.95}$$

$$\begin{aligned}\mathbb{F}\left(\nabla^{(2)}_{\mathbf{C}} K_1\right)\mathbb{F}^{\top} = {} & K_1(\mathbf{I} \otimes \mathbf{I} - \mathbf{I} \,\underline{\otimes}\, \mathbf{I}) \\ & - [\mathbf{I} \otimes ((\mathrm{cof}(\mathbf{F})\mathbf{n}) \otimes (\mathrm{cof}(\mathbf{F})\mathbf{n})) + ((\mathrm{cof}(\mathbf{F})\mathbf{n}) \otimes (\mathrm{cof}(\mathbf{F})\mathbf{n})) \otimes \mathbf{I}] \\ & + [\mathbf{I} \,\underline{\otimes}\, ((\mathrm{cof}(\mathbf{F})\mathbf{n}) \otimes (\mathrm{cof}(\mathbf{F})\mathbf{n})) + ((\mathrm{cof}(\mathbf{F})\mathbf{n}) \otimes (\mathrm{cof}(\mathbf{F})\mathbf{n})) \,\underline{\otimes}\, \mathbf{I}]\,.\end{aligned} \tag{5.96}$$

Finally, we can insert equations (5.89)–(5.96) into (5.80) and obtain the final form of the spatial elasticity tensor $\mathbb{c}$:

$$\begin{aligned}\mathbb{c} = 4J^{-1} \Bigg[& \Psi''_{\mathrm{iso}} \left(\bar{\mathbf{B}} \otimes \bar{\mathbf{B}} - \frac{1}{3}\bar{I}_1(\bar{\mathbf{B}} \otimes \mathbf{I} + \mathbf{I} \otimes \bar{\mathbf{B}}) + \frac{1}{9}\bar{I}_1^2 \mathbf{I} \otimes \mathbf{I}\right) \\ & + \Psi''_{\mathbf{f}}\,((\mathbf{F}\mathbf{f}) \otimes (\mathbf{F}\mathbf{f})) \otimes ((\mathbf{F}\mathbf{f}) \otimes (\mathbf{F}\mathbf{f})) \\ & + \Psi''_{\mathbf{fs}} \Big\{ K_1^2 \mathbf{I} \otimes \mathbf{I} - K_1[\mathbf{I} \otimes ((\mathrm{cof}(\mathbf{F})\mathbf{n}) \otimes (\mathrm{cof}(\mathbf{F})\mathbf{n})) + ((\mathrm{cof}(\mathbf{F})\mathbf{n}) \otimes (\mathrm{cof}(\mathbf{F})\mathbf{n})) \otimes \mathbf{I}] \\ & \quad + ((\mathrm{cof}(\mathbf{F})\mathbf{n}) \otimes (\mathrm{cof}(\mathbf{F})\mathbf{n})) \otimes ((\mathrm{cof}(\mathbf{F})\mathbf{n}) \otimes (\mathrm{cof}(\mathbf{F})\mathbf{n}))\Big\} \\ & + \Psi'_{\mathrm{iso}} \left(-\frac{1}{3}(\bar{\mathbf{B}} \otimes \mathbf{I} + \mathbf{I} \otimes \bar{\mathbf{B}}) + \frac{1}{9}\bar{I}_1(\mathbf{I} \otimes \mathbf{I} + 3\mathbf{I} \,\underline{\otimes}\, \mathbf{I})\right) \\ & + \Psi'_{\mathbf{fs}} \Big\{ K_1(\mathbf{I} \otimes \mathbf{I} - \mathbf{I} \,\underline{\otimes}\, \mathbf{I}) - [\mathbf{I} \otimes ((\mathrm{cof}(\mathbf{F})\mathbf{n}) \otimes (\mathrm{cof}(\mathbf{F})\mathbf{n})) + ((\mathrm{cof}(\mathbf{F})\mathbf{n}) \otimes (\mathrm{cof}(\mathbf{F})\mathbf{n})) \otimes \mathbf{I}] \\ & \quad + [\mathbf{I} \,\underline{\otimes}\, ((\mathrm{cof}(\mathbf{F})\mathbf{n}) \otimes (\mathrm{cof}(\mathbf{F})\mathbf{n})) + ((\mathrm{cof}(\mathbf{F})\mathbf{n}) \otimes (\mathrm{cof}(\mathbf{F})\mathbf{n})) \,\underline{\otimes}\, \mathbf{I}]\Big\}\Bigg] \\ & + \Psi'_{\mathrm{vol}}(\mathbf{I} \otimes \mathbf{I} - 2\mathbf{I} \,\underline{\otimes}\, \mathbf{I}) + \Psi''_{\mathrm{vol}} J \mathbf{I} \otimes \mathbf{I}\,.\end{aligned} \tag{5.97}$$

As mentioned in the beginning of this section, the material user subroutine `UserMat`, provided by the FE software Ansys APDL [83], requires the Jaumann tangent stiffness tensor $\mathbb{c}^J$ which is defined in terms of the spatial tensor $\mathbb{c}$. The components of this tensor with respect to the Cartesian basis can be calculated as [84]:

$$c^J_{ijkl} = c_{ijkl} + \frac{1}{2}(I_{ik}\sigma_{jl} + \sigma_{ik}I_{jl} + I_{il}\sigma_{jk} + \sigma_{il}I_{jk})\,, \tag{5.98}$$

where c^J_{ijkl}, c_{ijkl}, I_{ik} and σ_{jl} are the components of $\mathbb{c}^J$, $\mathbb{c}$, $\mathbf{I}$ and $\boldsymbol{\sigma}$, respectively.

5.8 Virtual configurations, constitutive equations for prestressed bodies

The strain-energy funtion Ψ_{alt} proposed in Sec. 5.4 must be associated with a reference configuration that is stress-free because the corresponding Cauchy stress tensor $\boldsymbol{\sigma}$, given by (5.58), is zero when no motion out of the reference configuration occurs. This can be easily checked by evaluating $\boldsymbol{\sigma}$ for $\mathbf{F} = \mathbf{I}$. However, the reference configuration Ω, used in this work, represents LV in its end-diastolic state and it can be clearly seen from the pressure tracing in Fig. 2 that at this moment of cardiac cycle there is already blood pressure of about 2.00 kPa inside the ventricle which means that the ventricular muscle is already stressed. The simple conclusion that can be draw from this fact is that Ψ_{alt} is not compatible with Ω; in fact, the same conclusion would apply to any other commonly used strain-energy function (in particular Ψ_{HO}) because zero-stress reference configuration is a standard requirement on strain-energy functions [72].

Suppose we choose $\mathbf{X} \in \Omega$ with preferred directions $\mathbf{f},\ \mathbf{s},\ \mathbf{n}$. If Ω was stress-free, then, for a given transplacement χ_t, it would be possible to calculate first the deformation gradient $\mathbf{F} = \nabla_{\mathbf{X}}(\chi_t)$ and subsequently the stress tensor $\boldsymbol{\sigma}$ at $\mathbf{x} = \chi_t(\mathbf{X})$. However, since $\mathbf{X}$ is in general prestressed, such calculation of stress would be incorrect even though the strain-energy function Ψ_{alt}, which determines $\boldsymbol{\sigma}$, has been shown to be able to reproduce experimental data very well (see Sec. 5.6). In order to obtain correct prediction of ventricular mechanics, it is necessary to formulate constitutive equation that explicitly includes the influence of initial prestress. An efficient method that can be used to obtain such constitutive equations was proposed by Johnson and Hoger [85, 86]. It is based on the concept of a virtual configuration of a point.

Let $\mathbf{X}$ be again a point in the reference configuration Ω. Johnson and Hoger [85, 86] proved that for each such point there exists a small (possibly infinitesimal) neighborhood $\mathcal{N}$ which can be mapped into a different local configuration, say $\widehat{\mathcal{N}}$, which is stress-free and which is called a *virtual configuration* of $\mathbf{X}$. The idea is illustrated in Fig. 24. The mapping χ_{p} which takes $\widehat{\mathcal{N}}$ onto $\mathcal{N}$ can be called a *virtual transplacement* and its inverse, χ_{p}^{-1}, is the aforementioned map which takes the neighborhood $\mathcal{N}$ to the stress-free state. The image of $\mathbf{X}$ in the virtual configuration is the point $\widehat{\mathbf{X}} \coloneqq \chi_{\text{p}}^{-1}(\mathbf{X})$. The gradient of χ_{p} at $\widehat{\mathbf{X}}$ is called the *prestrain gradient* [87] and it will be denoted by $\mathbf{F}_{\text{p}}$. The method proposed by Johnson and Hoger is based on the idea that if we want to describe the stress response at the image $\mathbf{x} = \chi_t(\mathbf{X})$ of a prestressed point $\mathbf{X}$ by means of a strain-energy function Ψ that satisfies the condition of a stress-free reference configuration, we can do so by associating Ψ with the local virtual configuration $\widehat{\mathcal{N}}$ rather than the reference configuration. In the case of our model Ψ_{alt}, this means we can still calculate $\boldsymbol{\sigma}$ and $\mathbb{c}$ according to equations (5.58) and (5.97), respectively, but we must replace all quantities in those equations which are related to the reference configuration by their counterparts related to the virtual configuration. In particular, $\mathbf{F}$ must be replaced by the total deformation gradient

$$\widehat{\mathbf{F}} \coloneqq \mathbf{F}\mathbf{F}_{\text{p}} \tag{5.99}$$

and the structural vectors $\mathbf{f}$ and $\mathbf{n}$ must be substituted by the unit vectors

$$\widehat{\mathbf{f}} \coloneqq \frac{\mathbf{F}_{\text{p}}^{-1}\mathbf{f}}{\|\mathbf{F}_{\text{p}}^{-1}\mathbf{f}\|} \qquad \text{and} \qquad \widehat{\mathbf{n}} \coloneqq \frac{\mathbf{F}_{\text{p}}^{\top}\mathbf{n}}{\|\mathbf{F}_{\text{p}}^{\top}\mathbf{n}\|}\,, \tag{5.100}$$

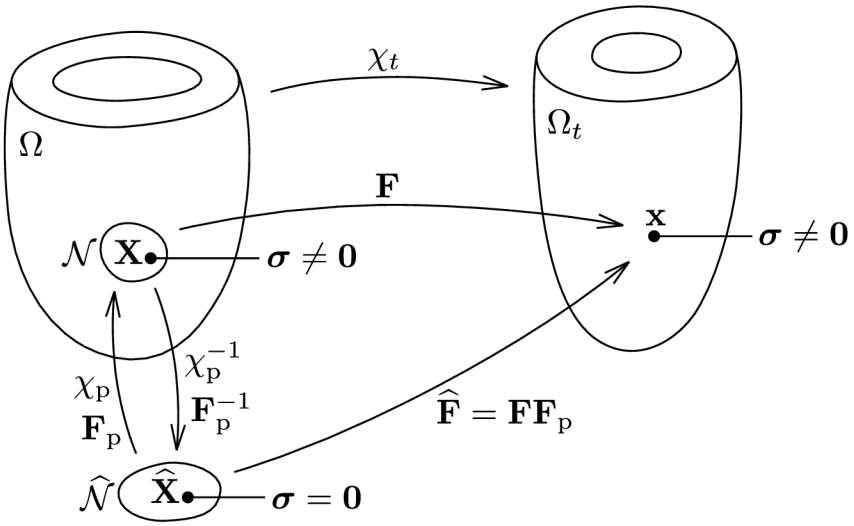

Fig. 24: An illustration showing the prestressed reference configuration Ω, the current configuration Ω_t and a stress-free virtual configuration $\widehat{\mathcal{N}}$ of a small neighborhood $\mathcal{N}$ of a point $\mathbf{X} \in \Omega$. According to Johnson and Hoger [85, 86], such virtual configuration exists for all points in Ω. See the text for the explanation of all quantities.

respectively. The expression (5.99) for the total deformation gradient allows the same geometrical interpretation as the polar decomposition of $\mathbf{F}$, which was illustrated in Fig. 20. This means that if $\mathbf{v}$ is a vector defined in the virtual configuration, the transformed vector $\widehat{\mathbf{F}}\mathbf{v}$ can be obtained by first sending $\mathbf{v}$ to the reference configuration by means of $\mathbf{F}_{\mathrm{p}}$ and then mapping the result, $\mathbf{F}_{\mathrm{p}}\mathbf{v}$, to the current configuration by means of $\mathbf{F}$, i.e:

$$\widehat{\mathbf{F}}\mathbf{v} = (\mathbf{F}\mathbf{F}_{\mathrm{p}})\mathbf{v} = \mathbf{F}(\mathbf{F}_{\mathrm{p}}\mathbf{v})\,. \tag{5.101}$$

Vectors $\widehat{\mathbf{f}}$ and $\widehat{\mathbf{n}}$ are defined by (5.100) because such definitions ensure that the deformed vectors $\mathbf{F}_{\mathrm{p}}\widehat{\mathbf{f}}$ and $\mathrm{cof}(\mathbf{F}_{\mathrm{p}})\widehat{\mathbf{n}}$, related to the reference configuration, will be aligned with the prescribed directions $\mathbf{f}$ and $\mathbf{n}$, respectively, as can be seen from the following results:

$$\mathbf{F}_{\mathrm{p}}\widehat{\mathbf{f}} = \|\mathbf{F}_{\mathrm{p}}^{-1}\mathbf{f}\|^{-1}\mathbf{F}_{\mathrm{p}}\mathbf{F}_{\mathrm{p}}^{-1}\mathbf{f} = \|\mathbf{F}_{\mathrm{p}}^{-1}\mathbf{f}\|^{-1}\mathbf{f}\,, \tag{5.102}$$

$$\mathrm{cof}(\mathbf{F}_{\mathrm{p}})\widehat{\mathbf{n}} = \det(\mathbf{F}_{\mathrm{p}})\|\mathbf{F}_{\mathrm{p}}^{\top}\mathbf{n}\|^{-1}\mathbf{F}_{\mathrm{p}}^{-\top}\mathbf{F}_{\mathrm{p}}^{\top}\mathbf{n} = \det(\mathbf{F}_{\mathrm{p}})\|\mathbf{F}_{\mathrm{p}}^{\top}\mathbf{n}\|^{-1}\mathbf{n}\,. \tag{5.103}$$

Thus the fibre and sheet-normal directions prescribed in the reference configuration will be preserved in the prestressed version of the model. The resulting vectors in (5.102) and (5.103) are not unit anymore but this is no longer required because $\boldsymbol{\sigma}$ and $\mathbb{c}$ are now formulated in terms of $\widehat{\mathbf{f}}$ and $\widehat{\mathbf{n}}$ (which are unit).

5.9 Calculation of prestrain gradients

In FE analyses, deformation gradients are calculated at all integration points of every element in mesh. Consequently, in order to obtain a prestressed reference configuration, it is necessary to provide the same number of prestrain gradients, one per each integration point. Both gradients are represented by 3×3 matrices whose entries are the components of the gradients with respect to the global Cartesian basis.

If no prestrain is applied (i.e. $\mathbf{F}_{\mathrm{p}} = \mathbf{I}$ everywhere), the application of end-diastolic pressure on the endocardial surface causes an unwanted inflation of the ventricular wall

and an increase in the cavity volume. For the model used in this work, such deformation for the applied end-diastolic pressure of 2 kPa (see Fig. 2) is displayed in Fig. 26A. Kinematic boundary conditions used in this simulation and in every other following in this chapter are shown in Fig. 25. It should be reiterated here that the FE model used in this chapter is based on the quadratic tetrahedral mesh shown in Fig. 13 of Sec. 4.7, with element coordinate systems defined by vectors $\mathbf{f}$, $\mathbf{s}$, $\mathbf{n}$ prescribed according to the algorithm described in Sec. 4.11. The material behavior is modeled by the strain-energy function Ψ_{alt} proposed in Sec. 5.4 with material parameters given in Table 5 of Sec. 5.6.

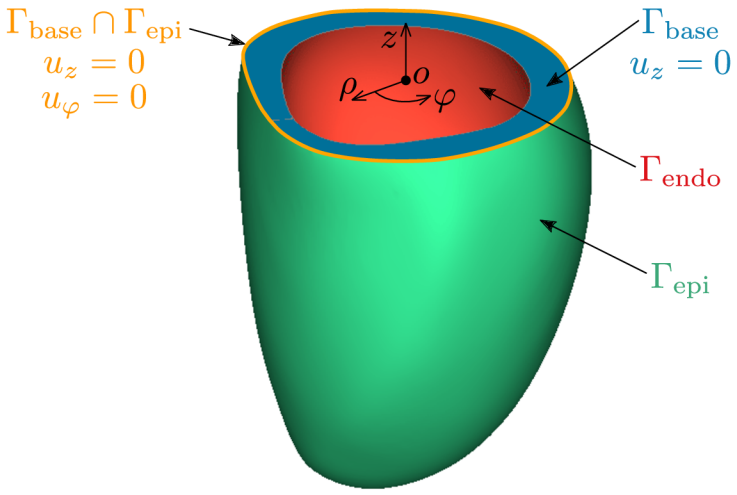

Fig. 25: Displacement boundary conditions on the basal surface Γ_{base} were prescribed in a cylindrical coordinate system (ρ, φ, z). The origin o of the system is situated at the intersection of the ventricular long axis with the basal plane and the z axis coincides with the long axis. For all nodes in Γ_{base}, the displacement u_z in z direction was set to zero. Additionally, zero displacement u_φ in the direction tangent to the φ coordinate was prescribed to all *corner* nodes (i.e. not to the nodes in the interior of the edges of elements) situated on the borderline between Γ_{base} and Γ_{epi} (orange contour in the figure). Thus the nodes on the borderline were allowed to move only in the radial direction ρ.

Although the displacement values shown in Fig. 26 may seem quite low, they caused an increase in the ventricular volume from approximately 137 ml to 200 ml, which is of course not permissible. In order to keep the shape and the volume of the ventricle approximately unchanged despite the acting endocardial pressure, it is necessary to find a suitable set of prestrain gradients that will reduce the nodal displacements to an acceptably low values. A general iterative algorithm for obtaining such prestrain field was proposed by Maas et al. [87]. This algorithm was employed here in the following way. First, it was necessary to provide starting values $\mathbf{F}_{\text{p}}^{(0)}$ of the prestrain gradient for all integration points. Since there is no reasonable non-trivial rule for such assignment, it was prescribed that $\mathbf{F}_{\text{p}}^{(0)} = \mathbf{I}$ in the whole model. Afterwards, pressure was applied on the endocardial surface and FE analysis was executed. The resulting expansion of the ventricle was described not only by calculated nodal displacements, but also by deformation gradients $\mathbf{F}^{(0)}$ calculated at each integration point. In Ansys APDL, these calculated gradients are made available inside the subroutine `UserMat` and the next step of the algorithm uses these gradients to formulate updated prestrain gradients $\mathbf{F}_{\text{p}}^{(1)} := \mathbf{F}^{(0)}\mathbf{F}_{\text{p}}^{(0)} = \mathbf{F}^{(0)}\mathbf{I} = \mathbf{F}^{(0)}$. This is the end of the initial (zeroth) iteration. In the next iteration, the whole process is repeated. The value

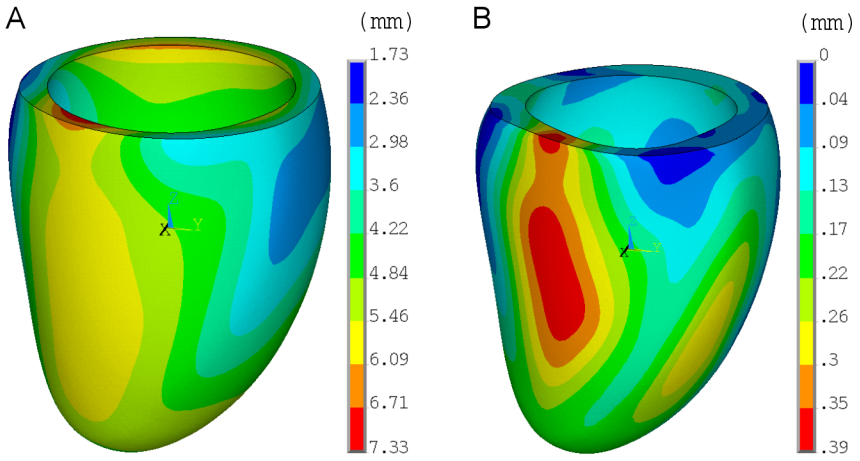

Fig. 26: (A) Total displacements resulting from the application of the end-diastolic pressure of 2 kPa on the endocardial surface of the model with no initial prestress. (B) Total displacements for the same presssure load when iteratively calculated prestrain gradients were applied. It can be seen that the maximum displacement in case B is below the chosen tolerance of 0.5 mm. The displacements are displayed in true scale and the viewing distance and viewing direction are the same for both cases.

of the applied pressure is unchanged but the gradients $\mathbf{F}_{\mathrm{p}}^{(1)}$ are now generally different from $\mathbf{I}$. These gradients act against the pressure load which means that, after the forces are balanced and a converged solution is obtained, the resulting displacements should be lower than in the previous iteration. In this way, the displacements can be iteratively decreased to an acceptable level. Generally, in the k-th iteration, $\mathbf{F}_{\mathrm{p}}^{(k)}$ is applied to each integration point and $\mathbf{F}^{(k)}$ is calculated in the subsequent FE solution. At the end of the iteration, maximum displacement is evaluated and compared with the chosen threshold, which in this work was 0.5 mm. If the maximum calculated displacement is higher than the threshold, the prestrain gradients are updated according to the rule $\mathbf{F}_{\mathrm{p}}^{(k+1)} := \mathbf{F}^{(k)}\mathbf{F}_{\mathrm{p}}^{(k)}$ and another iteration is started.

It should be realized that assignment of a prestrain gradient different from $\mathbf{I}$ to a given integration point is in fact equivalent to sending that point to a stress-free virtual configuration, as was illustrated in Fig. 24. Thus, the above described algorithm is based on the theory presented in the previous section. Also, it should be noted that the algorithm which was finally used in this work differed in one respect from that proposed by Maas et al. [87]. In the original algorithm, the loads are supposed to be applied at once and the prestrain gradients are calculated in a single iterative procedure. In the present case, such approach led to excessive distortion of elements and solution failure. For this reason, the pressure was applied incrementally and the iterative process described above had to be repeated after each increase.

In the final solution, the end-diastolic pressure was reached after 10 load steps. The pressure p applied in a given step was calculated as $p = (\mathrm{step}/10)^3 \cdot (2.0\ \mathrm{kPa})$ which means that it was increased very slowly at the beginning of analysis (because the constitutive model has very low initial stiffness and, consequently, a small increase of load causes large displacements) and as the solution proceeded, the increments gradually grew. The final displacement field at the end of the 10-th load step is shown in Fig. 26B. Additionally, Fig. 27A shows the distribution of the first principal stress in the prestressed configuration. In can be seen that there are some unrealistic stress concentrations at the base of the ventricle resulting from the imposed displacement boundary conditions. In order

to enable clearer visual comparison of stresses in the rest of the model (which are relevant), these concentrations were filtered in Fig. 27B by decreasing an upper bound of the contour legend to 0.050 MPa. This adjustment of the legend will be used also in some subsequent stress plots. It can be seen from Fig. 27B that highest calculated stresses are on the endocardial surface near the regions of the attachment of the right ventricular wall. However, since the forces exerted on the LV by the right ventricular myocardium were not taken into consideration (and nor was the blood pressure acting on the right side of the septum), it is debatable whether such locally increased stresses truly exist in real heart. More FE analyses with different boundary conditions should be carried out in the future in order to make definitive conclusions about the distribution of stress in these parts of the ventricle.

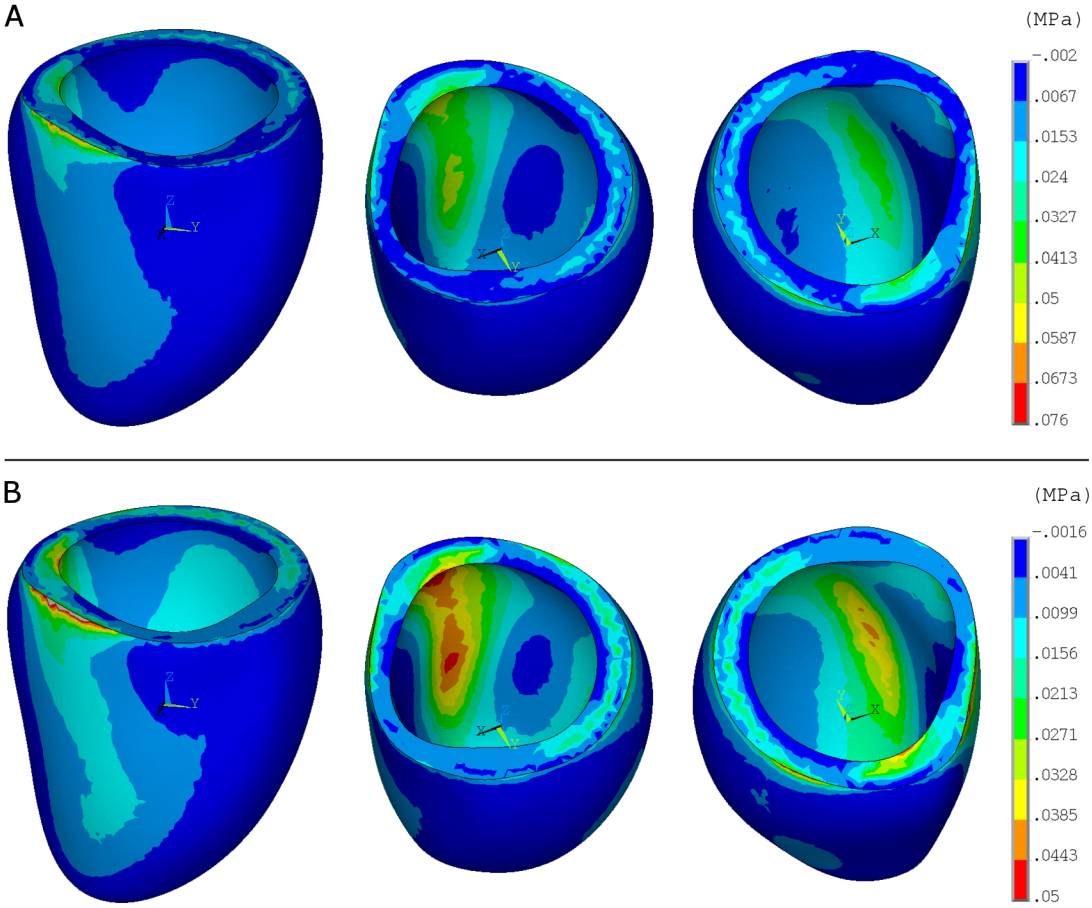

Fig. 27: (A) Calculated distribution of the first principal stress in the prestressed reference configuration (the same one that was shown in Fig. 26B). (B) The same stress field but with the upper bound of the contour legend decreased to 0.050 MPa. The intention is to filter the unrealistic stress concentrations near some nodes at the base with imposed displacement boundary conditions an to obtain better picture of the stress distribution in other parts of the model. Regions with stresses higher than 0.050 MPa are displayed in gray color (this is the case of only one small region in the leftmost figure of panel B).

5.10 Active strain approach for contractile tissues

In the continuum computational framework, a resting (i.e. non-contracting) myocyte can be represented by a small cylindrical neighborhood of a point in a reference configuration. (Alternatively, such neighborhood can also be viewed as a short section of a muscle fibre.) For our reference configuration Ω, such point $\mathbf{X}$ and its neighborhood $\mathcal{N}$ (magnified for illustrative purposes) are sketched in Fig. 28. Ventricular microstructure at $\mathbf{X}$ is characterized, as usual, by vectors $\mathbf{f}$, $\mathbf{s}$, $\mathbf{n}$. We can assume for simplicity that $\mathbf{X}$ is the centroid of the cylinder and that $\mathbf{f}$ coincides with its axis. Additionally, we will assume for a while that Ω is unloaded and stress-free.

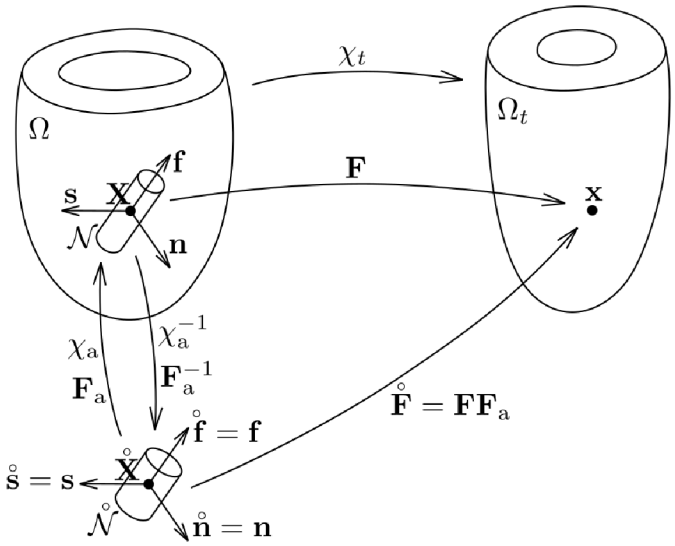

Fig. 28: A graphical representation of the active strain approach for modeling of muscle contraction. A cylindrical neighborhood $\mathcal{N}$ of a point $\mathbf{X}$ represents a myocyte (or a section of a muscle fibre) whose contraction generates stresses in the reference configuration Ω. The stress-free virtual configuration $\mathring{\mathcal{N}}$ represents unloaded contracted cell which is stretched by χ_a back into Ω. Active stresses can be included in constitutive equations by replacing the "standard" gradient $\mathbf{F}$ by $\mathring{\mathbf{F}}$ which is the composite of the active strain $\mathbf{F}_\mathrm{a}$ and $\mathbf{F}$. See the text for a full explanation.

Imagine now the "cell" $\mathcal{N}$ isolated from Ω so that it can freely deform without being restricted by its surroundings. If such cell contracts, its shape changes but the deformed (contracted) configuration, say $\mathring{\mathcal{N}}$, will be stress-free. However, if we forced such contracted cell back into its original shape $\mathcal{N}$, which could be regarded as an action of some local transplacement χ_a with the gradient $\mathbf{F}_\mathrm{a}$, then non-zero *active* stresses would be generated inside $\mathcal{N}$. The inverse local transplacement χ_a^{-1} (with the gradient $\mathbf{F}_\mathrm{a}^{-1}$), can be interpreted as a mapping that renders the neighborhood $\mathcal{N}$ stress-free. The value of χ_a^{-1} at $\mathbf{X}$ is $\mathring{\mathbf{X}}$.[1]

The above considerations suggest an efficient approach for modeling of active stresses generated by contractile muscle fibres. In the literature, it is usually called the *active strain approach* [88, 89] because it introduces the *active strain tensor* $\mathbf{F}_\mathrm{a}$ whose composition with

[1] Of course, if $\mathring{\mathcal{N}}$ is integrated back into Ω by means of χ_a, the resulting contact forces (tractions) acting on the boundary $\partial\mathcal{N}$ deform $\mathcal{N}$ (and its surroundings) into some other shape. But this is just a particular case of a "standard" deformation out of the reference configuration described by the transplacement χ_t and its gradient $\mathbf{F}$ (both shown in Fig. 28).

$\mathbf{F}$ defines the total deformation gradient

$$\mathring{\mathbf{F}} \coloneqq \mathbf{F}\mathbf{F}_{\mathrm{a}}\,. \tag{5.104}$$

The total gradient $\mathring{\mathbf{F}}$ can then be used in constitutive equations in place of the "standard" gradient $\mathbf{F}$ and the resulting response will thus include passive (elastic) as well as active stresses. It is obvious that this approach is based on the idea similar to that used in Sec. 5.8 to include the initial prestress. However, in contrast to the prestress gradient $\mathbf{F}_{\mathrm{p}}$, which had to be iteratively found, the active strain $\mathbf{F}_{\mathrm{a}}$ must be explicitly defined by its own constitutive equation [88]. A suitable form of such equation can be constructed using some basic facts about the deformation of a contracting cell. Boyett et al. [90] showed that when a cardiac myocyte freely contracts (i.e. without being subject to any axial loads or other constraints), it shortens and widens without significantly changing its volume. They also suggested that during contraction the width of the cell increases by the same proportion in different transverse directions. Under these conditions, it is natural to define the inverse gradient $\mathbf{F}_{\mathrm{a}}^{-1}$ by equation [88, 89]

$$\mathbf{F}_{\mathrm{a}}^{-1} \coloneqq \lambda\,\mathbf{f}\otimes\mathbf{f} + \frac{1}{\sqrt{\lambda}}\,(\mathbf{s}\otimes\mathbf{s} + \mathbf{n}\otimes\mathbf{n})\,. \tag{5.105}$$

The gradient of the form (5.105) describes transversely isotropic, isochoric deformation and it depends only on the stretch λ in the fibre direction. The inverse of $\mathbf{F}_{\mathrm{a}}^{-1}$ is $\mathbf{F}_{\mathrm{a}}$ which can be expressed from (5.105) as

$$\mathbf{F}_{\mathrm{a}} = \lambda^{-1}\,\mathbf{f}\otimes\mathbf{f} + \sqrt{\lambda}\,(\mathbf{s}\otimes\mathbf{s} + \mathbf{n}\otimes\mathbf{n})\,. \tag{5.106}$$

Although λ in (5.105) and (5.106) can generally be dependent on some other quantities, like action potential or some ionic currents [89], here it will be defined simply as a time-dependent function describing the evolution of stretch during an unloaded contraction. Such function can be constructed, e.g., from the results of Holubarsch et al. [91] who tested slim myocardial specimens with lengths of approximately 3.5–5.5 mm cut from human left ventricles. A time course of stretch of a typical specimen during its unloaded contraction is shown in Fig. 29. The curve in the figure can be used to obtain the value of λ for a particular time t measured from the beginning of contraction.

Since the strain-energy function Ψ_{alt} (Sec. 5.4) is defined in terms of $\mathbf{f}$ and $\mathbf{n}$, its modification for active materials entails not only the replacement of $\mathbf{F}$ by $\mathring{\mathbf{F}}$, but also transformation of $\mathbf{f}$ and $\mathbf{n}$ into their unit counterparts $\mathring{\mathbf{f}}$ and $\mathring{\mathbf{n}}$, respectively, defined in the stress-free configuration $\mathring{\mathcal{N}}$. This can be done by reutilizing equations (5.100) in which we only replace quantities introduced in Sec. 5.8 by the corresponding ones used in this section. If we also use the specific forms of $\mathbf{F}_{\mathrm{a}}$ and $\mathbf{F}_{\mathrm{a}}^{-1}$ given in (5.106) and (5.105), respectively, we obtain interesting results:

$$\mathring{\mathbf{f}} \coloneqq \frac{\mathbf{F}_{\mathrm{a}}^{-1}\mathbf{f}}{\|\mathbf{F}_{\mathrm{a}}^{-1}\mathbf{f}\|} = \frac{\lambda\mathbf{f}}{\|\lambda\mathbf{f}\|} = \frac{\lambda\mathbf{f}}{\lambda\|\mathbf{f}\|} = \mathbf{f}\,, \tag{5.107}$$

$$\mathring{\mathbf{n}} \coloneqq \frac{\mathbf{F}_{\mathrm{a}}^{\top}\mathbf{n}}{\|\mathbf{F}_{\mathrm{a}}^{\top}\mathbf{n}\|} = \frac{\sqrt{\lambda}\mathbf{n}}{\|\sqrt{\lambda}\mathbf{n}\|} = \frac{\sqrt{\lambda}\mathbf{n}}{\sqrt{\lambda}\|\mathbf{n}\|} = \mathbf{n} \tag{5.108}$$

(these results were already revealed above in Fig. 28). Thus the vectors $\mathbf{f}$ and $\mathbf{n}$ need not be modified in the expressions (5.58) and (5.97) for $\boldsymbol{\sigma}$ and $\mathbb{c}$, respectively, and it is only necessary to replace $\mathbf{F}$ by $\mathring{\mathbf{F}}$.

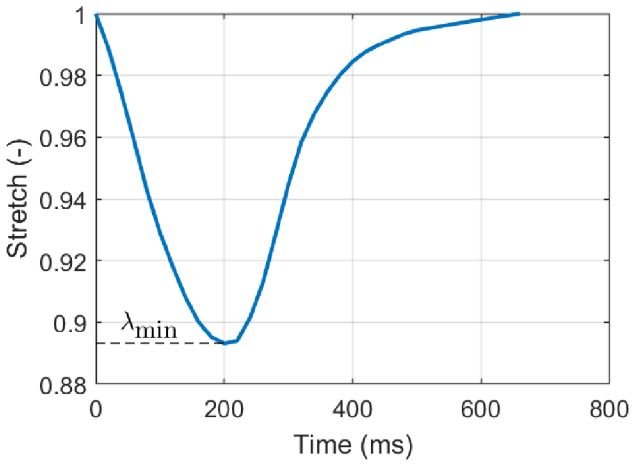

Fig. 29: An evolution of axial stretch λ during an unloaded contraction of a slim myocardial specimen cut from human left ventricle. The graph is based on Fig. 1B of [91]. Since the extent of shortening of the specimen is quite small, the curve had to be scaled in vertical direction before used in the FE model so as to achieve lower minimum stretch $\lambda_{\min}$ (i.e. increase the extent of shortening/increase the contractile force). More details will be given in Sec. 5.13.

5.11 Active materials with initial prestress

It is now time to combine the theory from sections (5.8)–(5.10); i.e. to consider bodies which are made up of active materials (capable of contracting) and, at the same time, are prestressed in their reference configuration. Obviously, this is exactly the case of the left ventricle when the chosen reference configuration represents the end-diastolic state. The value of the Cauchy stress tensor $\boldsymbol{\sigma}$ at a point of the ventricle at some time t is determined by the total deformation gradient $\overset{*}{\mathbf{F}}$ which is defined as the composition of the prestrain gradient $\mathbf{F}_{\mathrm{p}}$, the active strain $\mathbf{F}_{\mathrm{a}}$ and the standard gradient $\mathbf{F}$, i.e.:

$$\overset{*}{\mathbf{F}} := \mathbf{F}\mathbf{F}_{\mathrm{a}}\mathbf{F}_{\mathrm{p}}\,. \tag{5.109}$$

The order of gradients in the above definition implies that $\mathbf{F}_{\mathrm{p}}$ is applied first, followed by $\mathbf{F}_{\mathrm{a}}$, and finally the deformation from Ω to Ω_t is effected by $\mathbf{F}$. The sequence of mappings which take the stress-free local configuration $\widehat{\mathcal{N}}$ into the current configuration Ω_t is shown in Fig. 30. In the case of the FE model used in this chapter, $\mathbf{F}_{\mathrm{p}}$ is known for a given integration point and it is fixed in time. By contrast, $\mathbf{F}_{\mathrm{a}}$ changes with time and its current value must be calculated according to eq. (5.106). More details about the calculation of $\mathbf{F}_{\mathrm{a}}$ for a given integration point will be given in the next section. Referential unit vectors $\mathbf{f}$ and $\mathbf{n}$ must be mapped into the stress-free configuration $\widehat{\mathcal{N}}$. The transformation formulas are analogous to those in (5.100), (5.107) and (5.108); specifically:

$$\frac{(\mathbf{F}_{\mathrm{a}}\mathbf{F}_{\mathrm{p}})^{-1}\mathbf{f}}{\|(\mathbf{F}_{\mathrm{a}}\mathbf{F}_{\mathrm{p}})^{-1}\mathbf{f}\|} = \frac{\mathbf{F}_{\mathrm{p}}^{-1}\mathbf{F}_{\mathrm{a}}^{-1}\mathbf{f}}{\|\mathbf{F}_{\mathrm{p}}^{-1}\mathbf{F}_{\mathrm{a}}^{-1}\mathbf{f}\|} = \frac{\mathbf{F}_{\mathrm{p}}^{-1}(\lambda\mathbf{f})}{\|\mathbf{F}_{\mathrm{p}}^{-1}(\lambda\mathbf{f})\|} = \frac{\lambda\mathbf{F}_{\mathrm{p}}^{-1}\mathbf{f}}{\lambda\|\mathbf{F}_{\mathrm{p}}^{-1}\mathbf{f}\|} = \widehat{\mathbf{f}}\,, \tag{5.110}$$

$$\frac{(\mathbf{F}_{\mathrm{a}}\mathbf{F}_{\mathrm{p}})^{\top}\mathbf{n}}{\|(\mathbf{F}_{\mathrm{a}}\mathbf{F}_{\mathrm{p}})^{\top}\mathbf{n}\|} = \frac{\mathbf{F}_{\mathrm{p}}^{\top}\mathbf{F}_{\mathrm{a}}^{\top}\mathbf{n}}{\|\mathbf{F}_{\mathrm{p}}^{\top}\mathbf{F}_{\mathrm{a}}^{\top}\mathbf{n}\|} = \frac{\mathbf{F}_{\mathrm{p}}^{\top}(\sqrt{\lambda}\mathbf{n})}{\|\mathbf{F}_{\mathrm{p}}^{\top}(\sqrt{\lambda}\mathbf{n})\|} = \frac{\sqrt{\lambda}\mathbf{F}_{\mathrm{p}}^{\top}\mathbf{n}}{\sqrt{\lambda}\|\mathbf{F}_{\mathrm{p}}^{\top}\mathbf{n}\|} = \widehat{\mathbf{n}}\,. \tag{5.111}$$

Thus, as also indicated in Fig. 30, the transformed vectors are the vectors $\widehat{\mathbf{f}}$ and $\widehat{\mathbf{n}}$ defined in (5.100). With this result, we can conclude that in order to include the prestress as well

as the active stress into the constitutive model from Sec. 5.4, the Cauchy stress tensor (5.58) and the spatial elasticity tensor (5.97) must be expressed in terms of $\overset{*}{\mathbf{F}}$, $\widehat{\mathbf{f}}$ and $\widehat{\mathbf{n}}$ instead of $\mathbf{F}$, $\mathbf{f}$ and $\mathbf{n}$, respectively.

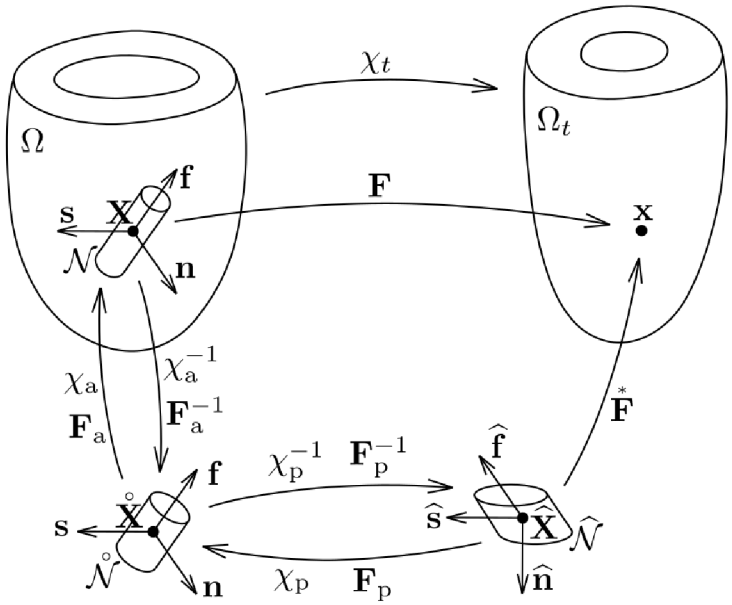

Fig. 30: A drawing showing all configurations, mappings and gradients involved in the constitutive description of a prestressed active material. $\widehat{\mathcal{N}}$ is a stress-free configuration. Prestress is applied by the prestrain gradient $\mathbf{F}_\mathrm{p}$ and active stresses at time t are generated by the active strain tensor $\mathbf{F}_\mathrm{a}$. Current configuration Ω_t represents equilibrated configuration at time t found by nonlinear FE solution. Deformation from the reference configuration Ω to Ω_t is characterized by the deformation gradient $\mathbf{F}$. All displayed vectors are of unit length. Vectors $\widehat{\mathbf{f}}$, $\widehat{\mathbf{s}}$, $\widehat{\mathbf{n}}$ are not necessarily orthogonal.

5.12 Calculation of mechanical activation maps

In Chapter 4, two simulations of electrical activation of LV were performed, one was the control simulation representing healthy conditions and the other represented a ventricle with the LBBB. The final outcome of these simulations were two electrical activation maps $\mathrm{eac_c}$ and $\mathrm{eac_b}$ respectively for control and LBBB conditions (see Sec. 4.14). Both these maps assign to each element K in the mesh $\mathcal{T}_h$ the calculated time of electrical activation at the centroid of the element. The maps should serve to distribute the onset of contraction throughout the mesh; however, the time of electrical activation is not the only determinant of the mechanical activation of myocytes. Experiments of Cordeiro et al. [92], conducted on isolated canine myocytes, showed that there is a latent period between the electrical activation and the onset of contraction and, most importantly, that the duration of this electromechanical delay considerably varies across the LV wall. Specifically, mean values measured in cells isolated from subendocardial, middle and subepicardial layers of myocardium were, respectively, 47 ms, 29 ms and 28 ms. The fact that the latency is shortest in epicardial cells, which generally depolarize later than the endocardial cells on the other side of the wall, suggests that this heterogeneity serves to synchronize contraction across the wall [92].

Since the reported differences between the electromechanical delays in endocardium and epicardium are significant, it was decided to take them into account in the FE model.

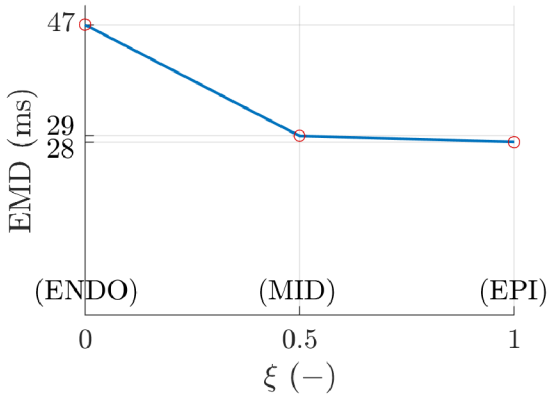

Fig. 31: Linear interpolation of the values (red circles) of electromechanical delay (EMD) reported by Cordeiro et al. [92] for myocytes from subendocardial (ENDO), middle (MID) and subepicardial (EPI) layer of myocardium. The data are plotted against a normalized transmural coordinate ξ (explained in the text).

To that end, the relative position of each point of the LV wall with respect to the endocardial and epicardial surfaces was assumed to be described by a normalized transmural coordinate ξ which takes the value 0 at the endocardium and the value 1 at the epicardium (regardless of the actual local wall thickness). Such coordinate was already assumed in Sec. 4.11 where the normalized distance ξ_K from the endocardial surface was defined for each element K by eq. (4.79). After the introduction of ξ, the mean values of electromechanical delay given above can be linearly interpolated over the interval $\langle 0, 1\rangle$, which is shown in Fig. 31. Since we know from Sec. 4.11 the value ξ_K of the coordinate ξ for each element K, we can define a function

$$\mathrm{emd}\colon \mathcal{T}_h \to \mathbb{R} \tag{5.112}$$

which assigns to each $K \in \mathcal{T}_h$ the value of the electromechanical delay according to the graph in Fig. 31. The function is defined by:

$$\mathrm{emd}(K) \coloneqq \begin{cases} (29-47)2\,\xi_K + 47 & \text{if} \quad \xi_K \in \langle 0, 0.5\rangle \\ (28-29)(2\,\xi_K - 1) + 29 & \text{if} \quad \xi_K \in (0.5, 1\rangle\,. \end{cases} \tag{5.113}$$

Mechanical activation maps, specifying the times of the onset of contraction for all $K \in \mathcal{T}_h$, can then be defined as two functions $\mathrm{mac_c}$ and $\mathrm{mac_b}$ of the form (5.112) whose values are given by:

$$\mathrm{mac_c}(K) \coloneqq \mathrm{eac_c}(K) + \mathrm{emd}(K)\,, \tag{5.114}$$

$$\mathrm{mac_b}(K) \coloneqq \mathrm{eac_b}(K) + 10 + \mathrm{emd}(K)\,. \tag{5.115}$$

The summand 10 in the definition 5.115 reflects the finding of Durrer et al. [25] that electrical activation of the right ventricle starts approximately 10 ms later then the activation of the left ventricle (cf. Sec. 2.4). In the LBBB the right ventricular conduction system is a source of activation not only for the right ventricle but also for the left ventricle. The delay of 10 ms should be included in the definition of $\mathrm{mac_b}$ because then both simulations will use the same origin of time (i.e. $t = 0$ ms will denote the same instant within the cardiac cycle in both cases). This will later enable, e.g., to plot pressure curves calculated for control and LBBB conditions in one graph with the horizontal time axis having an unambiguous meaning.

5.13 Modeling of ventricular pressure and volume

One of the main goals of this thesis is to calculate the evolution of ventricular pressure and volume under healthy conditions and in the presence of the LBBB. This section provides details about the two simulations from which these results were obtained.

At the beginning of both simulations, the corresponding prestrain gradient field was applied on the mesh against the end-diastolic pressure of 2 kPa acting on the endocardial surface. As mentioned before, the prestrain gradients $\mathbf{F}_{\mathrm{p}}$ were constant during the simulations for all intergation points. After the application of prestress, no pressure or volume changes occurred until first elements became mechanically activated. This happened approximately at $t = 35$ ms in the control simulation and $t = 38$ ms in the LBBB simulation; these times correspond to the lowest values assigned by functions $\mathrm{mac_c}$ and $\mathrm{mac_b}$, respectively. It should be emphasized that these functions represented the only difference between both simulations; all other parameters controlling the evolution of pressure and volume were common to both of them.

After a particular element K was mechanically activated, the value of the active strain tensor $\mathbf{F}_{\mathrm{a}}$ for its four integration points (the same value for all) was calculated at each load step from eq. (5.106). As mentioned before, parameter λ in this equation can be determined from the stretch curve in Fig. 29. Specifically, let t_k be a time at the end of the k-th load step and let $K \in \mathcal{T}$ be such that $\mathrm{mac_c}(K) < t_k$ (or, analogously, $\mathrm{mac_b}(K) < t_k$). Then the value of λ for this element and load step can be read from the vertical axis in Fig. 2 as the value corresponding to the horizontal coordinate Time $= t_k - \mathrm{mac_c}(K)$. However, it must be noted that it was not exactly the curve in Fig. 29 that was finally used to calculate λ in the simulations presented in this section. As already indicated in the caption to the figure, testing simulations revealed that the contraction displayed in the figure is too weak to generate blood pressures as high as 16 kPa (systolic pressure, see Sec. 2.2). For this reason, the curve had to be scaled in the vertical direction to achieve lower minimum value λ_{min}. The final value of this parameter used in the simulations was as low as $\lambda_{\mathrm{min}} = 0.74$, which corresponds to a 26% shortening. Although this value considerably differs from the experimental minimum shown in Fig. 29 (less than 11% shortening), it must be mentioned that in the paper [91], from which the data in Fig. 29 were extracted, the authors themselves admitted that contraction of their specimens was abnormally weak. In particular, the peak force developed during *isometric* contraction was considerably smaller compared to other studies. Anyway, full explanation of this discrepancy between the model and experiments surely requires further study.

When contraction in each simulation began, time step was decreased in order to capture the subsequent pressure and volume changes with sufficient accuracy. More precisely, time increments in the subsequent load steps varied between 0.1 ms and 10 ms. They were not constant because individual phases of cardiac cycle exhibit different character of pressure and volume changes which should be reflected in the chosen time increments. Time step was also decreased near the end of each phase in order to terminate each phase at the right time. Specifically, the shortest time step of 0.1 ms was prescribed just before the end of the isovolumic contraction because at this point of cardiac cycle the pressure growth is very rapid which means that even a moderate time increment results in a huge pressure increase. If the diastolic pressure was overly exceeded in the last step of the isovolumic contraction, parameters and equations prepared for the simulation of the subsequent ejection phase would be activated too late which would affect the shape of the calculated pressure waveform. The longest time step of 10 ms was used in the central part of the filling phase which did not require any special treatment.

Suppose now that t_k is a time within the isovolumic contraction period which specifies the end of the k-th load step. Active strain field $\mathbf{F}_\mathrm{a} \neq \mathbf{I}$ at t_k can be calculated relatively easily using the algorithm described above. However, if such active strain was applied against the initial end-diastolic pressure of 2 kPa, it is clear that the ventricle would shrink and its volume would decrease. Of course, substantial volume change is not permissible during the isovolumic contraction phase which means that unless $\mathbf{F}_\mathrm{a}$ is almost equal to $\mathbf{I}$, the endocardial pressure p_k must be increased so that the resulting ventricular volume V_k at t_k is approximately equal to the end-diastolic volume. A suitable value of p_k must be found iteratively. In this work, the first guess was calculated as

$$p_k^1 \coloneqq p_{k-1} + \dot{p}_k^1 \, (t_k - t_{k-1}) \,, \tag{5.116}$$

where

$$\dot{p}_k^1 \coloneqq \frac{p_{k-1} - p_{k-2}}{t_{k-1} - t_{k-2}} \,. \tag{5.117}$$

After a FE solution with applied pressure p_k^1 was executed, volume V_k^1 of the deformed LV cavity was calculated together with the rate of change of volume $\dot{V}_k^1 \coloneqq (V_k^1 - V_{k-1})/(t_k - t_{k-1})$. The volume rate should ideally be zero during isovolumic contraction, but since some error must be tolerated, the calculated volume rate was compared against the criterion $|\dot{V}_k^1 - \dot{V}_\mathrm{target}| < 10^{-3}$ ml $\cdot$ ms^{-1}, where the target value $\dot{V}_\mathrm{target} \coloneqq 0$ ml $\cdot$ ms^{-1}. If the criterion was not satisfied, the second estimate for the pressure rate was calculated as $\dot{p}_k^2 \coloneqq \dot{p}_k^1 + \mu \, (\dot{V}_k^1 - \dot{V}_\mathrm{target})$, where $\mu < 0$ is a suitably chosen penalty parameter. The next applied pressure was then $p_k^2 \coloneqq p_{k-1} + \dot{p}_k^2 \, (t_k - t_{k-1})$. The resulting volume was denoted V_k^2 and the volume rate $\dot{V}_k^2 \coloneqq (V_k^2 - V_{k-1})/(t_k - t_{k-1})$ was checked against the convergence criterion $|\dot{V}_k^2 - \dot{V}_\mathrm{target}| < 10^{-3}$ ml $\cdot$ ms^{-1}. In general, in the r-th iteration, for $r > 1$, the algorithm first calculated the pressure rate

$$\dot{p}_k^r \coloneqq \dot{p}_k^{r-1} + \mu \, (\dot{V}_k^{r-1} - \dot{V}_\mathrm{target}) \tag{5.118}$$

and then the next estimate of pressure

$$p_k^r \coloneqq p_{k-1} + \dot{p}_k^r \, (t_k - t_{k-1}) \,. \tag{5.119}$$

Volume V_k^r was obtained from the FE solution and the volume rate

$$\dot{V}_k^r \coloneqq \frac{V_k^r - V_{k-1}}{t_k - t_{k-1}} \tag{5.120}$$

was checked against the criterion

$$|\dot{V}_k^r - \dot{V}_\mathrm{target}| < 10^{-3} \text{ ml} \cdot \text{ms}^{-1} \,. \tag{5.121}$$

Although there is no subscript or superscript attached to μ in (5.118), its value was updated multiple times during simulations in order to improve convergence rate. The assigned values ranged from -1.6 kPa $\cdot$ ml^{-1} to -0.4 kPa $\cdot$ ml^{-1}.

When the pressure p exceeded the diastolic pressure of 10.7 kPa, the isovolumic contraction phase was terminated and the solution process entered the ejection phase. During this phase, equations (5.116)–(5.120) and criterion (5.121) continued to be used without any change. However, since the ventricular volume decreases during ejection, it was necessary to redefine $\dot{V}_\mathrm{target}$. A new definition was provided by the two-element Windkessel model [93] which relates aortic pressure, pressure rate and inflow of blood into aorta in

terms of arterial compliance C_w and total peripheral resistance R_w. If the inflow into aorta is replaced by the rate of change of ventricular volume, it is possible to define:

$$\dot{V}^r_\mathrm{target} \coloneqq -C_\mathrm{w}\dot{p}^r_k - \frac{p^r_k}{R_\mathrm{w}}\,. \tag{5.122}$$

Parameters C_w and R_w were tuned to give a realistic pressure–volume response. Final values used in both simulations were $C_\mathrm{w} \coloneqq 4.2\ \mathrm{ml}\cdot\mathrm{kPa}^{-1}$ and $R_\mathrm{w} \coloneqq 34\ \mathrm{kPa}\cdot\mathrm{ms}\cdot\mathrm{ml}^{-1}$. Generally, in r-th iteration ($r \geq 1$) of the k-th load step, the pressure rate $\dot{p}^r_k$ was first calculated using either (5.117) or (5.118). Afterwards, p^r_k was obtained either from (5.116) or from (5.119). Then the FE solution was executed which provided the volume V^r_k of the deformed chamber. Finally, volume rate $\dot{V}^r_k$ and its target value $\dot{V}^r_\mathrm{target}$ were calculated using (5.120) and (5.122), respectively, and both values were compared by means of the convergence criterion (5.121). When the criterion was satisfied, p^r_k and V^r_k were denoted as p_k and V_k, respectively, and these values were saved as results of the k-th load step. Ejection phase was terminated when the final volume rate $\dot{V}^r_k$ (calculated from the converged solution V_k) was greater than 0 which indicated reversed blood flow.

Isovolumic relaxation phase was modeled in exactly the same way as the isovolumic contraction phase with $\dot{V}_\mathrm{target} \coloneqq 0\ \mathrm{ml}\cdot\mathrm{ms}^{-1}$. When p_k decreased below 1.8 kPa (left atrial pressure at the end of isovolumic relaxation, see Fig. 2), isovolumic relaxation was finished and solution continued with the phase of ventricular filling. Since the results from this last phase are not crucial for this work, it was modeled in a very simple manner by assuming a linear increase of pressure back to its end-diastolic value of 2 kPa. This was motivated by the works of Eriksson et al. [75, 94] in which the same approach was used. The rate of pressure increase during the ventricular filling was adjusted to produce approximately 850 ms long cardiac cycle, which can be considered a normal resting value.

The resulting pressure and volume waveforms obtained from the simulations are compared in Fig. 32. It can be seen that LBBB decreases the rate of LV pressure rise during early isovolumic contraction. The pressure starts visibly rising approximately after 45 ms in the control simulation and about 10 ms later in the simulation of LBBB. However, at the end of isovolumic contraction the simulation of LBBB is delayed by more than 40 ms with respect to the control simulation, which is reflected by a prolonged IVC duration of 92 ms in LBBB compared to 50 ms duration under control conditions. These values correspond with clinically observed values (mean ± SD) 38±9 ms and 96±35 ms reported by Özdemir et al. [33] respectively for a group of 65 healthy subjects and a group of 45 patients with isolated LBBB. On the other hand, the pressure rise during IVC produced by the model is approximately exponential which is not in agreement with clinical measurements which show that the growth is much more straight. Consequently, the maximum rate of pressure rise at the end of IVC is 715 $\mathrm{Pa}\cdot\mathrm{ms}^{-1}$ in the control simulation, while normal values for an untrained person are only about 180–250 $\mathrm{Pa}\cdot\mathrm{ms}^{-1}$ [95]. What is interesting is that similar unrealistic exponential growth can be seen also in the results of other authors [40, 47] who also combined the active strain approach with an exponential strain-energy function. Since these authors used different, and more sophisticated, algorithm for calculation of active fibre stretch λ, it seems that this inconsistency is indeed a consequence of the above mentioned combination. This sets another potential direction for future investigations.

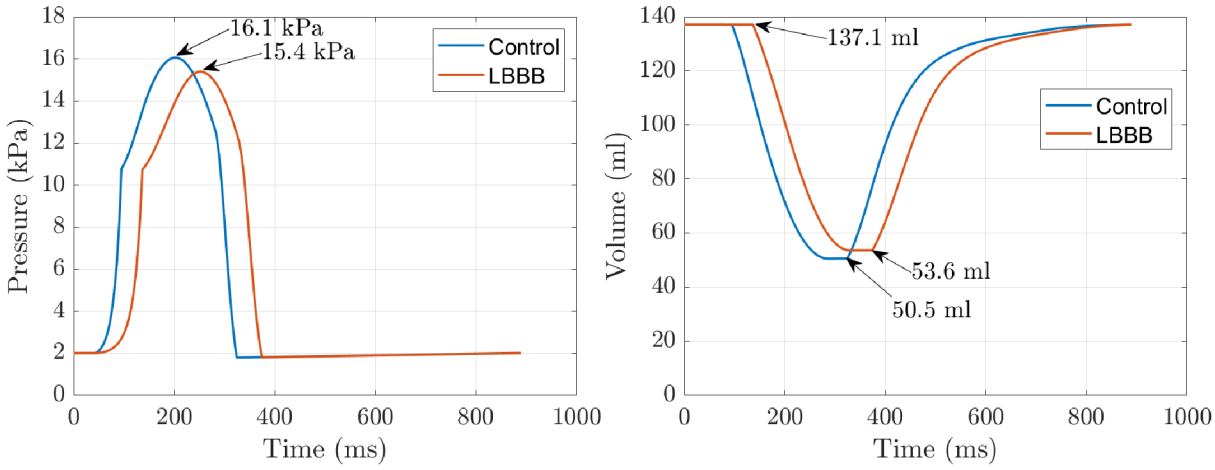

Fig. 32: Calculated pressures and volumes representing a healthy ventricle (Control) and a ventricle with the left bundle branch block (LBBB). During the first 10 ms of simulations, the prestress of 2 kPa was applied in small increments as described above in Sec. 5.9; this was reflected by small oscillations of volume around the end-diastolic value. These initial (unrealistic) parts of the curves were replaced by horizontal lines in the above graphs.

In the ejection phase, the model predicted a decrease of systolic pressure by ∼4.4 % due to the LBBB (see Fig. 32). For comparison, a clinical study of Aalen et al. [36] reported a decrease by ∼1.5 %. The duration of ejection period was approximately 190 ms in both simulations which is shorter than normal values 260–300 ms [4, 5]. The length of ejection could be adjusted to some extent by tuning the parameters C_{w} and R_{w} of the Windkessel model, but it was not possible to obtain values close to the normal ones. Again, the same deficiency can be seen in the results of the above mentioned studies [40, 47] whose authors also used the two-parametric Windkessel model and obtained ejection times of approximately 160 ms [40] and 190 ms [47]. Thus it seems that this shortcoming is an inherent feature of the Windkessel model.

The most important result with regard to the topic of this thesis is the graph on the right of Fig. 32 which shows temporal evolution of the LV volume in both simulations. From the values of end-diastolic and end-systolic volumes shown in the figure, we can calculate that ejection fraction in control simulation was 63.2 % and it decreased by 2.3 % to 60.9 % in the simulation of LBBB. Thus, ejection fraction remained in the range of normal values ($\geq$ 50 % [4]) after induction of the LBBB which confirms conclusions and claims of many authors (e.g. [26, 33, 36]) but contradicts, e.g., the findings of Valenti et al. [34] who observed a decrease in mean ejection fraction by 14.2 % to 48.9 %. Although the calculated decrease by 2.3 % is lower than the drops reported by all studies mentioned in Fig. 10 and Table 1 of Chapter 3, it is very close to the results of Özdemir et al. [33] and Aalen et al. [36] who observed 4% decrease in mean ejection fraction. The first of these studies also reported similar values of IVC durations, as already mentioned above.

The results from Fig. 32 were used to construct the pressure-volume diagrams shown in Fig. 33. In order to compare the diagrams with a real one, the figure contains also a diagram obtained from the curves in Fig. 2.

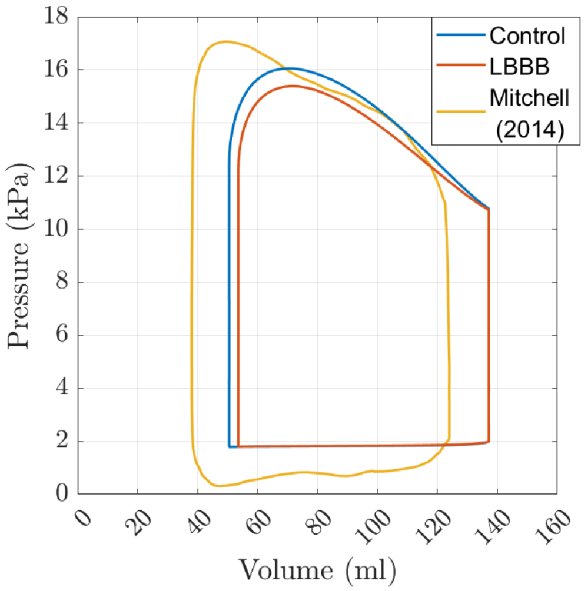

Fig. 33: Calculated pressure-volume diagrams representing a healthy ventricle (Control) and a ventricle with the left bundle branch block (LBBB). The diagrams are compared with a real one constructed from the left ventricular pressure and volume waveforms shown in Fig. 2, which were extracted from Fig. 1 of the paper by Mitchell and Wang (2014) [2].

5.14 Analysis of motions, strains and stresses

In Chapter 3, it was mentioned that asynchronous activation due to the LBBB necessarily leads to mechanical dyssynchrony which is demonstrated by the so-called "apical rocking" which refers to increased displacements of the LV apex perpendicular to the LV long axis [28, 29]. These changes are captured also by the FE model as demonstrated in Fig. 34 which shows, for both simulations, a trajectory of the lowest apical node of the model projected on the global xy plane (perpendicular to the long axis). It can be seen that in the simulation of the LBBB the motion of apex is altered and displacements are increased, especially in the y direction. In order to obtain a better idea of the motions of the model during the whole cardiac cycle, refer to the electronic appendix of the thesis which contains animations of the motion for both simulated conditions.

The impact of LBBB on the timing of contraction in different parts of the ventricle is demonstrated in Fig. 35. The figure shows calculated time courses of circumferential and longitudinal strains taken from the central part of the right septal surface and from the opposite area on the epicardial surface of the lateral wall of the ventricle. It can be seen that the time shift between strains in the septum and those in the lateral wall is considerably larger in LBBB which means that the two regions are clearly out of phase with each other. Also, there is more pronounced stretching of the lateral wall during early systole in the LBBB case, which is a consequence of the delayed activation of the wall. These findings agree with magnetic resonance-based strain measurements in dogs with induced LBBB [96].

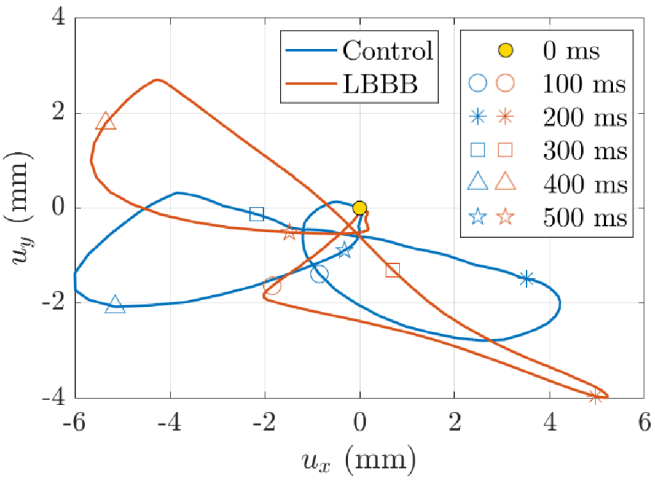

Fig. 34: Displacements u_x and u_y (corresponding to the global x and y directions) of the lowest apical node in the FE model during the whole cardiac cycle. Results are shown for a healthy ventricle (Control) and for a ventricle with the left bundle branch block (LBBB). Markers denote selected times within the cardiac cycle (values correspond to the timeline in Fig. 32).

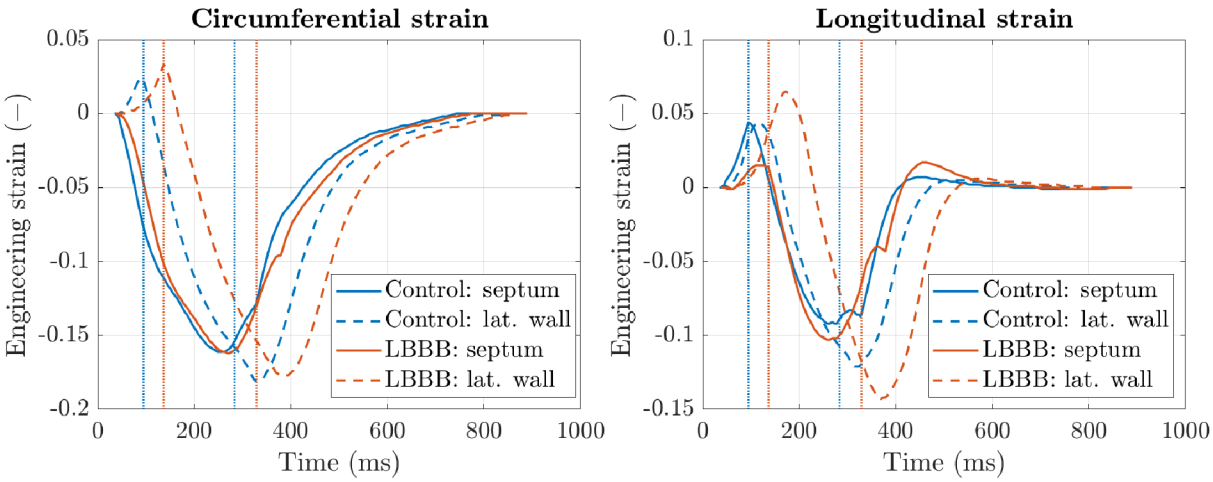

Fig. 35: Temporal evolution of circumferential and longitudinal strains in the central part of the right septal surface and in the site across the diameter of the ventricle on the epicardial surface of the lateral wall. Results are shown for a healthy ventricle (Control) and for a ventricle with the left bundle branch block (LBBB). Vertical lines mark the beginning and the end of ejection phase for each simulation. Timeline is the same as in Fig. 32.

The last quantity that should be analyzed in this work, according to the goals specified in Chapter 3, is wall stress. Stresses at the end of diastole were already discussed in Sec. 5.9. In the present section, another three characteristic stages of the cardiac cycle will be analyzed with respect to wall stress, namely: the beginning of ejection, the moment when the LV pressure reaches its peak, and the end of ejection. The distributions of the first principal stress at these three stages for both simulated conditions are displayed in Figs. 36, 37 and 38, respectively. Just like in Sec. 5.9, unrealistic stress concentrations near the base were excluded from the plots by restricting the intervals of the contour legends.

At the beginning of ejection (Fig. 36), the stress distribution is almost uniform in the anterior, lateral and posterior regions of the ventricle, especially on the epicardial surface. But this uniformity is totally disrupted in the septum where much higher stresses are concentrated in a narrow band running obliquely across the right septal surface from the base toward the apex. These concentrations are more pronounced in the LBBB simulation which is probably because ejection is delayed in this case which means that the early-activated septum has more time to increase the active stresses. However, as pointed out in Sec. 5.9, accuracy of stresses calculated in the septum and adjacent regions is somewhat questionable because this study neglected the forces exerted on the septum by the contracting right ventricle.

The moment of peak LV pressure (Fig. 37) is characterized by "banded" stress distribution which is obviously largely dependent on the prescribed fibre directions. Stress values in the anterior, lateral and posterior regions of the ventricle are less uniform then in the previous case. On the right septal surface there is again the band with concentrated high stresses, but this time the stress values are comparable for both simulations.

The dependence on the fibre directions can be recognized also in the stress field at the end of ejection (Fig. 38). Substantially increased septal stresses at this moment can be seen only in the control simulation; in the model with the LBBB, the septum is already relaxing and so the stresses are reduced.

It should be noted that the calculated stresses shown in the figures are generally far higher than those for which the hyperelastic model was calibrated. Therefore, it is doubtful whether the predicted responses, calculated for strains that are very far from available experimental data, are reliable. Unfortunately, this is an inherent disadvantage of the active strain approach in which a single (total) stress tensor is derived from a particular strain-energy function which, however, is never designed to reproduce the active stresses. This disadvantage can be eliminated by using an alternative *active stress approach* [88, 89] for modeling of contractile tissues. This approach introduces the active stress tensor (instead of the active strain tensor $\mathbf{F}_{\mathrm{a}}$) and defines the total stress as the sum of the passive tensor and the active tensor. The passive part is determined from a strain-energy function while the active part is defined by its own constitutive equation. The active stress approach was, in fact, the first choice for this thesis, but the implemented algorithm suffered from severe convergence difficulties during the ejection phase that could not be overcome. For this reason, the active strain formulation was eventually used which turned out to be numerically more stable.

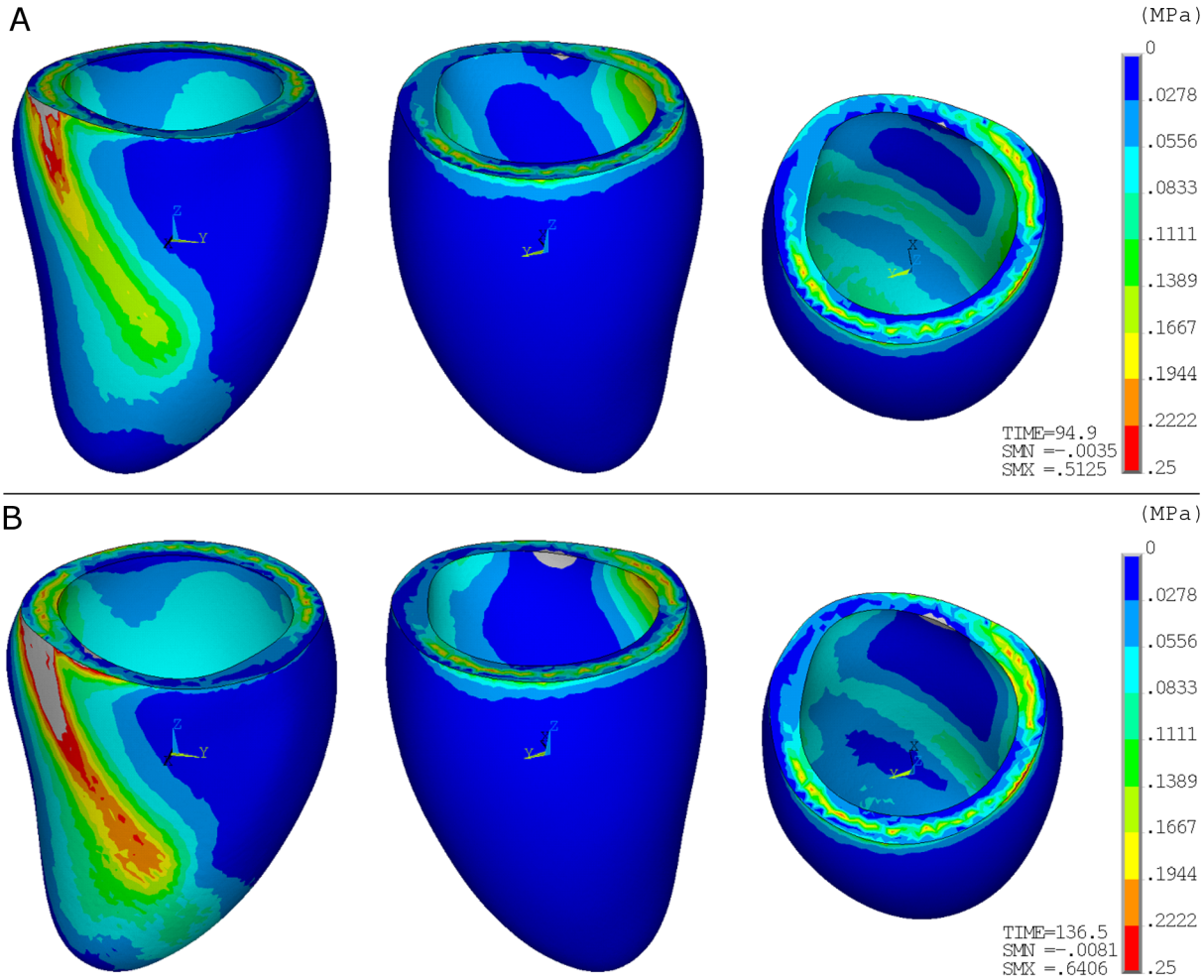

Fig. 36: Calculated distribution of the first principal stress at the beginning of ejection (A: control simulation, B: LBBB simulation). Upper bound of the contour legend was decreased to 0.25 MPa in order to remove unrealistic stress concentrations near the basal nodes with prescribed displacement boundary conditions. Lower bound of the legend was increased to 0 MPa so that both panels, A and B, use the same contour lines (for better comparison). Stresses outside the specified interval are shown in gray color. The actual calculated maximum and minimum stress values are written at the bottom of the legend along with the precise time of the beginning of ejection.

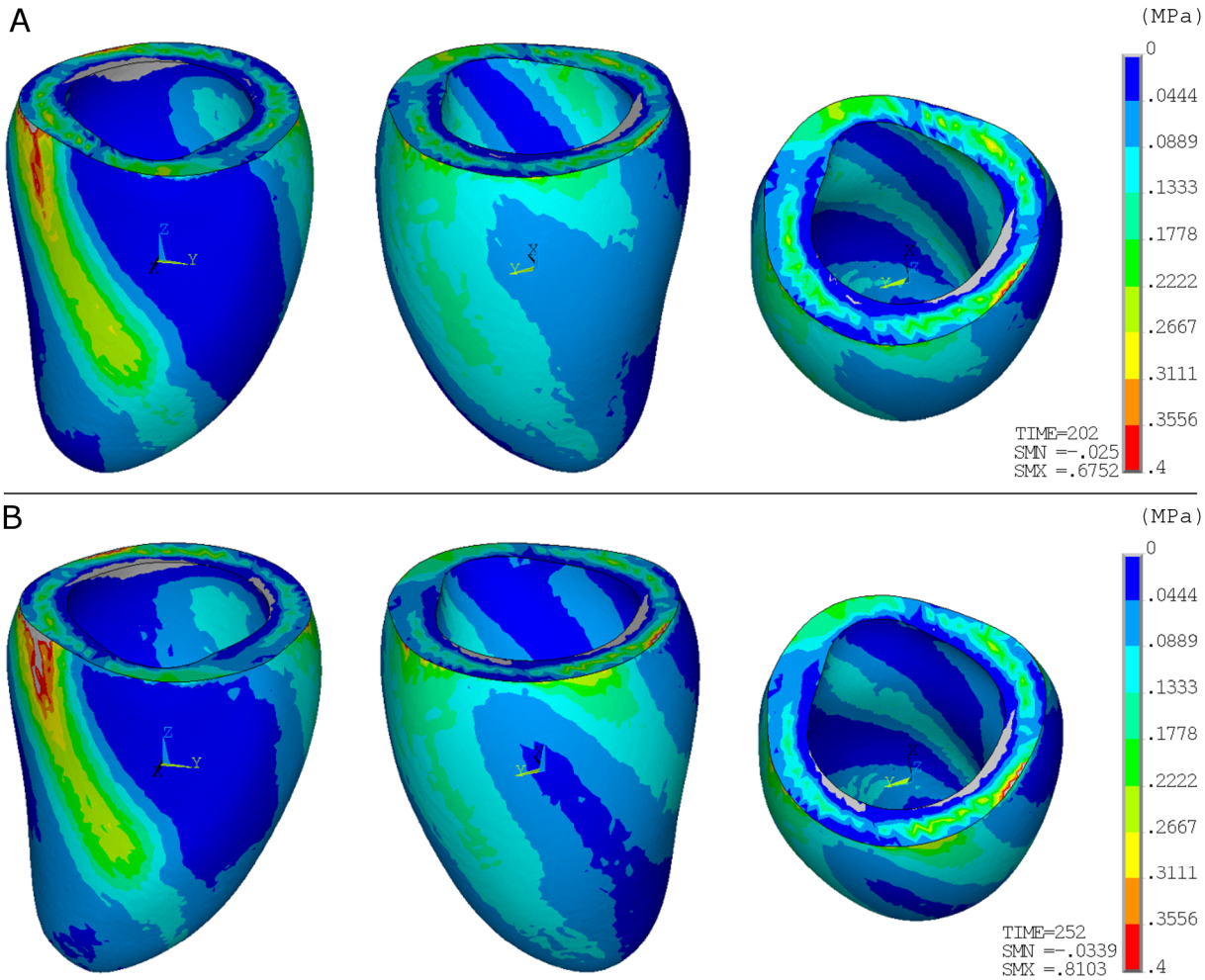

Fig. 37: Calculated distribution of the first principal stress at the moment when the LV pressure reaches its peak (A: control simulation, B: LBBB simulation). Upper bound of the contour legend was decreased to 0.4 MPa in order to remove unrealistic stress concentrations near the basal nodes with prescribed displacement boundary conditions. Lower bound of the legend was increased to 0 MPa so that both panels, A and B, use the same contour lines (for better comparison). Stresses outside the specified interval are shown in gray color. The actual calculated maximum and minimum stress values are written at the bottom of the legend along with the precise time when the peak pressure was reached.

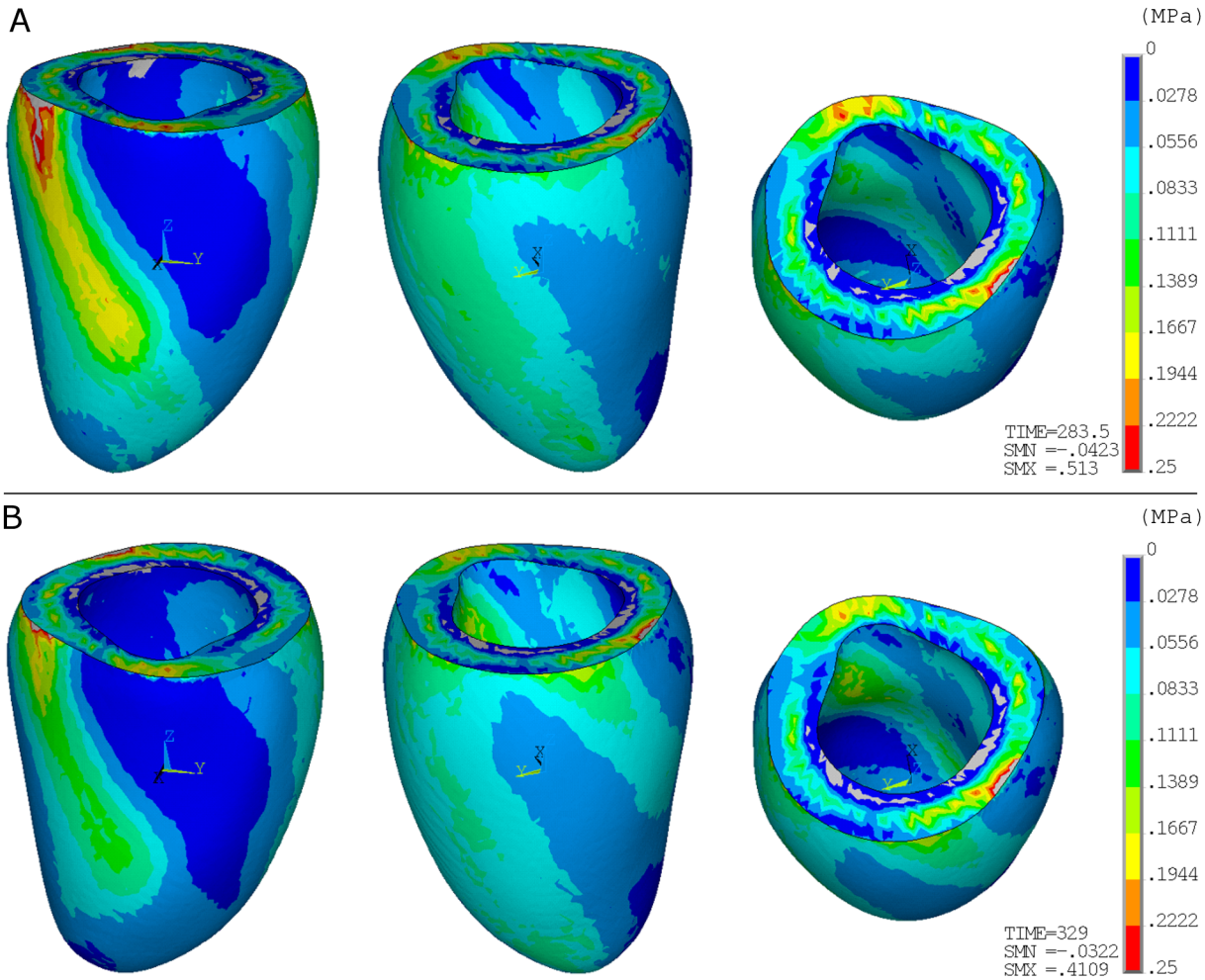

Fig. 38: Calculated distribution of the first principal stress at the end of ejection (A: control simulation, B: LBBB simulation). Upper bound of the contour legend was decreased to 0.25 MPa in order to remove unrealistic stress concentrations near the basal nodes with prescribed displacement boundary conditions. Lower bound of the legend was increased to 0 MPa so that both panels, A and B, use the same contour lines (for better comparison). Stresses outside the specified interval are shown in gray color. The actual calculated maximum and minimum stress values are written at the bottom of the legend along with the precise time of the end of ejection.

6 Conclusion

Simulations of the left ventricular contraction presented in this thesis indicate that the LBBB alone does not substantially reduce the pumping efficiency of the ventricle. When a normal electrical activation sequence was replaced by that representing the LBBB, the ejection fraction decreased by only 2.3 %, despite the fact that the total electrical activation time was prolonged by 50 %.

Mechanical consequences of the block were assessed by analyzing displacements of ventricular apex along with wall strains in the septum and in the lateral wall of the ventricle. These analyses confirmed that the model captures some basic characteristics of the LBBB-induced mechanical dyssynchrony, reported in literature. Specifically, apical displacements were increased in the presence of the block and strain analysis demonstrated delayed contraction of the lateral wall relative to the septum.

Stresses were analyzed at four characteristic instants within the cardiac cycle: the end of diastole, the beginning of ejection, the moment when the blood pressure reaches its peak (i.e. the systolic pressure), and the end of ejection. At all these stages, significantly higher stresses were observed in or around the septum than in the rest of the model. It is, however, questionable whether such high stresses truly exist in a beating heart in which the stress distribution is surely influenced by forces arising from the right ventricular contraction, which were neglected in the present study (as they were in many other studies that modeled only the left ventricle, isolated from its surroundings [40, 47, 75, 94]). However, the results presented in this work suggest that it could be beneficial to take these interactions between the left and the right ventricle into consideration in the future; at least the right ventricular blood pressure should be applied on the right septal surface and the results compared with those presented here.

In regions outside the septum, the stress pattern was markedly influenced by the prescribed fibre directions which emphasizes how important it is to describe the mechanical behavior of myocardium by anisotropic constitutive equations and to respect the arrangement of fibres in ventricular walls. Interestingly, stress magnitudes were not considerably different in control and LBBB simulations, except for the septum.

Besides the ignored influence of the right ventricle, several other shortcomings of the model were pointed out throughout this work. The strain-energy function proposed in Sec. 5.4, although seemingly suitable for modeling biaxial and simple shear responses, does not correctly order the simple shear modes according to their stiffness. This inconsistency of the constitutive model is barely perceptible in the present case, but the suitability of the model for the description of myocardial behavior is of course challenged by this fact.

Inaccuracies were also recognized on the simulated LV pressure curves. The calculated pressure rise during IVC is not entirely realistic, even though the total duration of IVC corresponds well with clinical measurements for both control and LBBB conditions. Also, the ejection phase is too short in both simulations which is most likely an inherent drawback of the two-element Windkessel model which was used to calculate the pressure boundary condition during the ejection phase.

These shortcomings identify some potential directions for future improvement.

References

[1] Seeley RR, Stephens TD, Tate P. Anatomy and Physiology. 6th ed. McGraw-Hill Higher Education; 2003.

[2] Mitchell J, Wang JJ. Expanding application of the Wiggers diagram to teach cardiovascular physiology. Advances in physiology education. 2014 06;38:170-5.

[3] Hudsmith L, Petersen S, Francis J, Robson M, Neubauer S. Normal Human Left and Right Ventricular and Left Atrial Dimensions Using Steady State Free Precession Magnetic Resonance Imaging. Journal of cardiovascular magnetic resonance : official journal of the Society for Cardiovascular Magnetic Resonance. 2005 10;7:775-82.

[4] Biering-Sørensen T, Møgelvang R, Schnohr P, Jensen J. Cardiac Time Intervals Measured by Tissue Doppler Imaging M-mode: Association With Hypertension, Left Ventricular Geometry, and Future Ischemic Cardiovascular Diseases. Journal of the American Heart Association. 2016 01;5.

[5] Duzenli MA, Özdemir K, Aygul N, Soylu A, Aygul MU, Gök H. Comparison of myocardial performance index obtained either by conventional echocardiography or tissue Doppler echocardiography in healthy subjects and patients with heart failure. Heart and Vessels. 2009;24:8-15.

[6] Anderson R, Smerup M, Sánchez-Quintana D, Loukas M, Lunkenheimer PP. The three-dimensional arrangement of the myocytes in the ventricular walls. Clinical anatomy (New York, NY). 2009 01;22:64-76.

[7] Agger P, Ilkjær C, Laustsen C, Smerup M, Frandsen J, Ringgaard S, et al. Changes in overall ventricular myocardial architecture in the setting of a porcine animal model of right ventricular dilation. Journal of Cardiovascular Magnetic Resonance. 2017 12;19.

[8] Stephenson RS, Agger P, Lunkenheimer PP, Zhao J, Smerup M, Niederer P, et al. The functional architecture of skeletal compared to cardiac musculature: Myocyte orientation, lamellar unit morphology, and the helical ventricular myocardial band. Clinical Anatomy. 2016;29(3):316-32.

[9] Lunkenheimer PP, Niederer P. Hierarchy and inhomogeneity in the systematic structure of the mammalian myocardium: towards a comprehensive view of cardiodynamics. Technology and health care. 2012;20(5):423-34.

[10] Stephenson R, Agger P, Omann C, Sánchez-Quintana D, Jarvis J, Anderson R. Resolving the True Ventricular Mural Architecture. Journal of Cardiovascular Development and Disease. 2018 06;5:34.

[11] Caldwell BJ, Trew ML, Sands GB, Hooks DA, LeGrice IJ, Smaill BH. Three Distinct Directions of Intramural Activation Reveal Nonuniform Side-to-Side Electrical Coupling of Ventricular Myocytes. Circulation: Arrhythmia and Electrophysiology. 2009;2(4):433-40.

[12] Sommer G, Schriefl AJ, Andrä M, Sacherer M, Viertler C, Wolinski H, et al. Biomechanical properties and microstructure of human ventricular myocardium. Acta Biomaterialia. 2015;24:172-92.

[13] Nielles-Vallespin S, Khalique Z, Ferreira PF, de Silva R, Scott AD, Kilner P, et al. Assessment of Myocardial Microstructural Dynamics by In Vivo Diffusion Tensor Cardiac Magnetic Resonance. Journal of the American College of Cardiology. 2017;69(6):661-76.

[14] Holzapfel GA, Ogden RW. Constitutive modelling of passive myocardium: a structurally based framework for material characterization. Philosophical Transactions of the Royal Society A: Mathematical, Physical and Engineering Sciences. 2009;367(1902):3445-75.

[15] Macfarlane PW, van Oosterom A, Pahlm O, Kligfield P, Janse M, Camm J. Comprehensive Electrocardiology. 6th ed. Springer London; 2010.

[16] Bueno-Orovio A, Cherry EM, Fenton FH. Minimal model for human ventricular action potentials in tissue. Journal of theoretical biology. 2008;253 3:544-60.

[17] Colli Franzone P, Pavarino LF, Scacchi S. Mathematical Cardiac Electrophysiology. Springer International Publishing; 2014.

[18] Fenton F, Karma A. Vortex dynamics in three-dimensional continuous myocardium with fiber rotation: Filament instability and fibrillation. Chaos: An Interdisciplinary Journal of Nonlinear Science. 1998;8(1):20-47.

[19] Näbauer M, Beuckelmann DJ, Überfuhr P, Steinbeck G. Regional Differences in Current Density and Rate-Dependent Properties of the Transient Outward Current in Subepicardial and Subendocardial Myocytes of Human Left Ventricle. Circulation. 1996;93(1):168-77.

[20] Anderson RH, Yanni J, Boyett MR, Chandler NJ, Dobrzynski H. The anatomy of the cardiac conduction system. Clinical Anatomy. 2009;22(1):99-113.

[21] Stephenson R, Atkinson A, Kottas P, Filip P, Jafarzadeh F, Bateman M, et al. High resolution 3-Dimensional imaging of the human cardiac conduction system from microanatomy to mathematical modeling. Scientific Reports. 2017 12;7.

[22] Tawara S. Das Reizleitungssystem des Säugetierherzens: eine anatomisch-histologische Studie über das Atrioventrikularbündel und die Purkinjeschen Fäden. Fischer; 1906.

[23] Scheinman M. Role of the His-Purkinje system in the genesis of cardiac arrhythmia. Heart rhythm : the official journal of the Heart Rhythm Society. 2009 04;6:1050-8.

[24] Kléber AG, Janse MJ, Fast VG. In: Normal and Abnormal Conduction in the Heart. John Wiley & Sons, Ltd; 2011. p. 455-530.

[25] Durrer D, van Dam RT, Freud GE, Janse MJ, Meijler FL, Arzbaecher RC. Total Excitation of the Isolated Human Heart. Circulation. 1970;41(6):899-912.

[26] Smiseth OA, Aalen JM. Mechanism of harm from left bundle branch block. Trends in Cardiovascular Medicine. 2019;29(6):335-42.

[27] Zannad F, Huvelle E, Dickstein K, van Veldhuisen DJ, Stellbrink C, Køber L, et al. Left bundle branch block as a risk factor for progression to heart failure. European Journal of Heart Failure. 2007;9(1):7-14.

[28] Voigt JU, Schneider TM, Korder S, Szulik M, Gürel E, Daniel WG, et al. Apical transverse motion as surrogate parameter to determine regional left ventricular function inhomogeneities: a new, integrative approach to left ventricular asynchrony assessment. European Heart Journal. 2009 03;30(8):959-68.

[29] Stankovic I, Prinz C, Ciarka A, Daraban AM, Kotrc M, Aarones M, et al. Relationship of visually assessed apical rocking and septal flash to response and long-term survival following cardiac resynchronization therapy (PREDICT-CRT). European Heart Journal - Cardiovascular Imaging. 2015 11;17(3):262-9.

[30] Guccione JM, Costa KD, McCulloch AD. Finite element stress analysis of left ventricular mechanics in the beating dog heart. Journal of Biomechanics. 1995;28(10):1167-77.

[31] Cikes M, Solomon SD. Beyond ejection fraction: an integrative approach for assessment of cardiac structure and function in heart failure. European Heart Journal. 2015 09;37(21):1642-50.

[32] Grines CL, Bashore TM, Boudoulas H, Olson S, Shafer P, Wooley CF. Functional abnormalities in isolated left bundle branch block. The effect of interventricular asynchrony. Circulation. 1989;79(4):845-53.

[33] Özdemir K, Altunkeser BB, Daniş G, Özdemir A, Uluca Y, Tokaç M, et al. Effect of the isolated left bundle branch block on systolic and diastolic functions of left ventricle. Journal of the American Society of Echocardiography. 2001;14(11):1075-9.

[34] Valenti V, Zia MI, Shubayev L, Edelstein S, Supariwala A, Uretsky S, et al. Cardiac Magnetic Resonance Evaluation of the Impact of Interventricular and Intraventricular Dyssynchrony on Cardiac Ventricular Systolic and Diastolic Function in Patients With Isolated Left Bundle Branch Block. The American Journal of Cardiology. 2012;110(11):1651-6.

[35] Akhtari S, Chuang M, Salton C, Berg S, Kissinger K, Goddu B, et al. Effect of isolated left bundle-branch block on biventricular volumes and ejection fraction: a cardiovascular magnetic resonance assessment. J Cardiovasc Magn Reson. 2018;20(66).

[36] Aalen J, Storsten P, Remme EW, Sirnes PA, Gjesdal O, Larsen CK, et al. Afterload Hypersensitivity in Patients With Left Bundle Branch Block. JACC: Cardiovascular Imaging. 2019;12(6):967-77.

[37] Lee A, Mendonça Costa C, Strocchi M, Rinaldi C, Niederer S. Computational Modeling for Cardiac Resynchronization Therapy. Journal of Cardiovascular Translational Research. 2018 04;11.

[38] Dou J, Xia L, Zhang Y, Shou G, Wei Q, Liu F, et al. Mechanical analysis of congestive heart failure caused by bundle branch block based on an electromechanical canine heart model. Physics in medicine and biology. 2009 02;54:353-71.

[39] Dokos S, Smaill B, Young A, Legrice I. Shear properties of passive ventricular myocardium. American journal of physiology Heart and circulatory physiology. 2003 01;283:H2650-9.

[40] Quarteroni A, Lassila T, Rossi S, Ruiz-Baier R. Integrated Heart—Coupling multiscale and multiphysics models for the simulation of the cardiac function. Computer Methods in Applied Mechanics and Engineering. 2017;314:345-407.

[41] Vaverka J, Burša J, Šumbera J, Pásek M. Effect of Transmural Differences in Excitation-Contraction Delay and Contraction Velocity on Left Ventricle Isovolumic Contraction: A Simulation Study. BioMed Research International. 2018;2018.

[42] Vaverka J, Moudr J, Lokaj P, Burša J, Pásek M. Impact of Decreased Transmural Conduction Velocity on the Function of the Human Left Ventricle: A Simulation Study. BioMed Research International. 2020;2020.

[43] Truesdell C. A First Course in Rational Continuum Mechanics: General Concepts. 2nd ed. Academic Press; 1991.

[44] Bai W, Shi W, de Marvao A, Dawes TJW, O'Regan DP, Cook SA, et al. A bi-ventricular cardiac atlas built from 1000+ high resolution MR images of healthy subjects and an analysis of shape and motion. Medical Image Analysis. 2015;26(1):133-45.

[45] Ginat DT, Fong MW, Tuttle DJ, Hobbs SK, Vyas RC. Cardiac Imaging: Part 1, MR Pulse Sequences, Imaging Planes, and Basic Anatomy. American Journal of Roentgenology. 2011;197(4):808-15.

[46] Ciarlet PG. The Finite Element Method for Elliptic Problems. Classics in Applied Mathematics. Society for Industrial and Applied Mathematics; 2002.

[47] Gerbi A, Dedè L, Quarteroni A. A monolithic algorithm for the simulation of cardiac electromechanics in the human left ventricle. Mathematics in Engineering. 2019;1(1):1-37.

[48] Noll W. Finite-dimensional spaces. Algebra, geometry and analysis. Volume I. 1st ed. Martinus Nijhoff Publishers; 1987. Available also on prof. Noll's website https://www.math.cmu.edu/∼wn0g/noll/.

[49] Clayton RH, Bernus O, Cherry EM, Dierckx H, Fenton FH, Mirabella L, et al. Models of cardiac tissue electrophysiology: Progress, challenges and open questions. Progress in Biophysics and Molecular Biology. 2011;104(1):22-48.

[50] Pathmanathan P, Mirams GR, Southern J, Whiteley JP. The significant effect of the choice of ionic current integration method in cardiac electro-physiological simulations. International Journal for Numerical Methods in Biomedical Engineering. 2011;27(11):1751-70.

[51] Pathmanathan P, Bernabeu MO, Bordas R, Cooper J, Garny A, Pitt-Francis JM, et al. A numerical guide to the solution of the bidomain equations of cardiac electrophysiology. Progress in Biophysics and Molecular Biology. 2010;102(2):136-55.

[52] Quarteroni A, Valli A. Numerical Approximation of Partial Differential Equations. Springer-Verlag; 1994.

[53] Zienkiewicz OC, Taylor RL, Zhu JZ. The Finite Element Method: Its Basis and Fundamentals. Sixth edition ed. Butterworth-Heinemann; 2005.

[54] Bonet J, Wood RD. Nonlinear Continuum Mechanics for Finite Element Analysis. Cambridge University Press; 2008.

[55] Ansys 2021 R1: Theory Reference. ANSYS Inc., Canonsburg, Pennsylvania;. http://www.ansys.com.

[56] Bowen RM, Wang C. Introduction to Vectors and Tensors. Dover books on mathematics. Dover Publications; 2008.

[57] Ten Tusscher KHWJ, Panfilov AV. Modelling of the ventricular conduction system. Progress in Biophysics and Molecular Biology. 2008;96(1):152-70.

[58] Potse M, Krause D, Kroon W, Murzilli R, Muzzarelli S, Regoli F, et al. Patient-specific modelling of cardiac electrophysiology in heart-failure patients. Europace. 2014 11;16:iv56-61.

[59] Mendez C, Mueller WJ, Urguiaga X. Propagation of Impulses across the Purkinje Fiber-Muscle Junctions in the Dog Heart. Circulation Research. 1970;26(2):135-50.

[60] Mazur A, Kusniec J, Strasberg B. Bundle Branch Reentrant Ventricular Tachycardia. Indian pacing and electrophysiology journal. 2005 02;5:86-95.

[61] Strauss DG, Selvester RH, Wagner GS. Defining Left Bundle Branch Block in the Era of Cardiac Resynchronization Therapy. The American Journal of Cardiology. 2011;107(6):927-34.

[62] Strik M, Rademakers LM, van Deursen CJM, van Hunnik A, Kuiper M, Klersy C, et al. Endocardial Left Ventricular Pacing Improves Cardiac Resynchronization Therapy in Chronic Asynchronous Infarction and Heart Failure Models. Circulation: Arrhythmia and Electrophysiology. 2012;5(1):191-200.

[63] Hyde ER, Behar JM, Claridge S, Jackson T, Lee AWC, Remme EW, et al. Beneficial Effect on Cardiac Resynchronization From Left Ventricular Endocardial Pacing Is Mediated by Early Access to High Conduction Velocity Tissue. Circulation: Arrhythmia and Electrophysiology. 2015;8(5):1164-72.

[64] Grant RP, Dodge HT. Mechanisms of QRS complex prolongation in man: Left ventricular conduction disturbances. The American Journal of Medicine. 1956;20(6):834-52.

[65] Okada J, Washio T, Nakagawa M, Watanabe M, Kadooka Y, Kariya T, et al. Absence of Rapid Propagation through the Purkinje Network as a Potential Cause of Line Block in the Human Heart with Left Bundle Branch Block. Frontiers in Physiology. 2018;9.

[66] Truesdell C, Noll W. The Non-linear Field Theories of Mechanics. 2nd ed. Springer-Verlag; 1992. (A corrected reprint of the 1st edition from 1965.).

[67] Noll W. Five Contributions to Natural Philosophy. 2004. Published on prof. Noll's website https://www.math.cmu.edu/∼wn0g/noll/.

[68] Yin FCP, Strumpf RK, Chew PH, Zeger SL. Quantification of the mechanical properties of noncontracting canine myocardium under simultaneous biaxial loading. Journal of Biomechanics. 1987;20(6):577-89.

[69] Humphrey JD, Yin FCP. On Constitutive Relations and Finite Deformations of Passive Cardiac Tissue: I. A Pseudostrain-Energy Function. Journal of Biomechanical Engineering. 1987 11;109(4):298-304.

[70] Costa KD, Holmes JW, McCulloch AD. Modelling Cardiac Mechanical Properties in Three Dimensions. Philosophical Transactions: Mathematical, Physical and Engineering Sciences. 2001;359(1783):1233-50.

[71] Schröder J, Neff P. Invariant formulation of hyperelastic transverse isotropy based on polyconvex free energy functions. International Journal of Solids and Structures. 2003;40(2):401-45.

[72] Balzani D, Neff P, Schröder J, Holzapfel GA. A polyconvex framework for soft biological tissues. Adjustment to experimental data. International Journal of Solids and Structures. 2006;43(20):6052-70.

[73] Holzapfel G, Gasser T, Ogden R. A New Constitutive Framework for Arterial Wall Mechanics and a Comparative Study of Material Models. Journal of Elasticity. 2012 04;61:1-48.

[74] Göktepe S, Acharya SNS, Wong J, Kuhl E. Computational modeling of passive myocardium. International Journal for Numerical Methods in Biomedical Engineering. 2011;27(1):1-12.

[75] Eriksson T, Prassl A, Plank G, Holzapfel G. Influence of myocardial fiber/sheet orientations on left ventricular mechanical contraction. Mathematics and Mechanics of Solids. 2013;18(6):592-606.

[76] Palit A, Bhudia S, Arvanitis T, Turley G, Williams M. In vivo estimation of passive biomechanical properties of human myocardium. Medical & Biological Engineering & Computing. 2018 02;56:1-17.

[77] Nolan D, Gower A, Destrade M, Ogden RW, Mcgarry P. A robust anisotropic hyperelastic formulation for the modelling of soft tissue. Journal of the Mechanical Behavior of Biomedical Materials. 2014 11;39:48–60.

[78] Vergori L, Destrade M, Mcgarry P, Ogden R. On anisotropic elasticity and questions concerning its Finite Element implementation. Computational Mechanics. 2013 11;52:1185-97.

[79] Mcevoy E, Holzapfel G, McGarry P. Compressibility and Anisotropy of the Ventricular Myocardium: Experimental Analysis and Microstructural Modeling. Journal of Biomechanical Engineering. 2018 05;140:081004.

[80] Steigmann D. Frame-invariant polyconvex strain-energy functions for some anisotropic solids. Mathematics and Mechanics of Solids. 2003 10;8:497-506.

[81] Bellini C, Federico S. Green-Naghdi rate of the Kirchhoff stress and deformation rate: the elasticity tensor. Zeitschrift für angewandte Mathematik und Physik. 2015;66:1143-63.

[82] Holzapfel GA. Nonlinear Solid Mechanics: A Continuum Approach for Engineering. Wiley; 2000.

[83] Ansys 2021 R1: Programmer's Reference. ANSYS Inc., Canonsburg, Pennsylvania;. http://www.ansys.com.

[84] Suchocki C. A Finite Element Implementation of Knowles Stored-Energy Function: Theory, Coding and Applications. Archive of Mechanical Engineering. 2011 01;LVIII.

[85] Johnson BE, Hoger A. The use of a virtual configuration in formulating constitutive equations for residually stressed elastic materials. Journal of Elasticity. 1995;41:177-215.

[86] Hoger A. Virtual Configurations and Constitutive Equations for Residually Stressed Bodies with Material Symmetry. Journal of Elasticity. 1997;48:125-44.

[87] Maas S, Erdemir A, Halloran J, Weiss J. A General Framework for Application of Prestrain to Computational Models of Biological Materials. Journal of the Mechanical Behavior of Biomedical Materials. 2016 04;61.

[88] Giantesio G, Musesti A, Riccobelli D. A Comparison Between Active Strain and Active Stress in Transversely Isotropic Hyperelastic Materials. Journal of Elasticity. 2019 10.

[89] Pezzuto S, Ambrosi D, Quarteroni A. An orthotropic active–strain model for the myocardium mechanics and its numerical approximation. European Journal of Mechanics - A/Solids. 2014 11;48.

[90] Boyett M, Frampton J, Kirby M. The length, width and volume of isolated rat and ferret ventricular myocytes during twitch contractions and changes in osmotic strength. Experimental Physiology. 1991;76(2):259-70.

[91] Holubarsch C, Lüdemann J, Wiessner S, Ruf T, Schulte-Baukloh H, Schmidt-Schweda S, et al. Shortening versus isometric contractions in isolated human failing and non-failing left ventricular myocardium: dependency of external work and force on muscle length, heart rate and inotropic stimulation. Cardiovascular Research. 1998 01;37(1):46-57.

[92] Cordeiro JM, Greene L, Heilmann C, Antzelevitch D, Antzelevitch C. Transmural heterogeneity of calcium activity and mechanical function in the canine left ventricle. American Journal of Physiology-Heart and Circulatory Physiology. 2004;286(4):H1471-9.

[93] Stergiopulos N, Meister JJ, Westerhof N. Evaluation of methods for estimation of total arterial compliance. The American journal of physiology. 1995;268 4 Pt 2:H1540-8.

[94] Eriksson T, Prassl A, Plank G, Holzapfel G. Modeling the dispersion in electromechanically coupled myocardium. International journal for numerical methods in biomedical engineering. 2013 01;29:1267-84.

[95] Baim DS, Grossman W. Grossman's Cardiac Catheterization, Angiography, and Intervention. LWW medical book collection. Lippincott Williams & Wilkins; 2006.

[96] Byrne MJ, Helm RH, Daya S, Osman NF, Halperin HR, Berger RD, et al. Diminished Left Ventricular Dyssynchrony and Impact of Resynchronization in Failing Hearts With Right Versus Left Bundle Branch Block. Journal of the American College of Cardiology. 2007;50(15):1484-90.

List of abbreviations

FE	finite-element
IVC	isovolumic contraction
LBBB	left bundle branch block
LV	left ventricle
SD	standard deviation